Predictive Milling of Active Pharmaceutical Ingredients and Excipients

by

Selasi Cudjoe Dogbe

Submitted in accordance with the requirements for the degree of

Doctor of Philosophy

The University of Leeds

The School of Chemical and Process Engineering

December 2016

The candidate confirms that the work submitted is his own and that appropriate credit has been given where reference has been made to the work of others.

This copy has been supplied on the understanding that it is copyright material and that no quotation from the thesis may be published without proper acknowledgement.

Acknowledgements

The best spectacles in the world tend to happen every four years. The Olympics. The World Cup. A leap year. But here marks the greatest spectacle of them all: Selasi completes his PhD. It has been a long and arduous journey, but one that I can honestly say I've enjoyed taking and am very proud (and relieved) to finish. However, I would not have been able to complete this feat alone. Everyone needs the support of others at some point to achieve the remarkable. Even Jesus had disciples. So I would like to take this moment to recognise those that have played important roles in my life over the past four years.

Melissa Chee!!! I can't thank you enough for all your help in the experimental work of this research. You are one of the brightest and most interesting people I've been

honoured enough to meet, and I'm sure you are going to go on to achieve amazing things. I look forward to telling people "that woman was my student once"!

It's very rare that you come across an engineer who is both intelligent and down to earth, capable of holding engaging conversation beyond topics like the mesoscopic behaviour of particulate systems. Somehow I've been blessed with a group full of them! I must acknowledge Dr Massih Pasha first, for giving me my first taste of research work in the Ghadiri Research Group and being part of the motivation behind me deciding to take up the PhD. The two people I started this journey with: Dr Tina Bonakdar and Siwarote "Pom" Siriluck. It has been a lot of fun having you two sitting either side of me. We've experienced many highs and lows together, and have always manage to continue laughing throughout. If you guys weren't there, who knows if I would have made it far enough to even write these acknowledgements. Dr Vincenzino Vivacqua, you've always been a sturdy tank for me to pour all my anger and frustrations from this PhD into, and for that I am in debt to you. Office 2.16 (as well as wine and cheese, juice and nuts, and all its variations) would not be complete without the presence of Dr Mehrdad Pasha, Dr Umair Zafar, Fabio Fulchini and Wei Pin Goh; I am blessed to be able to call you guys not only colleagues, but friends. There have been several others who have come and gone in the group while I've been here, and though their stay may not have been long, they have certainly had an impact on my life ("short but intense" some would say), and for that I will never forget them. Thank you Francesca "Franché" Orsola Alfano, Caterina Rizzo, Dr Qinqin Chen, Wenguang "Mr Nan" Nan, and Dr Nick Ku. I have a lot of time for you all.

The strength and confidence of my family has been a major catalyst throughout these past four years. Thank you Dad for never showing any kind of doubt in or question of my ability, and always pushing me to achieve more than I think possible. Thank you Mum for your never-ending love and support throughout the duration of this PhD course, especially for the monthly supply of jollof rice and chicken. You fuelled the work in this thesis! My sisters: Dela and Senna. Thank you for holding it down and still riding for man even after I abandoned you to come back to Leeds and do this PhD. You two helped keep my ears to the streets with the latest music and dances, and always gave me live updates of everything happening in the house to the point it was like I never left! Safiya Kinshasa, thank you for your constant encouragement, for being there for me whenever, and most importantly, for your "annoyingness"; you've helped keep me sane!

For my family

Abstract

Spiral jet milling is a size reduction process used in various industries, ranging from paints to food and pharmaceuticals. It has great benefit in the pharmaceutical industry due to its ability to reduce particulate solids to micron sizes and narrow size distributions. Despite its heavy usage, the underlying size reduction mechanism of the mill is not well understood. However it is generally known that the milling behaviour is dependent on the grinding conditions of the mill, as well as the materials physical and mechanical properties. The system is also very energy inefficient.

In this work the milling behaviour of active pharmaceutical ingredients and excipients in the spiral jet mill has been analysed based on their mechanical properties, as established from the Ghadiri and Zhang semi-brittle breakage model. Using the Single Particle Impact Test Rig, the breakability index ($\alpha H/K_C^2$) of three pharmaceutical materials (paracetamol, aspirin, and α-lactose monohydrate) is determined. It is shown that the order of breakability is paracetamol > aspirin > α-lactose monohydrate.

For milling studies the Hosokawa Alpine Aeroplex Spiral Jet Mill 50AS is used. The change in specific surface area (ΔSSA) due to milling is quantified by size analysis and related to the breakability indices. The order of ΔSSA is α-lactose monohydrate > paracetamol > aspirin at high grinding pressure conditions. The loading of particles in the grinding chamber of the mill is found to be an important characteristic for the classification of milled materials in addition to the effects of centrifugal and drag forces.

Numerical simulations have been carried out and used to analyse the behaviour of the spiral jet mill. Using Computational Fluid Dynamics, the mechanics of internal particle classification by size of the 50AS has been analysed. Particles of 2 μm and less are shown to be classified. The Discrete Element Method is coupled with Computational Fluid Dynamics to investigate the effect of grinding conditions and particle properties on the particle motion and fluid-particle energy transfer, including gas pressure, the number of particles and the particle size distribution. A very small amount of energy is transferred to the particles from the fluid, highlighting the energy inefficiency of the system. Interparticle interactions are found to have a greater amount of dissipated energy compared to particle-wall interactions, which suggests interparticle collisions are the primary source of particle breakage. The majority of the stress exerted on the particles is close to the wall of the mill, with the normal stress being greater than the shear stress. A very low proportion of particles are found to be in contact at a given time, indicating particle breakage occurs from instantaneous collisions rather than particles shearing against each other.

Finally the potential for scale-up of the spiral jet mill is investigated based on the fluid power input to the system. There is a good comparison of the ΔSSA of α-lactose monohydrate milled in four different mills at similar fluid power input conditions. Two of the mills are the 50AS and the Hosokawa Alpine Piconizer (33 AS), and the other two are of different design but with internal diameters of 2 inches and 4 inches, i.e. roughly similar size to the Hosokawa mills. The latter two mills had a greater fluid power as the grinding nozzle diameters are larger than the Hosokawa mills.

Table of Contents

List of Figures

List of Tables

UNIVERSITY OF LEEDS

Nomenclature

a	Constant	-
b	Constant	-
c	Constant	-
c	Dashpot coefficient	-
c_t	Tangential dashpot coefficient	-
C_l	Drag coefficient as the Reynolds number tends towards infinity	-
$C_{l\varepsilon}$	Constant	-
$C_{2\varepsilon}$	Constant	-
$C_{3\varepsilon}$	Constant	-
C_D	Drag coefficient	-
C_E	Empirical constant (=9.793)	-
C_M	Mass transfer coefficient	-
C_p	Specific heat at constant pressure	J/kg·K
C_v	Specific heat at constant volume	J/kg·K
C_μ	Constant	-
D	Particle size	m
d_c	Diameter of the milling chamber	m

d_{cut}	Particle cut size diameter	m
d_o	Diameter of outlet	m
d_p	Particle diameter	m
$d_{Reynolds}$	Length scale of particle at the grinding chamber exit	m
e	Coefficient of restitution	-
E^*	Equivalent Young's modulus	Pa
E_{fract}	Fracture energy	J/m^3
E_{kin}	Kinetic energy of particles	J
E_{sp}	Specific energy consumption	J/g
$\boldsymbol{F}_s$	Source term for momentum transfer	$kg/m^2{\cdot}s^2$
$\boldsymbol{F}_b$	Body force	N
$\boldsymbol{F}_c$	Contact force	N
f_{ce}	Pull-off force	N
f_{cp}	Pull-off force after plastic deformation	N
$\boldsymbol{F}_D$	Drag force	N
$\boldsymbol{F}_g$	Gravitational force	N
$\boldsymbol{F}_{Mag}$	Magnus lift force	N
f_{Mat}	Resistance of particle material against volume specific external stressing energy	g/J·m

F_n	Normal contact force	N
$F_n{}^d$	Normal damping force	N
F_{nc}	Non-contact force	N
F_{saff}	Saffman lift force	N
F_t	Tangential contact force	N
$F_t{}^d$	Tangential damping force	N
G	Particle shear modulus	Pa
g	Gravity force vector	m/s^2
G^*	Equivalent shear modulus	Pa
G_b	Generation of turbulence kinetic energy due to buoyancy	kg/m·s^3
G_k	Generation of turbulence kinetic energy due to the mean velocity gradients	kg/m·s^3
H	Hardness	Pa
h_1	Height of the central outlet in the grinding chamber	m
h_2	Height of the grinding chamber	m
I	Moment of inertia	kg·m^2
k	Turbulent kinetic energy	m^2/s^2
K	Dimensionless number	-
K_c	Fracture toughness	MPa·m$^{1/2}$

k_{cp}	Plastic-cohesive stiffness	N/m
k_e	Elastic stiffness	N/m
k_n	Normal stiffness	N/m
k_p	Plastic stiffness	N/m
k_t	Tangential contact stiffness	N/m
ℓ	Flaw length	m
m	Mass	kg
m^*	Equivalent mass	kg
$\boldsymbol{M}$	Contact torque between particles and walls	N·m
M_1	Mach number at the nozzle exit	-
M_{de}	Mass of debris particles	kg
M_f	Mass of feed particles	kg
$\dot{m}_F$	Gas mass flow rate	kg/s
M_m	Mass of mother particles	kg
$\dot{m}_p$	Solid feed rate	kg/s
M_w	Gas molecular weight	g/mol
N	Total number of sample points	-
N_B	Total number of particles in bin	-

n_c	Number of sample points of a particle within the mesh cell	-
P	Gas pressure	Pa
P^*	Critical pressure	Pa
P_0	Pressure of gas entering the nozzle	Pa
P_y	Yield pressure	Pa
Q	Volumetric air flow rate	m^3/s
r	Radial position	m
R	Universal gas constant	$J/K \cdot mol$
R^*	Extent of breakage	%
R_p	Particle radius	m
R_p^*	Equivalent radius	m
S	Breakage probability	-
S_k	User-defined source term	-
S_M	Momentum sink	$kg/m^2 \cdot s^2$
$\bar{S}_m$	Source term arising from the exchange of mass	$kg/m^3 \cdot s$
S_ε	User-defined source term	-
t	Time	s
T	Gas temperature	K

T^*	Critical temperature	K
T_0	Temperature of gas entering the nozzle	K
T_{fp}	Fluid-induced torque	N/m
T_R	Rayleigh time-step	s
u_i	Fluid velocity	m/s
$\bar{u}_i$	Time-average velocity component	m/s
u_i'	Fluctuating velocity component	m/s
U^*	Dimensionless velocity	-
v	Impact velocity	m/s
V_B	Bin volume	m^3
v_C	Characteristic velocity	m/s
V_F	Gas volume	m^3
V_m	CFD mesh cell volume	m^3
$\boldsymbol{v}_n^{rel}$	Normal component of the relative velocity	m/s
$\boldsymbol{v}_t^{rel}$	Tangential component of the relative velocity	m/s
$\boldsymbol{v}_p$	Particle translational velocity	m/s
V_p	Particle volume	m^3
$\boldsymbol{v}_r$	Radial gas velocity	m/s

UNIVERSITY OF LEEDS

v_{sonic}	Gas sonic velocity	m/s
v_t	Tangential velocity	m/s
$W_{m,kin}$	Mass specific impact kinetic energy	J/g
$W_{m,min}$	Specific threshold energy needed to cause fracture	J/g
Y_M	Contribution of the fluctuating dilation in compressible turbulence to the overall dissipation rate	
y^*	Dimensionless distance from the wall	-
Z	Compressibility factor	-
μ	Viscosity	kg/m·s
μ_f	Static friction coefficient	-
μ_r	Rolling friction coefficient	-
μ_{t0}	Value of turbulent viscosity calculated without swirl modification	kg/m·s
α	Proportionality constant	-
$\dot{\alpha}$	Overlap velocity	m/s
α_μ	Deformation at which sliding occurs	m
α_k	Inverse effective Prandtl number for k	-
α_n	Normal overlap	m

UNIVERSITY OF LEEDS

α_s	Swirl constant	-
α_t	Tangential overlap	m
α_ε	Inverse effective Prandtl number for ε	-
β	Load mass throughput in relation to gas mass throughput	-
γ	Ratio of specific heat at constant pressure to specific heat at constant volume (C_p/C_v)	-
ε	Turbulent dissipation rate	m^2/s^3
ζ	Time averaged mass fraction of collision fragments below the cut size	-
κ	von Kármán constant (=0.4187)	-
η	Attrition propensity parameter	-
ρ_F	Fluid density	kg/m^3
ρ_p	Particle density	kg/m^3
σ_H	Hydrostatic stress	Pa
σ_{ij}	ij-component of stress tensor	Pa
σ_k	Turbulent Prandtl number for k	-
σ_ε	Turbulent Prandtl number for ε	-
τ_D	Deviatoric stress	Pa
υ	Poisson's ratio	-

ϕ	Fluid volume fraction	-
Ω	Characteristic swirl number	-
ω	Specific turbulent dissipation rate	s^{-1}
ω_f	Fluid vorticity	s^{-1}
ω_p	Particle angular velocity	rad/s
Γ	Interface energy	J/m^2

Chapter 1 Introduction

Milling is used in a wide range of industries, spanning from pharmaceuticals to paints and coatings. There are various types of mills, each different type suited towards a specific feed and/or product size. They include crushers, grinding mills, roller mills, impact mills, jet mills, and cutting mills (Bernotat and Schönert, 2006). Crushers are generally used for coarse reduction while mills are for intermediate to fine grinding (Ortega-Rivas, 2012). Along with the feed and product particle size, the method of particle breakage also differs between the types of mill. Compressive, impact or shearing forces can be applied to reduce the size of particles. Crushers use compressive force to reduce particle size, while mills generally use impact or shearing force.

Spiral jet mills are a popular choice of equipment for size reduction, particularly in industries such as pharmaceuticals, paint and fine chemicals. They are capable of producing very fine particle sizes with narrow size distributions, which make them suitable for these industries with strict requirements on particle sizes. The mill contains no moving parts; it utilises gas as a propellant for the particles. Therefore there is no contamination of the material. There is also a low equipment wear rate. The jet mill does not produce high temperature changes during the milling process, and so is suitable for use with heat-sensitive materials. There is high turbulence in the mill during its operation, which enables high heat and mass transfer. The main disadvantage of the spiral jet mill is its inefficient energy utilisation. The mill requires a large input of energy, but only 2% of the supplied energy is used in particle breakage (Mebtoul et al., 1996). Energy is lost through

the deformation of particles and friction between particles and the containing walls (Ortega-Rivas, 2012).

Milling is used in the pharmaceutical industry for the size reduction of active pharmaceutical ingredients (API), often in crystalline form, to micron size and preferably to a narrow size distribution. In most cases the particles are needed to be in the micron size range for ease of dissolution and content uniformity, as for example, in tableting to be able to compact the correct amount of active pharmaceutical ingredient and excipients into the small-sized tablet. They are also needed in the micron size range for use in dry powder inhalers, where the powder must be small enough to enter the lungs where its effects are needed. The relative amounts of API and excipients, their sizes and their size distributions are important as they affect the bioavailability of the drug. The degree of bioavailability is related to the material properties. For example, a water-soluble micron-sized particle will dissolve in the human body at a much faster rate than a larger sized and less soluble particle. Properties such as solubility and dispersion are manipulated in order to produce drugs which target a specific part of the body in a specific amount of time. It is often the case that the quantity of material to be milled is too low to allow for the trial and error of different milling conditions until the optimum for the desired particle size and distribution is found. It would therefore be of great benefit if the milling behaviour could be predicted from analysis of the properties of a small quantity of material.

1.1 Thesis Outline and Structure

The overall aim of this work is to gain a better understanding of the behaviour of active pharmaceutical ingredients and excipients in the spiral jet mill, and look at the potential to predict the milling behaviour based on the single particle mechanical properties of the materials. This involves the use of both experimental and simulation work.

Chapter 2 gives an outline of the fundamental science behind the main concepts of the work in this thesis. The different material breakage mechanisms and modes of particle failure will be described. A brief outline will be given of laser diffraction, the main method of particle size analysis used in this work. The computational methods of Discrete Element Modelling and Computational Fluid Dynamics will be discussed, including the main contact and turbulence models involved in both.

Chapter 3 gives details of the pharmaceutical materials used in this research: aspirin, paracetamol, and α-lactose monohydrate.

Chapter 4 focusses on the single particle impact testing of the pharmaceutical materials, used in this research to characterise the material mechanical properties. A review of single impact testing is given, followed by details of the single particle breakage model and Single Particle Impact Rig utilised in the work. The results of impact testing are reported, and from these the mechanical properties of the material are inferred.

Chapter 5 contains the work on the spiral jet milling of the active pharmaceutical ingredients and excipients used. Previous research on the spiral jet mill is discussed, and then the spiral jet mill as well as the milling conditions used in this

work are described. The results include the analysis of steady-state milling in the jet mill, and the size reduction behaviour of the three pharmaceutical materials. The change in specific surface area of the materials as a function of the input fluid power will be shown and compared to the mechanical properties of the material.

Chapter 6 consists of the simulation work of the spiral jet mill. Past simulation work on the spiral jet mill is reviewed, which is then followed by details of the simulation conditions used. The classification efficiency of the mill is analysed, followed by the fluid-particle energy transfer in the system. The effects of the number of particles and gas pressure on the particle velocities and stress in the system is investigated.

Chapter 7 looks at the scale-up of the spiral jet mill, exploring the use of fluid power as the scale-up criterion. Four different sized mills are used to assess scale-up with α-lactose monohydrate, comparing the change in specific surface area as a function of fluid power input in the different mills.

Chapter 8 brings the thesis to a close, giving the conclusions of the work carried out, as well as suggestions for future investigations to expand the research.

Chapter 2 Fundamental Theory of Particle Breakage, Laser Diffraction Size Analysis, DEM and CFD

In this chapter, the fundamental science behind the main concepts involved in this research are detailed. This includes material failure modes and breakage mechanisms, particle size analysis by laser diffraction, and the computational techniques of the Discrete Element Method and Computational Fluid Dynamics.

2.1 Material Breakage Behaviour

When a particle is impacted onto a surface or another particle, it experiences stress. This stress initially causes elastic deformation of the particle, which is the temporary displacement of atoms or molecules from their standard positions. When the stress is removed, the atoms go back to their previous location. The elasticity of a linear elastic material is governed by the material Young's modulus. This is the ratio of stress applied to a material to the strain which the applied stress causes. Young's modulus is influenced by the atomic and molecular bonding of a material, and so its value can vary in a material depending on the arrangement of atomic particles in each direction.

If the applied stress surpasses the material yield stress, permanent plastic deformation occurs. This is due to slip, which is when atomic or ionic planes slip over each other at the point of maximum shear stress. Slip is primarily caused by the presence of defects in the crystal structure of the material, known as dislocations. Slip leads to dislocation pile-up, which is the displacement of atoms

or molecules from their original position to a new equilibrium position. The
material resistance to plastic deformation is defined as its hardness.

If the stress exerted on a particle is large enough, it will initiate a crack in the
material, or cause the propagation of a pre-existing crack. When dislocation
movement and slip occurs, the dislocation density in the material increases until
it reaches a critical value known as the saturation density. Beyond this point, the
movement of dislocations can no longer occur, and increasing the stress now leads
to crack initiation. Fracture toughness (also known as the critical stress intensity
factor) represents the resistance of a material to crack propagation.

Material failure is classed into three types: brittle, semi-brittle, and ductile. Brittle
failure is defined as material failure which is not preceded by any significant plastic
deformation. This is due to low dislocation mobility and a limited number of slip
planes in the material. Cracks are initiated from pre-existing flaws within the
material; the application of stress to the material creates tensile stress at the flaws.
The impact of brittle material typically creates what is known as ring and cone
cracks (Lawn, 1993). These are formed from surface flaws subjected to radial
tensile stresses around and just outside of the area of contact during impact, as
illustrated in Figure 2.1.
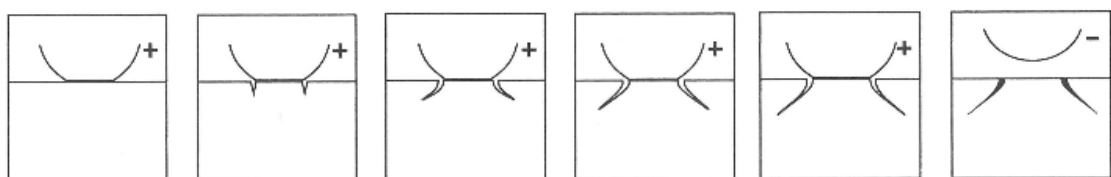
Figure 2.1: Formation of ring and cone cracks during loading and unloading (Lawn, 1993)

Semi-brittle failure occurs when cracks form after a limited extent of plastic deformation. Three types of cracks are formed in semi-brittle materials: median, radial and lateral cracks. Figure 2.2 displays the formation of radial and lateral cracks. Radial and median cracks are formed during the loading of a material. Radial cracks are formed by tensile stresses around sub-surface flaws near the elastic-plastic boundary and can propagate through the whole volume of the material, while median cracks are formed under the plastic zone (Lawn and Evans, 1977; Lawn et al., 1980). Therefore radial and median cracks are responsible for fragmentation. Lateral cracks form during unloading. They form at the plastic zone, which will typically be near the surface of the material, and are therefore responsible for surface wear (Lawn et al., 1980).
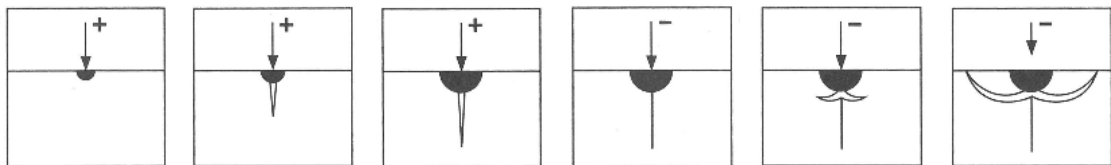
Figure 2.2: Formation of radial and lateral cracks during loading and unloading (Lawn, 1993)

Ductile failure occurs after considerable plastic deformation at the point of maximum shear stress. The main mechanisms of failure involved are ploughing and cutting, as shown in Figure 2.3 (Hutchings, 1993). Ploughing is the result of a rounded particle impacting the material surface, causing displacement of material around the particle. There are two types of cutting: type I occurs when an angular particle impacts the material surface and rolls forward causing an indentation and raising the material; type II occurs when the impacting particle rolls backwards and cuts material from the surface. Ductile materials do not fail by fracture.

Ploughing

Type I cutting

Type II cutting
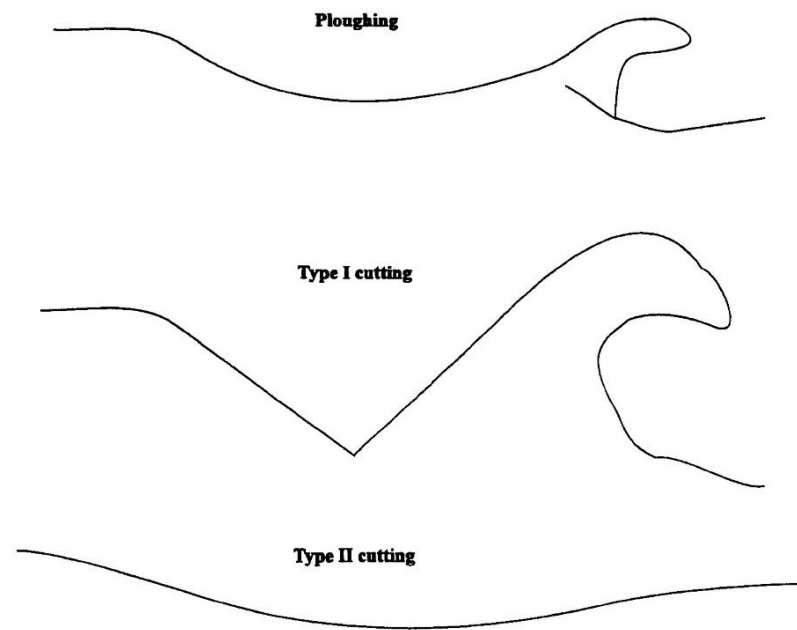
Figure 2.3: Ductile failure mechanisms (Hutchings, 1992)

Papadopoulos (1998) showed that the type of breakage experienced by a material can be best presented by the Schuhmann Jr (1940) plot, where the cumulative size distribution of the broken particles subjected to impact varied with the impact velocity. The shape of the distribution curve corresponded to breakage either by chipping, fragmentation, or disintegration, presented in Figure 2.4. Chipping is the removal of small chips a material from its mother particle due to sub-surface lateral cracks. Fragmentation is a particle breaks into fragments due to the extension of radial and median cracks across the full of the particle. The particle size is normalised by dividing by the initial feed size.
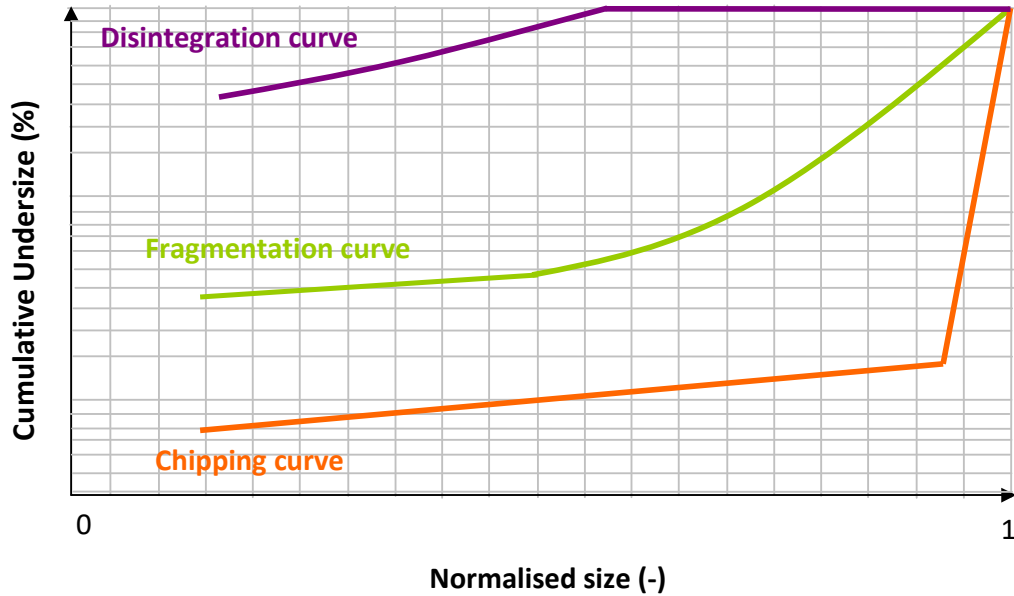
Figure 2.4: Cumulative size distribution corresponding to type of breakage (Papadopoulos, 1998)

2.2   Laser Diffraction Size Analysis

Laser diffraction is a popular method of particle size analysis, capable of measuring

sizes ranging from approximately 0.02 μm up to as large as 3 mm. It calculates the

particle size distribution of a whole powder sample based on the diffraction of the

laser light by the sample. Light from a laser source is emitted towards a detector.

The sample of material is dispersed and passes through the laser beam, leading to

diffraction (as well as absorption and refraction) of the light. The degree of

scattering of the diffracted light is dependent on the particle size. Large particles

scatter light at low angles with a high light intensity, while small particles scatter

light with a large angle and low light intensity. The scattered light is detected by

surrounding elements of the detector, and the intensity distribution of the light is

measured (Allen, 1997). Using the Mie or Fraunhofer theory, the measured light

scattering data are converted to a particle size distribution. The Fraunhofer theory

is the simpler of the two, and does not require any knowledge of the material

optical properties, namely its absorption and refractive index. This theory is
suitable for opaque, larger sized particles of at least 10 μm. For the analysis of
transparent particles below 10 μm, the more general Mie theory should be used.
This theory requires knowledge of the material optical properties. Laser diffraction
analysis gives the particle size distribution in the form of a volume based
distribution. Particles are assumed to be spherical, and so particle sizes are in the
form of their volume equivalent sphere diameter.

Laser diffraction is used to measure the particle size distribution of the milled
material in this study.

2.3   Computational Methods

2.3.1   Discrete Element Method

The Discrete Element Method (DEM) is a numerical simulation method for
predicting the motion of and interaction between particles in a granular assembly.
Cundall (1974) first developed the method to analyse problems involved in rock
mechanics, and later expanded it with help from Strack (Cundall and Strack, 1979).
They stated DEM was capable of realistically modelling the behaviour of particles
of any shape. Particulate behaviour is modelled using contact models, which
describe the force and local deformation of particles in contact with each other and
surrounding walls. The amount of research involving DEM and particulate
materials has greatly increased since its initial development by Cundall and Strack
(Zhu et al., 2007). In DEM interactions amongst neighbouring particles are
calculated at each integration step. Hence carrying out a simulation can be very
computationally intensive, especially where a large number of particles are

involved. This is the main factor preventing more extensive use of the method, however with the ever-improving performance and speed of computer systems combined with the work on simplified algorithms for DEM, the use and reliability of DEM will continue to increase.

Particle motion is modelled based on the forces arisen from direct and indirect contact between the individual particles. When particles come into contact with each other, the deformation of the particles is modelled by the amount of overlap, which influences their interaction force. These forces affect the movement of the particles. Particles have two main types of movement: translational and rotational. The motion is governed by Newton's second law of motion. The translational movement of particles is calculated using Eq. 2.1:

$$m\frac{dv_p}{dt} = F_g + F_c + F_{nc} \tag{2.1}$$

where v_p is the translational velocity, F_g is the gravitational force acting on the particle, and F_c and F_{nc} are the contact and non-contact forces between the particles and walls, respectively. The rotational movement is calculated using Eq. 2.2:

$$I\frac{d\omega_p}{dt} = M \tag{2.2}$$

where I is the moment of inertia, ω_p is the particle angular velocity, and M is the contact torque between particles and walls. Figure 2.5 shows a schematic diagram of the interaction between two particles and the forces involved.
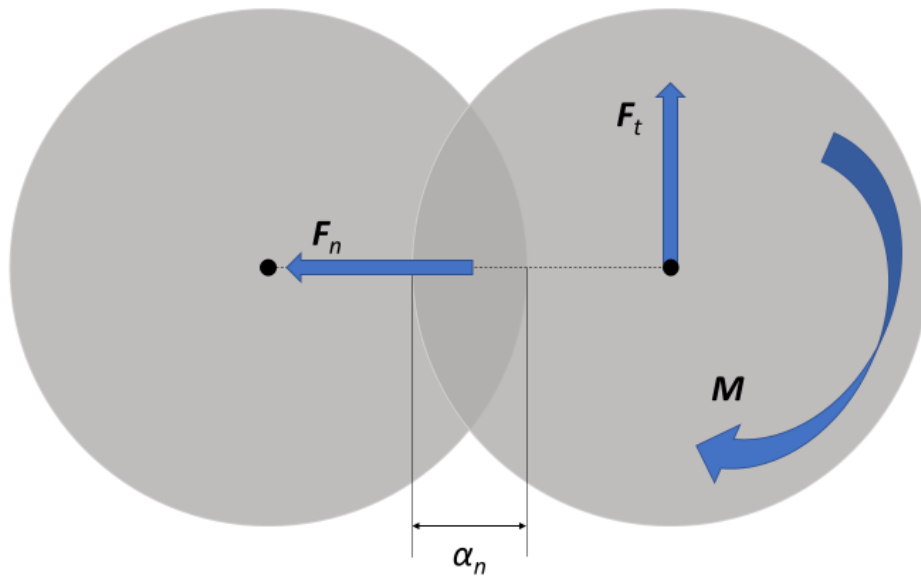
Figure 2.5: Schematic diagram of particle interaction in DEM, where F_n is the normal contact force, F_t is the tangential contact force, α_n is the normal overlap, and M is the contact torque

Both equations (Eqs. 2.1 and 2.2) are integrated at time intervals based on the time-step in order to calculate the velocity. It is assumed that there is no change in particle velocity within this time interval. The time-step of a simulation defines how often the calculations for particle interactions are conducted and is related to the speed of the Rayleigh surface wave propagation (Ning and Ghadiri, 2006). Ning and Ghadiri stated that the time-step should be sufficiently small, as compared to the transmission time of waves from the point of contact to the aft of the particle. The time-step should be less than the time it takes for the wave to travel through the smallest particle in the assembly. The time it takes for the wave to transverse is known as the Rayleigh time-step. This is calculated based on the material properties of the smallest particle in the simulation. DEM Solutions Ltd. (2015) detail the Rayleigh equation for the calculation of the Rayleigh time-step as follows:

$$T_R = \frac{\pi R_p \frac{\rho_p^{\frac{1}{2}}}{G}}{0.1631v + 0.8766} \tag{2.3}$$

where ρ_p is the particle density, R_p is the particle radius, G is the particle shear

modulus, and v is Poisson's ratio of the particle. A time-step of 20 % of the

Rayleigh time-step is generally acceptable for accurate simulations (DEM Solutions

Ltd., 2015).

2.3.1.1 Contact models

The force due to contact between particles leads to deformation at the point of

contact on each particle. This deformation is considered as an overlap between

the colliding particles for the modelling of particle interaction. Deformation can

be either elastic or plastic, and various models have been developed to model both

types of interaction. Models have also been developed to simulate the adhesion

behaviour of two particles which come into contact. The majority of these models

use perfectly spherical particles, as they are the simplest to model in computer

simulation.

The most common elastic contact model is the linear spring-dashpot contact

model originally proposed by Cundall and Strack (1979). In this model, the total

contact force applied to colliding particles is the summation of the normal contact

force and tangential contact force (Eq. 2.4).

$$\boldsymbol{F}_c = \boldsymbol{F}_n + \boldsymbol{F}_t \tag{2.4}$$

where $\boldsymbol{F}_n$ is the normal contact force and $\boldsymbol{F}_t$ is the tangential force. The normal

contact force is calculated using Hooke's Law (Eq, 2.5).

$$F_n = k_n \alpha_n + c\dot{\alpha} \tag{2.5}$$

where α_n is the normal overlap, c is the dashpot coefficient, and $\dot{\alpha}$ is the overlap velocity. The normal stiffness, k_n, used in EDEM software is calculated from Eq. 2.6:

$$k_n = \frac{16}{15} R_p^{*\frac{1}{2}} E^* \left(\frac{15 m^* v_C^2}{16 R^{*\frac{1}{2}} E^*} \right)^{\frac{1}{5}} \tag{2.6}$$

where R_p^* is the equivalent radius, E^* is the equivalent Young's modulus, m^* is the equivalent mass, and v_C is a used-defined characteristic velocity which is typical of the case being simulated (usually taken as the maximum velocity in the simulation). The equivalent radius is calculated using Eq. 2.7:

$$R_p^* = \left(\frac{1}{R_1} + \frac{1}{R_2} \right)^{-1} \tag{2.7}$$

where R_1 and R_2 are the radii of the first and second particles, respectively. The equivalent Young's modulus is calculated by Eq. 2.8:

$$E^* = \left(\frac{1-v_1^2}{E_1} + \frac{1-v_2^2}{E_2} \right)^{-1} \tag{2.8}$$

where E_1 and E_2 are Young's moduli of the first and second particles, respectively, and v_1 and v_2 are Poisson's ratios of the first and second particles, respectively. The equivalent mass is calculated by:

$$m^* = \left(\frac{1}{m_1} + \frac{1}{m_2} \right)^{-1} \tag{2.9}$$

where m_1 and m_2 are the masses of the first and second particles, respectively. The dashpot coefficient is calculated from:

14

$$c = \sqrt{\frac{4m^* k_n}{1+\left(\frac{\pi}{\ln e}\right)^2}} \qquad (2.10)$$

where e is the coefficient of restitution, which is the ratio of the particle's rebound velocity after impact to its velocity upon impact. The coefficient of restitution is the same for both normal and tangential velocities.

The tangential force is calculated as follows:

$$\boldsymbol{F}_t = \min(k_t \alpha_n + c_t \dot{\alpha}, \mu_f \boldsymbol{F}_n) \qquad (2.11)$$

where k_t is the tangential stiffness, which in EDEM is taken to be the same as the normal stiffness. c_t is the tangential dashpot coefficient. The tangential force is the minimum of two terms because the tangential force follows the Coulomb law of friction, where the tangential force cannot be greater than $\mu_f \boldsymbol{F}_n$.

2.3.1.1.1 Hertz-Mindlin "no slip" model

Hertz (1882) proposed a non-linear contact model for the force of two contacting elastic spheres in the normal direction. The normal contact force is calculated by Eq. 2.12:

$$\boldsymbol{F}_n = \frac{4}{3} E^* R_p^{*\frac{1}{2}} \alpha^{\frac{3}{2}} + \boldsymbol{F}_n^d \qquad (2.12)$$

In EDEM a damping force, $\boldsymbol{F}_n^d$, can be applied, which is calculated by:

$$\boldsymbol{F}_n^d = -2\sqrt{\frac{5}{6}} \beta \sqrt{k_n m^*} \boldsymbol{v}_n^{rel} \qquad (2.13)$$

where $\boldsymbol{v}_n^{rel}$ is the normal component of the relative velocity of the two contacting particles, and β and k_n are given by:

$$\beta = \frac{\ln e}{\sqrt{\ln^2 e + \pi^2}}$$

(2.14)

$$k_n = 2E^* \sqrt{R_p^* \alpha_n}$$

(2.15)

The Hertz model is frequently combined with the tangential force model of

Mindlin and Deresiewicz (1953). In EDEM software, a simplified version of the

HMD model is used, referred to as the Hertz-Mindlin 'no-slip' model. This model

is a combination of the Hertz normal force with Mindlin's theory of 'no-slip' in the

tangential direction (Mindlin, 1949). This model is used as the basis for tangential

forces in EDEM, where it is calculated as:

$$\boldsymbol{F}_t = -k_t \alpha_t + \boldsymbol{F}_t^d$$

(2.16)

where k_t is the tangential stiffness:

$$k_t = 8G^* \sqrt{R_p^* \alpha_n}$$

(2.17)

where G^* is the equivalent shear modulus, calculated from Eq. 2.18:

$$G^* = \left(\frac{1-v_1}{G_1} + \frac{1-v_2}{G_2} \right)^{-1}$$

(2.18)

where G_1 and G_2 are the shear moduli of the first and second particles, respectively.

The tangential damping force is calculated as:

$$\boldsymbol{F}_t^d = -2\sqrt{\frac{5}{6}} \beta \sqrt{k_t m^*} \boldsymbol{v}_t^{rel}$$

(2.19)

where $\boldsymbol{v}_t^{rel}$ is the relative tangential velocity. Rolling friction creates a resistance to

rotational movement of particles and is applied by the following modification to

Eq. 2.2:

$$I \frac{d\boldsymbol{\omega}_p}{dt} + \boldsymbol{\tau}_i = \boldsymbol{M} \tag{2.20}$$

$$\boldsymbol{\tau}_i = -\mu_r \boldsymbol{F}_n R_p \boldsymbol{\omega}_v \tag{2.21}$$

where μ_r is the rolling friction coefficient.

2.3.1.1.2 Pasha et al. (2014) model

There have been a few contact models developed for the simulation of elasto-plastic-adhesive behaviour, such as that by Ning (1995), Thornton and Ning (1998), Tomas (2007), and Luding (2008). Most of these models are intensive, requiring lengthy computational times. Pasha et al. (2014) developed a simplified linear contact model which simulates elasto-plastic-adhesive behaviour, based on the model of Thornton and Ning (1998). The model incorporates a linearised version of the Johnson, Kendell and Roberts (JKR) model which describes the adhesion behaviour of two contacting elastic particles (Johnson et al., 1971). It allows for realistic contact deformation while having a fast simulation time compared to other more rigorous non-linear elasto-plastic contact models. The schematic diagram of the force-overlap behaviour implemented into EDEM software is illustrated in Figure 2.6.
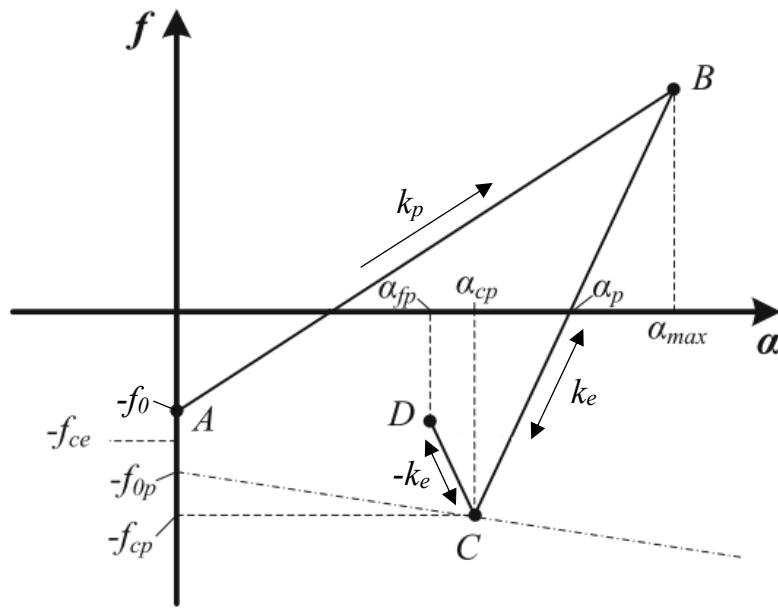
Figure 2.6: Schematic diagram of the normal force-overlap relationship in the Pasha et al. (2014) model

At initial contact the force between the two contacting particles falls to a negative

value, f_0, due to the van der Waals forces. f_0 is $8f_{ce}/9$, where f_{ce} is the JKR pull-off

force.

$$f_{ce} = -\frac{3}{2}\pi R_p^* \Gamma \tag{2.22}$$

where Γ is interface energy. At the initial loading, the contact deforms plastically

(line AB), governed by Eq. 2.23:

$$\boldsymbol{F}_n = k_p \alpha_n + f_0 \tag{2.23}$$

where k_p is the plastic stiffness. Unloading after plastic deformation will follow a

line governed by the elastic stiffness, k_e, as seen in the unloading line BC with Eq.

2.24:

$$\boldsymbol{F}_n = k_e(\alpha_n - \alpha_p) \tag{2.24}$$

Due to the plastic deformation, the contact area between the two particles will have increased, and so a greater force will be required to separate them. A new pull-off force is calculated, f_{cp}. Unloading beyond this pull-off force (line CD) is governed by Eq. 2.25:

$$\boldsymbol{F}_n = -k_e(\alpha_n - 2\alpha_{cp} + \alpha_p) \tag{2.25}$$

The model differs from other elasto-plastic-adhesive models in that reloading along DC and CB is reversible, following Eqs. 2.25 and 2.24, respectively. Reloading past the previous maximum force at point B leads to further plastic deformation. The tangential force is calculated as:

$$\boldsymbol{F}_t = \min\left(-k_t\alpha_t, \mu_f\left(|\boldsymbol{F}_n| + 2|f_{cp}|\right)\right) \tag{2.26}$$

Figure 2.7 illustrates the force-overlap relationship in the model when there is no adhesion. In this case, the initial loading is governed by Eq. 2.27:

$$\boldsymbol{F}_n = k_p\alpha_n \tag{2.27}$$

Unloading follows Eq. 2.24. Rolling friction is applied based on Eq. 2.20.
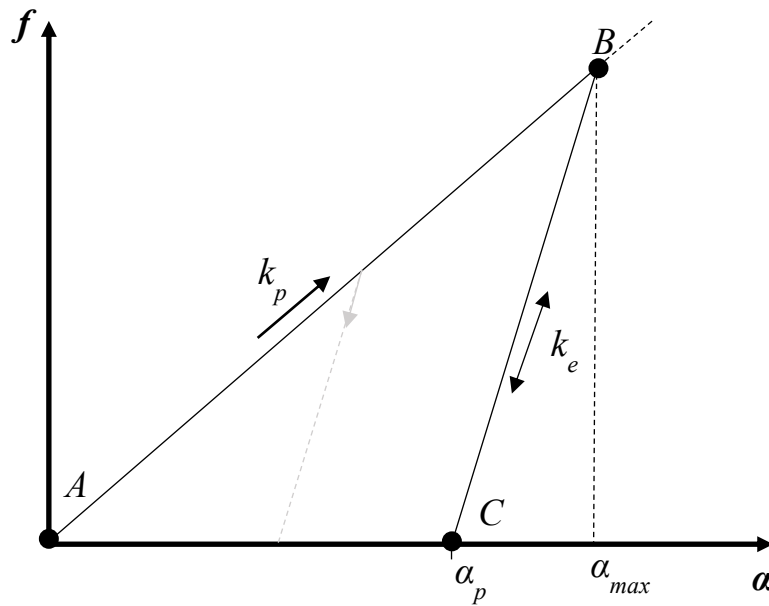
Figure 2.7: Schematic diagram of the normal force-overlap relationship in the Pasha et al. (2014) model with
no adhesion

2.3.2 Computational Fluid Dynamics

Computational Fluid Dynamics is the application of computers in solving problems

of fluid dynamics. The flow of fluids in reality is highly complex and is affected by

a number of different properties. The definition of these flows has been simplified

into equations based on a mixture of empirical equations and theory, and

computers are used for solving these equations. The governing principles are the

conservation of mass and momentum. These principles are typically applied to a

finite control volume. A control volume is a defined region of flow which can be

fixed in space with fluid passing through it, or moving with the fluid and having

the same fluid particles always contained within it. Calculations are applied to the

finite control volume rather than the whole fluid volume. The fundamental

equations for calculating the flow of viscous fluids, derived from the governing

principles, are known as the continuity and Navier-Stokes equations. Numerically

solving these equations is known as Direct Numerical Simulation, which is a very

computationally intensive process, especially for large, highly turbulent cases. The

time-averaged form of these equations is usually solved instead, which is known as

the Reynolds averaged Navier Stokes (RANS) equation. This is derived by breaking

up the instantaneous velocity which randomly fluctuates into the time-average and

fluctuating quantity (Eq. 2.26).

$$u_i = \bar{u}_i + u_i' \tag{2.28}$$

where u_i is the fluid velocity, $\bar{u}_i$ is the time-average velocity component, and u_i' is

the fluctuating component. The time-average continuity equation is given as Eq.

2.27:

$$\frac{\partial \rho_F}{\partial t} + \frac{\partial}{\partial x_i}(\rho_F \bar{u}_i) = \bar{S}_m \tag{2.29}$$

where ρ_F is the fluid density, t is time, and $\bar{S}_m$ is the source term arising from the

exchange of mass. In this study, $\bar{S}_m$ is zero. The RANS equation is given by (Eq.

2.28):

$$\frac{\partial}{\partial t}(\rho_F \bar{u}_i) + \frac{\partial}{\partial x_i}(\rho_F \bar{u}_i \bar{u}_j) = \frac{\partial}{\partial x_i}\left[\mu\left(\frac{\partial \bar{u}_i}{\partial x_j} + \frac{\partial \bar{u}_j}{\partial x_i}\right)\right] - \frac{\partial p}{\partial x_j} + \frac{\partial}{\partial x_i}\left(-\rho_F \overline{u_i' u_j'}\right) + \boldsymbol{F}_b + \boldsymbol{F}_s \tag{2.30}$$

where the term $-\rho_F \overline{u_i' u_j'}$ is the Reynolds stress, which is modelled using what are

known as turbulence models, $\boldsymbol{F}_b$ is the gravitational body force, and $\boldsymbol{F}_s$ is the source

term for momentum transfer. More details of CFD procedures are given in Chapter

6.

Chapter 3 Breakage Test Materials

Three materials were used in this research: acetylsalicylic acid (more commonly known as aspirin), paracetamol, and α-lactose monohydrate. These were selected due to them being very popular APIs and excipient used within the pharmaceutical industry, and therefore will be easily available in large quantities for milling. They were supplied by WeylChem in Germany, Kraemer & Martin in Germany, and DMV International in The Netherlands, respectively. Previous studies of these materials also suggest that they will break to a measureable extent under single impact testing.

Aspirin ($C_9H_8O_4$) is a nonsteroidal anti-inflammatory drug, commonly used as a painkiller. It is a white, semi-brittle material that has a monoclinic crystal structure, and can be seen in Figure 3.1. Previous studies have shown that it breaks preferentially along slip and cleavage planes at the (100) and (001) planes, respectively (Olusanmi et al., 2011). The mechanical properties of Young's modulus, hardness and fracture toughness of aspirin have been measured as 5.17 GPa, 0.12 GPa, and 0.0252 MPa·m$^{1/2}$, respectively (Olusanmi, 2009).

LEMAS 2.0kV 7.8mm x40 LM(L)   1.00mm
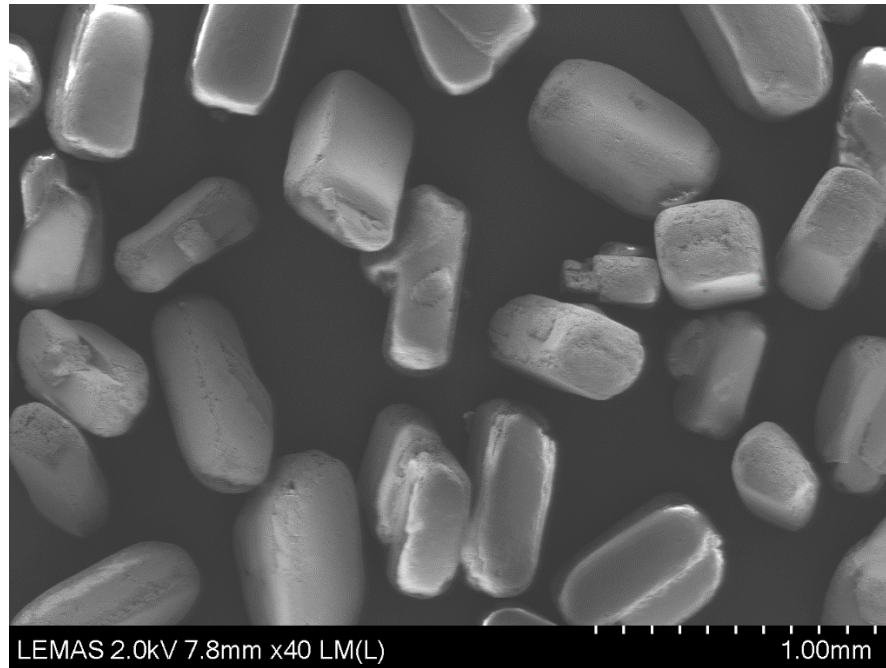
Figure 3.1: SEM image of aspirin sieved to size range 425 – 500 µm

Paracetamol ($C_8H_9NO_2$) is also a nonsteroidal drug used as a painkiller, and its SEM image is shown in Figure 3.2. It is a semi-brittle material and, as with aspirin, has a monoclinic crystal structure. Paracetamol has a slip plane on (010) (Hare, 2010). Prasad et al. (2001) also showed there is preferential breakage along the cleavage plane (010). The Young's modulus, hardness and fracture toughness have been reported to be 10.9 GPa, 0.44 GPa, and 0.05 MPa·$m^{1/2}$, respectively (Prasad et al., 2001; Finnie et al., 2001).
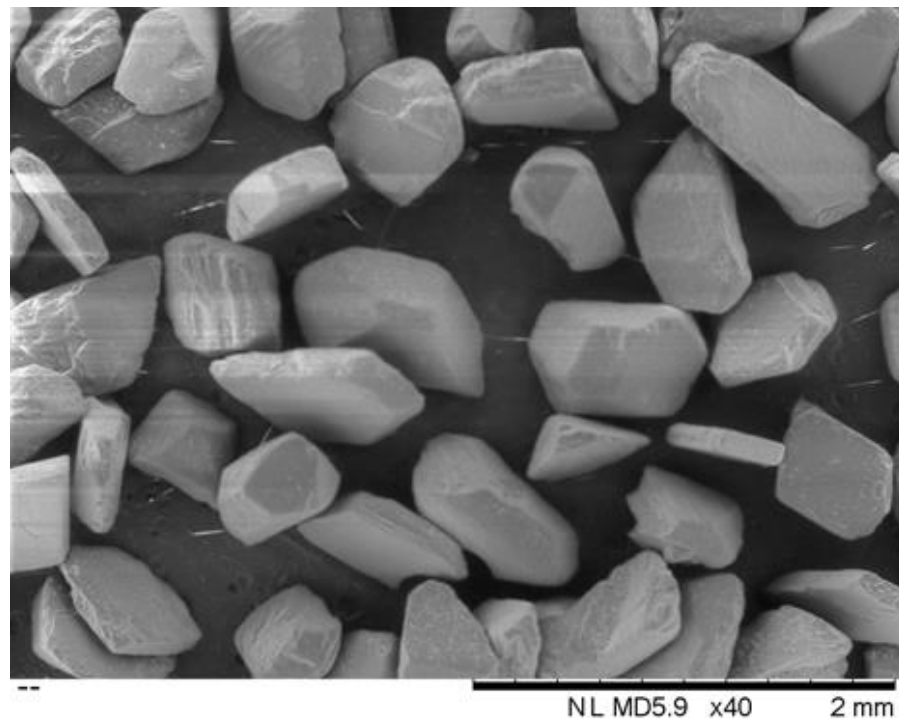
Figure 3.2: SEM image of paracetamol sieved to size range 425 – 500 μm

α-lactose monohydrate ($C_{12}H_{22}O_{11}$) is a disaccharide sugar found in milk. It is used as a filler or diluent in tablets and dry powder inhalers. The alpha form is the most stable of the four lactose variants. α-lactose has a tomahawk crystal shape, with no known cleavage planes. An SEM image of the crystals is displayed in Figure 3.3. Olusanmi (2009) measured the Young's modulus, hardness and fracture toughness as 21.4 GPa, 0.89 GPa and 0.0908 MPa·m$^{1/2}$, respectively.
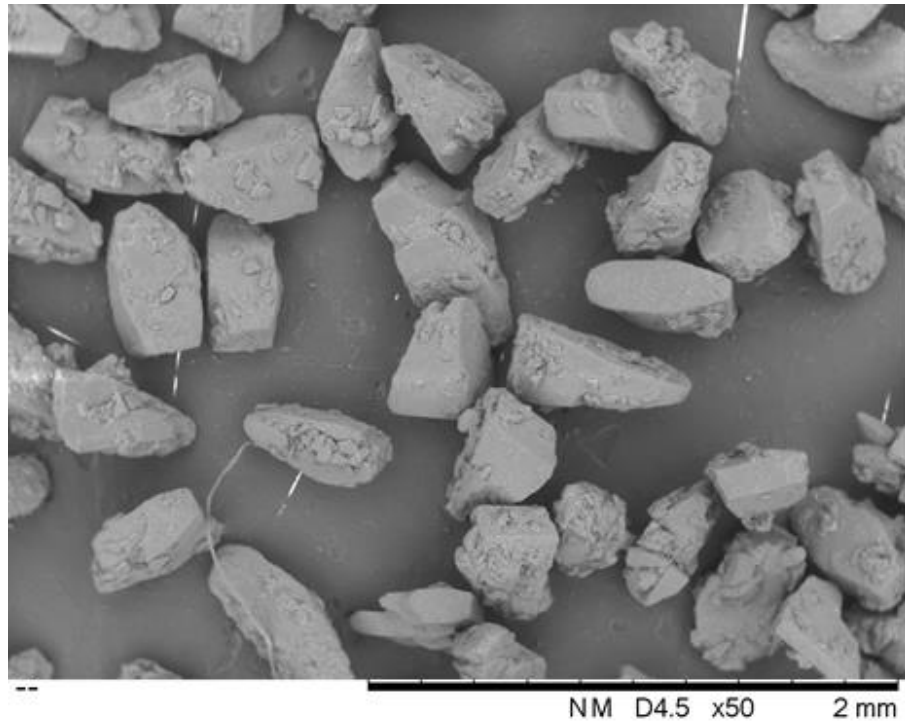
Figure 3.3: SEM image of α-lactose monohydrate sieved to size range 300 – 355 μm

A summary of the mechanical properties of the three materials can be seen in Table 3.1.

Table 3.1: The mechanical properties of aspirin, paracetamol, and α-lactose monohydrate

Material	Young's modulus (GPa)	Hardness (GPa)	Fracture toughness ($MPa \cdot m^{1/2}$)
Aspirin	5.17	0.12	0.025
Paracetamol	10.90	0.44	0.050
α-lactose monohydrate	21.40	0.89	0.091

Chapter 4 Single Particle Impact Testing

4.1   Introduction

The degree of size reduction of particulate materials is governed by various factors. One of the most important factors is the mechanical properties of the material itself. The stiffness, hardness and fracture toughness of a material will all affect the mode and extent of material breakage. The breakage of a particle subjected to single impact is a broadly studied phenomenon. Single impact breakage of materials occurs at high strain rates, making the approach beneficial for investigating high velocity processes such as milling. The investigation of breakage of a single particle allows for a more targeted analysis of a material behaviour due to its properties as compared to particle breakage in a bulk assembly which can be subject to the conditions of the bulk such as the number of particles present.

In this chapter, pharmaceutical materials are subjected to single impacts using the Single Particle Impact Rig. Their extent of breakage is measured using sieving, from which their mechanical properties are inferred in the form of a lumped parameter known as the "breakability index", using the Ghadiri and Zhang semi-brittle breakage model (Ghadiri and Zhang, 2002). The breakability index gives a measure of how readily the material breaks.

4.2   Review of Single Particle Impact Testing

There has been extensive research on the single impact behaviour of numerous different types of materials in recent times, i.e. over the last two decades. Papadopoulos and Ghadiri (1996) looked at the single impact of poly-methylmethacrylate (PMMA) polymer particles. Subero-Couroyer et al. (2005)

26

investigated the breakage strength of alumina catalyst beads by single impact. Salman and Gorham (1997, 2000) carried out the single impact of glass spheres. Seipenbusch et al. (2007) studied the breakage of nanoparticle agglomerates. Ali et al. (2015) examined the single impact behaviour of burkeite powder. Single impact testing has also been used to investigate the breakage behaviour of pharmaceutical materials by several researchers, including Kwan et al. (2004), Bentham et al. (2004), Yang et al. (2007), Meier et al. (2008), and Olusanmi et al. (2010). These materials include microcrystalline cellulose, α-lactose monohydrate, paracetamol, and sucrose amongst others.

A few models have been developed to represent particle breakage in a quantitative form. The most widely used is the breakage probability function developed by Vogel and Peukert (2003, 2004, 2005), which uses the work of Rumpf (1973) and Weibull (1951). Rumpf established a relationship between initial particle size and elastic strain energy by assuming that there is a similarity in the geometry of particles undergoing breakage, and a similarity in the states of stress and strain. By applying Weibull statistics for flaw size distribution with the laws of fracture mechanics, as previously done by Weibull (1951), the same correlation found by Rumpf can be obtained. Vogel and Peukert simplified these two approaches to reach the following equation:

$$S = 1 - \exp\{-f_{Mat}D(W_{m,kin} - W_{m,min})\} \tag{4.1}$$

where S is the breakage probability, f_{Mat} is the resistance of particle material against volume specific external stressing energy, $W_{m,kin}$ is the mass specific impact kinetic energy of particles, $W_{m,min}$ is the specific threshold energy needed to cause fracture

in a particle, and D is the particle size. Vogel and Peukert verified the model using seven different materials with particle sizes ranging from 95 μm up to 8 mm. They found that the breakage probability of the materials can be represented with a single mastercurve. The main drawback of the model is that it does not give a measure of breakage, but rather the chance of it occurring. It also does not give an indication of the type of breakage, whether it is chipping or fragmentation. While the function was initially developed for and validated using brittle materials, it has been found to work also with semi-brittle materials. Meier et al. (2008) used the model to successfully describe the impact breakage of pharmaceutical powders including lactose monohydrate, sucrose and aspirin. Pharmaceutical powders most commonly exhibit semi-brittle behaviour. The materials were found to fall on the mastercurve of Vogel and Peukert (2003). However there is a large standard deviation in the results of some of the materials, bringing the suitability of the model into question.

de Vegt et al. (2005a) developed a breakage probability function for the milling of organic material in a jet mill using dimensional analysis of the parameters found to be important for breakage in fracture mechanics.

$$S = c \frac{E_{kin} E_{fract} \sqrt{\frac{P_y}{\rho_p}}}{V_p H \sqrt{D} K_c} \left(\frac{\ell}{D}\right) \tag{4.2}$$

where c is a constant, E_{kin} is the kinetic energy of the particles, E_{fract} is the fracture energy, P_y is the yield pressure, V_p is the particle volume, H is the hardness, K_c is the fracture toughness, and ℓ is the flaw length. Despite being designed to investigate bulk milling, the model uses parameters involved in individual particle

breakage. de Vegt et al. (2005b) validated the model by carrying out experiments in a fluidised bed opposed jet mill with five materials: α-lactose monohydrate, paracetamol, two heterocyclic compounds (Org 12962 and one unnamed), and a steroid (Add-Neop). They found that the model can be used to compare the rates of breakage of different materials, thus showing their relative milling behaviours. α-lactose monohydrate has the lowest rate of breakage compared to the other materials. While the model includes the main mechanical properties responsible for breakage of a material, again it does not give a measure of breakage. The model also under-predicts the degree of fracture of fine particles, and over-predicts that of coarser particles.

An alternative approach has been developed by Ghadiri and Zhang (2002) based on indentation fracture mechanics for the breakage of semi-brittle materials, revolving around the fact that the formation of cracks at the corner of impacted particles are similar to their formation by indentation of a flat surface by an indenter. The material lost from the corners of the impacted particle is assumed to have dimensions equivalent to the length of the subsurface lateral cracks and the depth at which the crack is formed. The model defines the extent of breakage of a material as a function of the impact velocity, particle diameter, particle density and the material mechanical properties:

$$R^* = \alpha \eta = \alpha \frac{\rho_p v^2 D H}{K_c^2} \tag{4.3}$$

where R^* is the extent of breakage, α is the proportionality constant which represents the influence of the geometry of chipping, η is the attrition propensity parameter, v is the impact velocity, and K_c is the fracture toughness. The Ghadiri

and Zhang model was specifically developed to describe breakage via chipping, and incorporates all the mechanical properties important for semi-brittle breakage, making it an ideal model for use with semi-brittle materials such as pharmaceutical powders.

The extent of breakage can be defined in a number of ways depending on how the losses are taken into account. One way is to define it as the ratio of the mass of debris (broken) particles to the total mass of material collected from the impact rig:

$$R^* = \frac{M_{de}}{M_{de} + M_m} \times 100 \qquad (4.4)$$

where M_{de} is the mass of debris particles, and M_m is the mass of mother particles. Debris is considered to be any particle whose size is less than two British standard sieve sizes below the feed particle size. By considering only the material that is collected from the impact rig, the extent of breakage calculation takes into account material losses of both mother and debris particles during handling. There are two alternative ways which describe the upper and lower limits of breakage, depending on whether the losses are attributed to the debris or to the mother particles. The calculation of the extent of breakage for cases where the mother particles are lost during handling:

$$R^- = \frac{M_{de}}{M_f} \times 100 \qquad (4.5)$$

where M_f is the mass of feed particles. For cases where losses are mainly from the debris particles, the extent of breakage can be calculated as follows:

$$R^+ = \frac{M_f - M_m}{M_f} \times 100 \qquad\qquad (4.6)$$

This approach was used by Papadopoulos and Ghadiri (1996) in their study of PMMA particle breakage. Zhang and Ghadiri (2002) impacted ionic crystals to verify the model described by Eq. 4.3. Ali et al. (2015) used the same rig and model for the mechanical properties of burkeite. In regards to pharmaceutical materials, Bentham et al. (2004) characterised the breakability indices of α-lactose monohydrate and paracetamol using the model. It should be noted that they impacted particles sieved into the range of 300 – 500 μm rather than sieving particles into British standard single sieve sizes, i.e. 300 – 355 μm, 355 – 425 μm, and 425 – 500 μm. They then separated the debris from the mother particles using a 212 μm sieve. By doing this, they would measure a lower extent of breakage than if they sieved the particles into three British standard sieve cuts and separated debris using the three corresponding lower sized sieves (212 μm, 250 μm, and 300 μm). Olusanmi et al. (2010, 2011) used the single particle impact rig with the Ghadiri and Zhang model to measure the extent of breakage and infer the breakability indices of aspirin and sucrose, although they carried out the majority of their impacts at high velocities of over 16 m/s which produced fragmentation rather than falling in the chipping regime. Kwan et al. (2004) inferred the breakability of microcrystalline cellulose and α-lactose monohydrate. Table 4.1 lists the breakability indices achieved from the previous investigations of pharmaceutical materials.

Table 4.1: Breakability indices of pharmaceutical materials from previous literature

Material	$\alpha H/Kc^2$	Source
Paracetamol	0.0539	*(Bentham et al., 2004)*
Aspirin	0.0373 *(impact velocity < 14 m/s)* 0.0641 *(impact velocity > 16 m/s)*	*(Olusanmi et al., 2011)*
α-lactose monohydrate	0.007	*(Bentham et al., 2004)*
	0.0069	*(Kwan et al., 2004)*

From Eq. 4.3 it can be seen that if the mechanical properties of the impacted material are grouped together, there exists a linear relationship between $\rho D v^2$ and the extent of breakage. Plotting the extent of breakage against $\rho D v^2$ produces a line with the gradient of $\alpha H/K_C^2$ if the model fits the experimental data. This is shown in Figure 4.1, which presents the breakage results of Bentham et al. (2004) for α-lactose monohydrate. $\alpha H/K_C^2$ is known as the breakability index, and describes how readily materials break to form chips in relation to each other. The greater the breakability index, the more readily a material breaks. If a line of best fit is drawn through the linear section of the curve, the line will cross the x-axis and the x-intercept is regarded as the point at which breakage begins to occur.
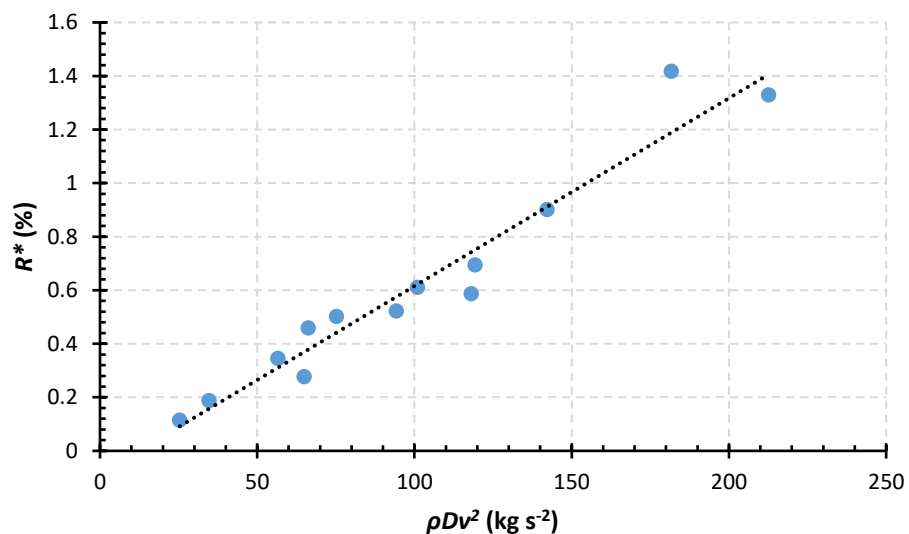
Figure 4.1: Extent of breakage of α-lactose monohydrate as a function of $\rho D v^2$ (Bentham et al., 2004)

32

4.2.1 Summary

Single particle breakage is a well-studied area of particle science, with there being several attempts made to predict the breakage behaviour of particles. This has been investigated for materials with differing modes of breakage, including brittle and semi-brittle. Particulate materials are commonly used in bulk conditions in large quantities, particularly in milling operations; it would be of great benefit to relate the single particle breakage properties of a material to its bulk behaviour. Single particle impact testing also possesses benefits over other material property characterisation techniques as its high strain rates give it a better relevance to processes such as milling.

4.3 Experimental Test Method for Single Particle Impact Breakage

Single impact testing was carried out using the Single Particle Impact Rig at the University of Leeds, pictured in Figure 4.2. The impact rig allows for individual particles to collide with a rigid sapphire target at a pre-set angle. As the single particle travels down the impact tube, it passes two photodiodes separated by a known distance. The time for the particle to pass the two diodes is recorded and the particle velocity is calculated. This velocity is regarded as the impact velocity. The collection chamber of the rig is connected to a vacuum line, and the pressure can be changed to set the impact velocity.
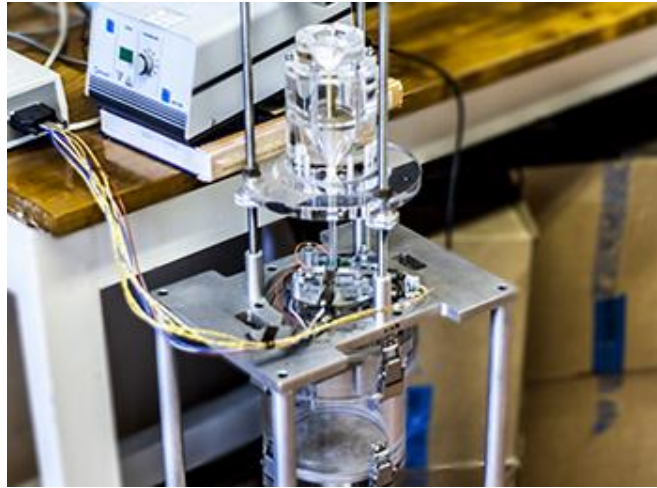
Figure 4.2: Single Particle Impact Rig

Three materials were impacted in the rig: aspirin, paracetamol and α-lactose monohydrate. Table 4.2 lists the different particle feed sieve cut sizes used for each material; particles were hand sieved using British standard sized sieves. 2 g of material was weighed and singly fed into the single impact rig at various velocities using the Retsch vibratory feeder DR 100 (Retsch GmbH, Germany). This mass of material leads to a significantly large number of single particle impacts. The velocities were selected so as to be within the chipping breakage regime of the materials. This ranged between free-fall velocity (≈ 1.5 m/s) and 25 m/s. The impacted material was then collected and hand sieved using British standard sieves to separate the debris and mother particles. As previously mentioned, debris is considered as particles less than two British standard sieve sizes below the particle feed size. The debris sieve size for each feed is detailed in Table 4.2.

Table 4.2: The feed sizes of aspirin, paracetamol and α-lactose monohydrate impacted in the single particle rig in this investigation (the debris sieve size is given in brackets)

Material	Aspirin	Paracetamol	α-lactose monohydrate
Feed sizes (μm) [Debris size]	300 – 355 [212] 355 – 425 [250] 425 – 500 [300]	355 – 425 [250] 425 – 500 [300] 500 – 600 [355]	300 – 355 [212] 355 – 425 [250] 425 – 500 [300]

4.4   Results of Single Particle Impact Testing

4.4.1   Single Particle Impact Breakage of Paracetamol

Before carrying out impact testing, the velocity range in which chipping occurred was identified. This was done by carrying out single impact testing at various velocities, and then sieving the impacted material on British standard sieves. Six sieves were used: the particle feed sieve size and the five sieve sizes below. The mass on each sieve was weighed and plotted into a Schuhmann plot, as described in Figure 2.4.

By using the Schuhmann plot the transition from chipping to fragmentation can be seen to occur around an impact velocity of 22 m/s, as shown in Figure 4.3. Therefore, only impact results at velocities lower than this were used to infer the breakability index. A normalised particle size, which is the ratio of the average particle size through the sieve to the feed particle size, is used in Figure 4.3.
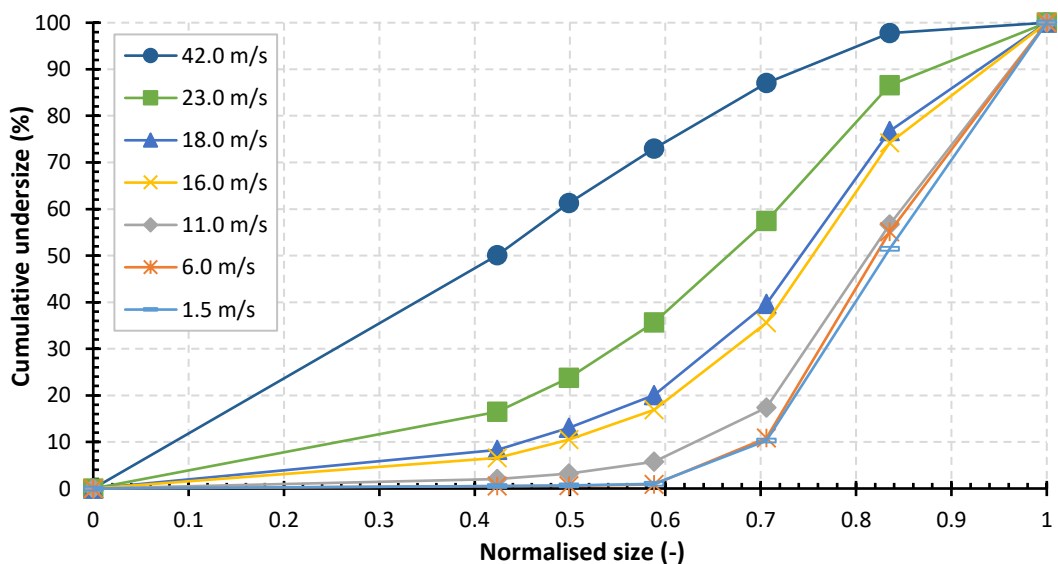
Figure 4.3: Schuhmann plot for impact breakage of paracetamol of sieved size 500 - 600 μm

The extent of breakage of paracetamol at low impact velocities was found to vary linearly with ρDv^2, as shown in Figure 4.4. There was very good unification of the curves of different particle sizes, with the R-squared value being 0.999. This shows that the mechanical properties of paracetamol are independent of its particle size. From the impact results, paracetamol was found to have a breakability index of 0.0841.
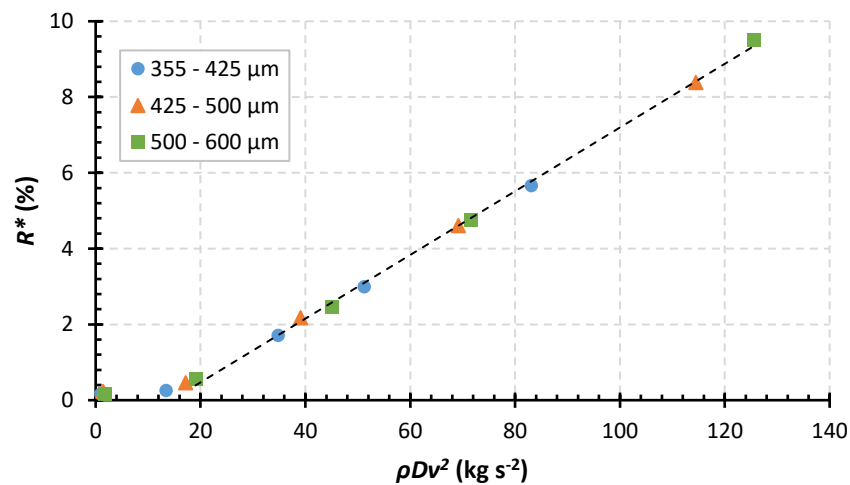
Figure 4.4: Extent of breakage of paracetamol as a function of ρDv^2

From Figure 4.4, the x-intercept of the line of best fit is the point at which breakage of paracetamol begins. From this, the minimum velocity to cause breakage can be inferred. This velocity is size dependent, with larger particles having a lower minimum breakage velocity. It is found to have a linear relationship with D^{-2}, as shown in Figure 4.5.
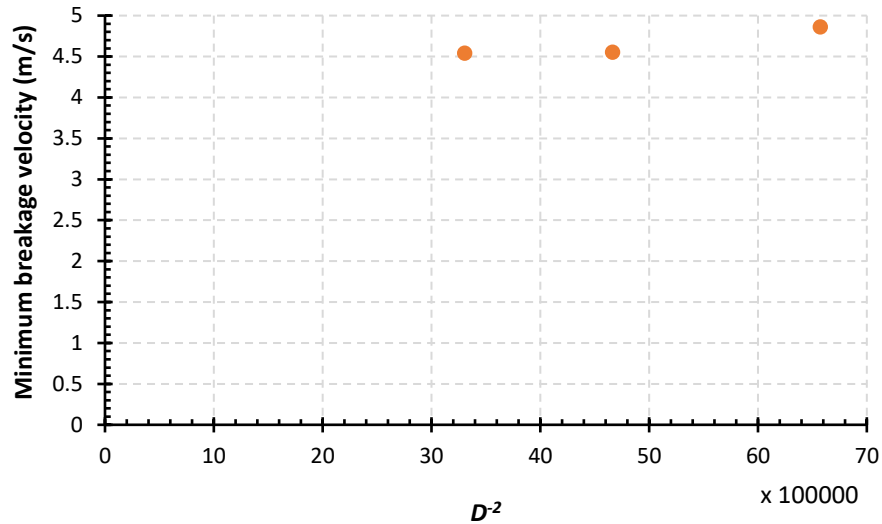
Figure 4.5: The minimum breakage velocity for paracetamol as a function of D^{-2}

4.4.2 Single Particle Impact Breakage of Aspirin

Initial testing found the chipping-fragmentation transition to be around 26 m/s, illustrated by the Schuhmann plot in Figure 4.6.
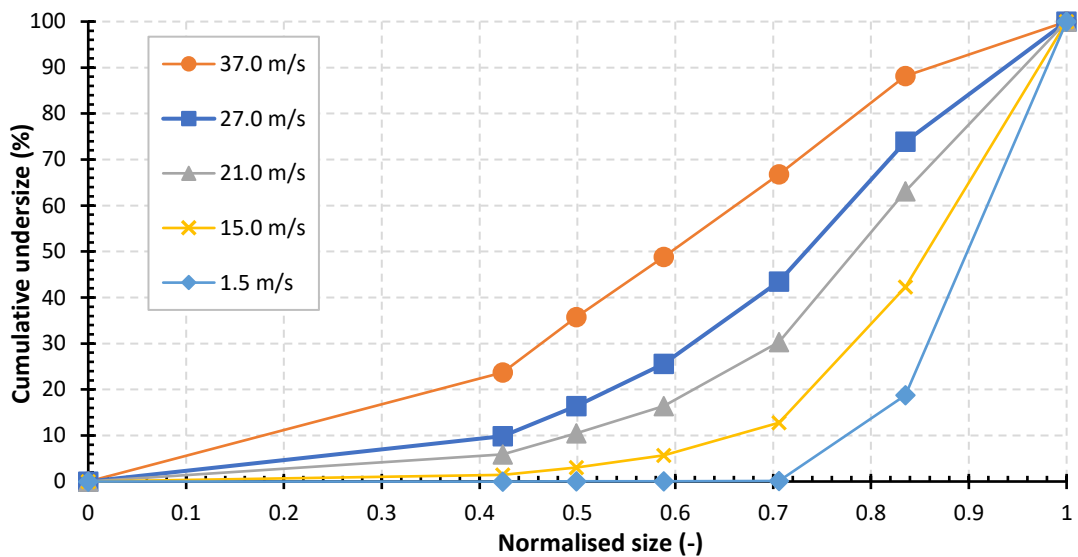
Figure 4.6: Schuhmann plot for impact breakage of aspirin of sieved size 425 - 500 μm

Figure 4.7 shows the results of the single particle impact of aspirin. The impact test results of aspirin show a good unification, with the R-squared value being 0.967. The breakability index was found to be 0.0534.
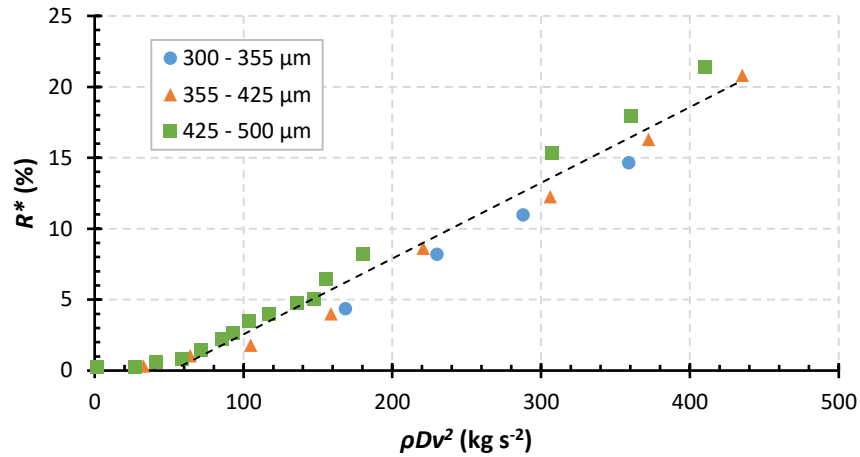
Figure 4.7: Extent of breakage of aspirin as a function of ρDv^2

Figure 4.8 shows the relationship between the minimum breakage velocity and D^{-2}

for aspirin, which is found to vary linearly.
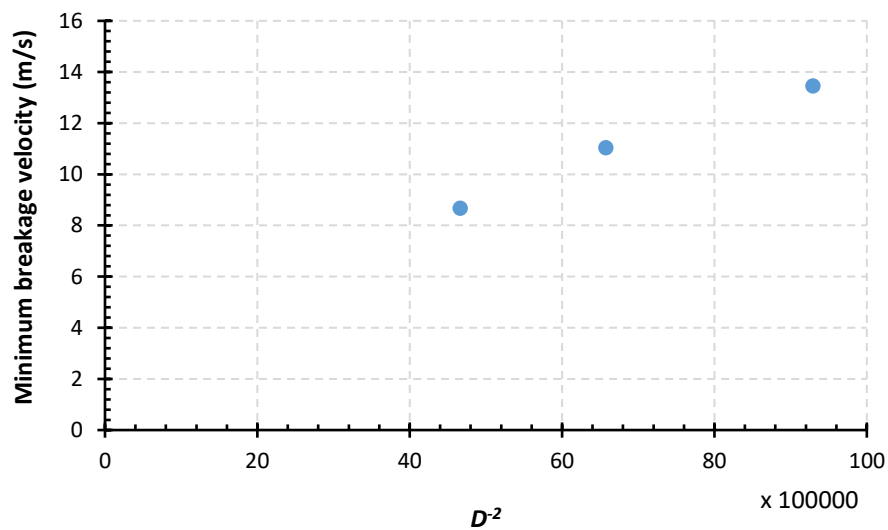
Figure 4.8: The minimum breakage velocity for aspirin as a function of D^{-2}

4.4.3   Single Particle Impact Breakage of α-Lactose Monohydrate

Analysis of the Schuhmann plot in Figure 4.9 suggests that up to the highest tested

impact velocity of 42 m/s, breakage of α-lactose monohydrate is still occurring in

the chipping regime.
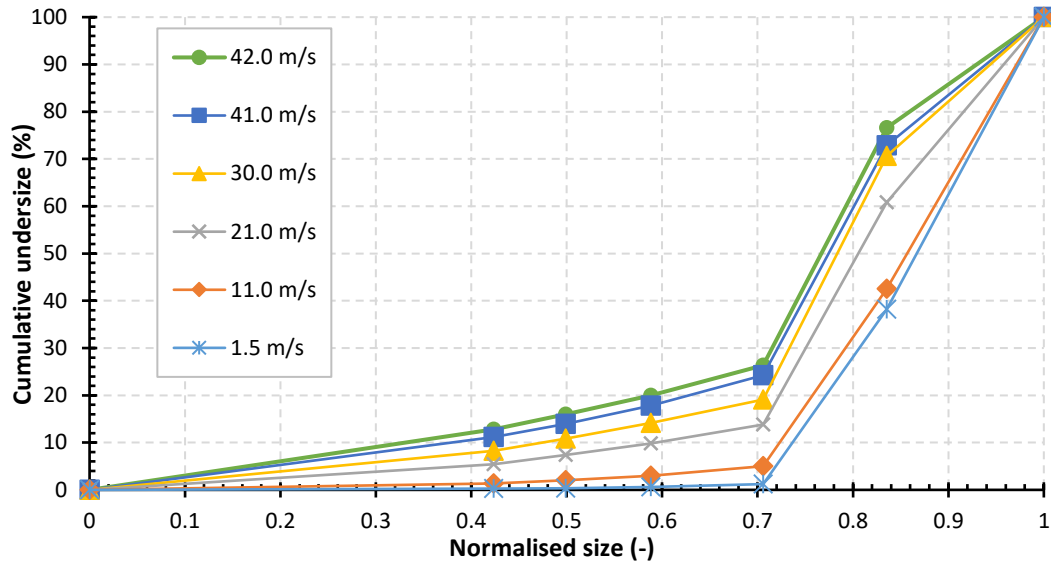
Figure 4.9: Schuhmann plot for impact breakage of α-lactose monohydrate of sieved size 425 - 500 µm

Single impact results show a near unification of particle sieve cuts 300 – 355 and

355 – 425 µm, visible in Figure 4.10. The line for the larger size of 425 – 500 µm,

however, is some distance away from the other two sizes, with it having an extent

of breakage almost three times greater than the smallest tested sieve cut of 300 –

355 µm. The graph seems to suggest that the lines intercept the y-axis, implying

that there is breakage at a velocity of 0 m/s. However this is not the case; there is

a jump in the extent of breakage of the particles sized 425 – 500 µm. The lowest

tested impact velocity (free-fall, approximately 1.4 m/s) yielded breakage extents

of 0.2, 0.6, and 2.1 % in particle sizes 300 – 355, 355 – 425, and 425 – 500 µm,

respectively. This is shown more clearly in Figure 4.11. The breakability index was

found to be 0.0179.
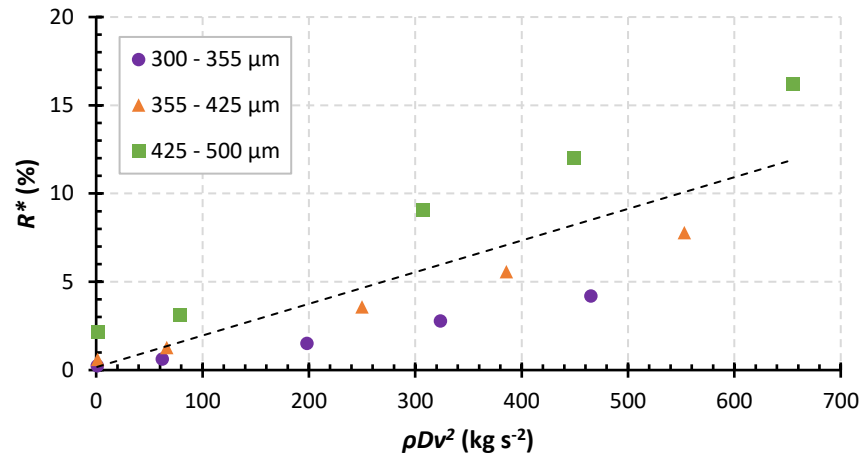
Figure 4.10: Extent of breakage of α-lactose monohydrate as a function of ρDv^2
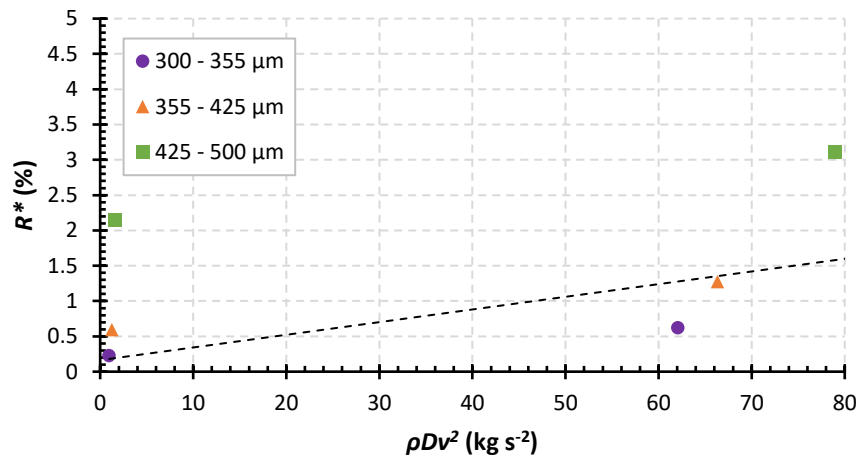
Figure 4.11: Extent of breakage of α-lactose monohydrate as a function of ρDv^2 at the lowest impact conditions

Looking at the extent of breakage caused by impact at different velocities, shown in Figure 4.12, the minimum impact velocity for breakage occurs at a much lower velocity for particle sieve size 425 – 500 μm compared to sizes 300 – 355 μm and 355 – 425 μm.
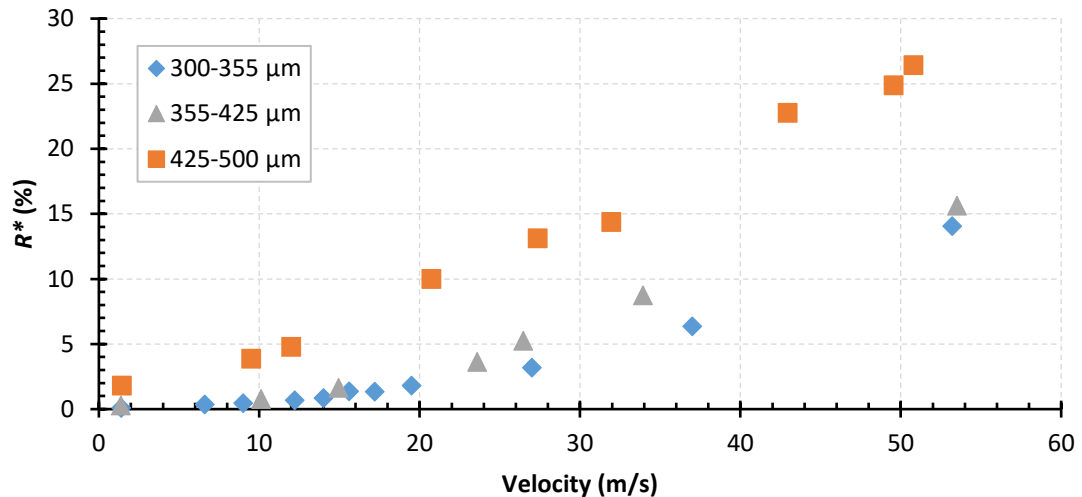
Figure 4.12: Extent of breakage as a function of the impact velocity of α-lactose monohydrate

Figure 4.13 shows that α-lactose monohydrate is quite a dusty material, with larger sized particles having smaller, sub-50 μm lactose particles attached to their surface which may contribute towards the jump seen in the extent of breakage shown in Figure 4.11. In order to prevent these small particles from contributing to the measured breakage extent, the α-lactose monohydrate was washed. The particles were poured into a beaker containing distilled water in order to dissolve the fine debris on the surface of the larger crystals, and then immediately poured out into a sieve and rinsed with propan-2-ol. Once dried, they were subjected to single impact testing.
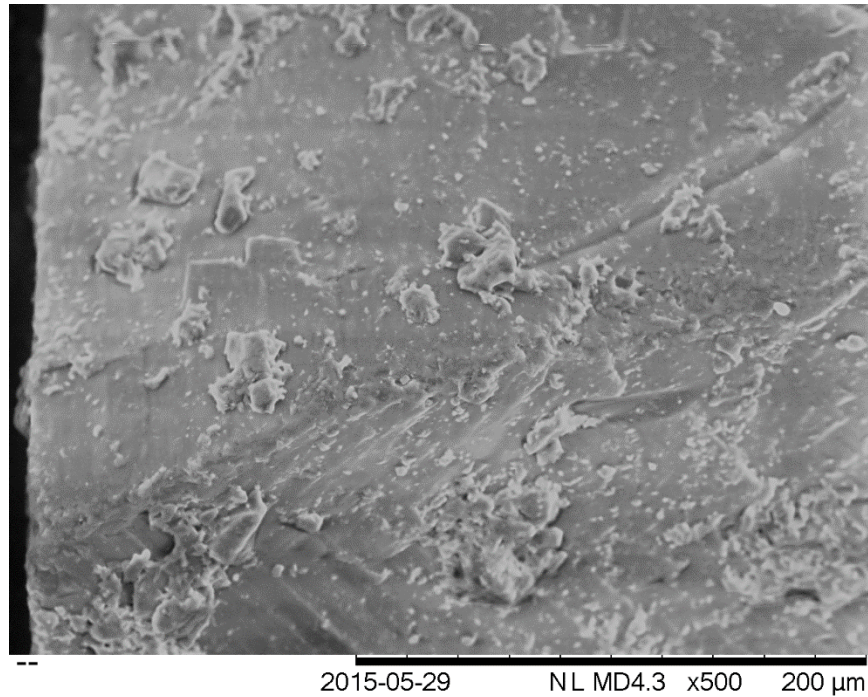
Figure 4.13: SEM image of the surface of an unwashed α-lactose monohydrate particle

After washing, α-lactose monohydrate was found to have a smoother surface with the majority of the fine particles removed, as shown in Figure 4.14.
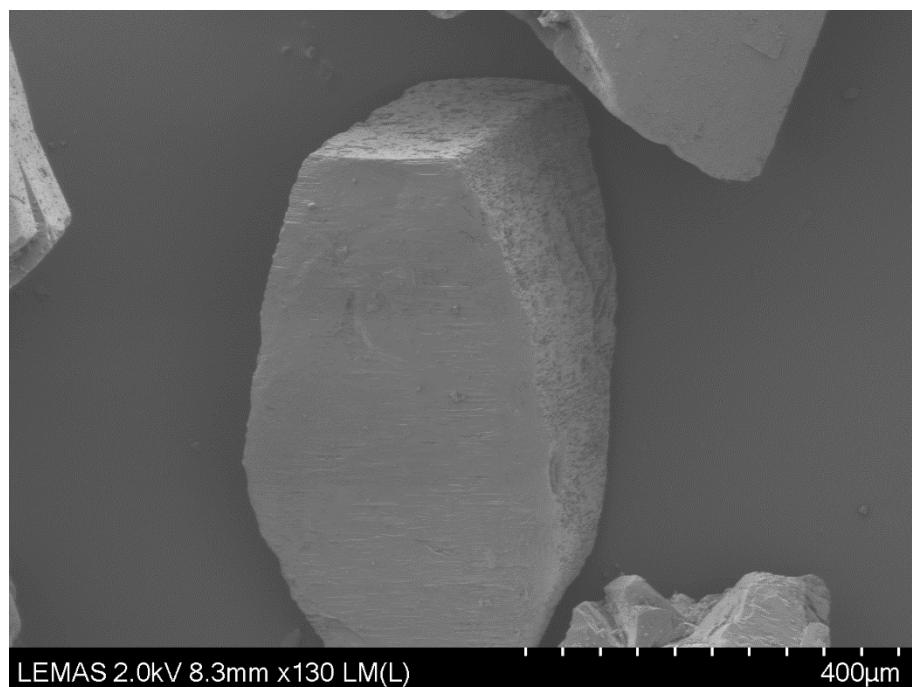
Figure 4.14: SEM image of the surface of α-lactose monohydrate after washing with water and propan-2-ol

Despite the cleaner particle surface, washing of α-lactose monohydrate was found to cause an increase in the extent of breakage of all tested sizes of the material, as can be seen in Figure 4.15. This implies that the washing process of α-lactose monohydrate weakens the material. The breakability index of the washed α-lactose monohydrate was found to be 0.0194.
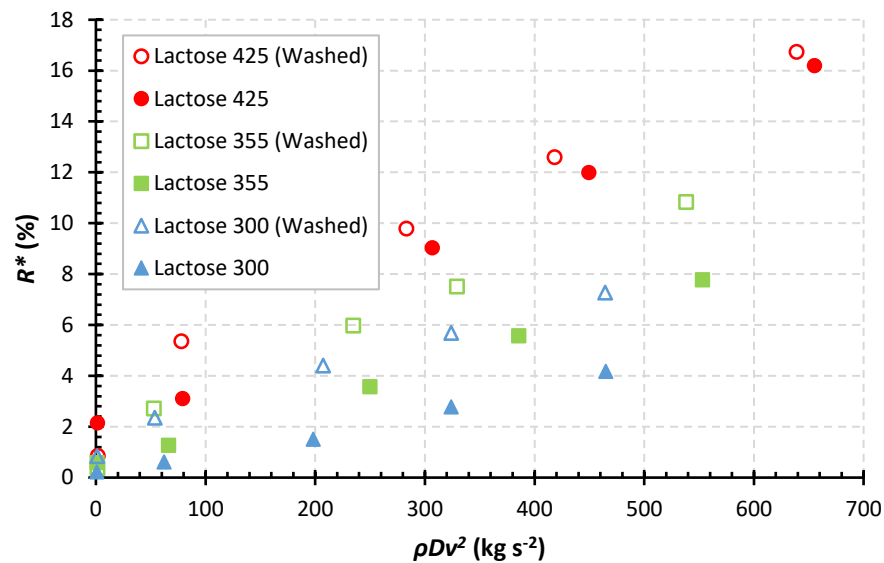
Figure 4.15: Comparison of the extent of breakage of washed and unwashed α-lactose monohydrate as a function of $\rho D v^2$

Using the Malvern Mastersizer 2000, the size distribution of the unwashed α-lactose monohydrate was measured. As can be seen in Figure 4.16, the results show that there is no peak in the curve at sizes below 200 μm for any of the particle sieve sizes tested, suggesting that the amount of fines on the surface of the particles are insignificant and do not contribute to the measured extent of breakage.
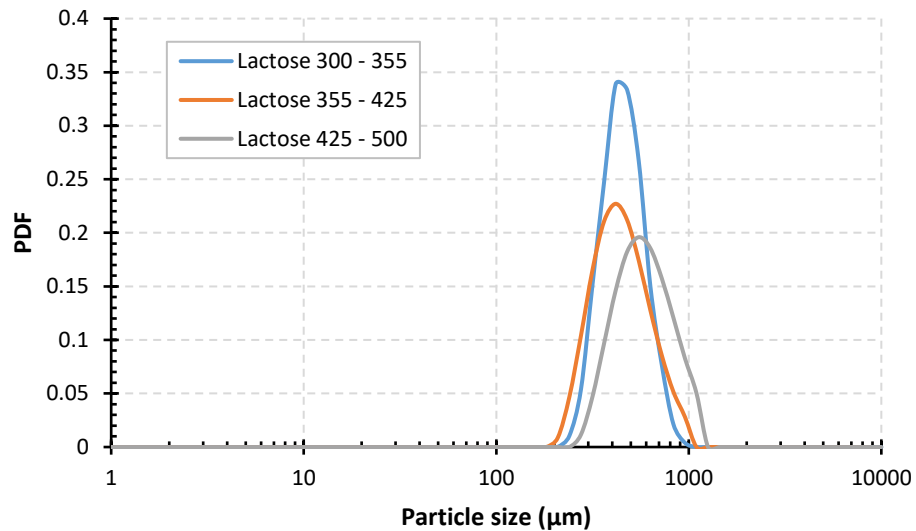
Figure 4.16: Probability density function of unwashed α-lactose monohydrate

4.5   Conclusions

Single particle impact testing has been carried out on aspirin, paracetamol and α-lactose monohydrate. All materials were impacted at velocities that resulted in breakage in the chipping regime. Table 4.3 shows the breakability indices of the tested materials. Paracetamol was found to break most readily, followed by aspirin and then α-lactose monohydrate. This same trend was seen with the results from previous work. The breakability indices observed in this work were found to be higher than those found from previous research. The higher value of breakage for paracetamol compared to the work of Bentham et al. (2004) may be owing to the fact that they impacted particles with a sieved size of 300 – 500 μm and separated the debris from the mother particles using one sieve size of 212 μm. The range of 300 – 500 μm can be divided into three British standard sieve sizes of 300 – 355 μm, 355 – 425 μm, and 425 – 500 μm. The debris from impact testing should then be separated using three corresponding sieve sizes of 212 μm, 250 μm, and 300 μm, respectively. By separating the range of 300 – 500 μm with a one sieve size of 212

μm, a lower extent of breakage would be measured. For aspirin, the breakability

index reported by Olusanmi et al. (2011) is based on the impact of only one particle

size, as this was the only size which was impacted at velocities under which semi-

brittle breakage occurs. The value reported in this work is based on three particle

sizes, and can therefore be considered more comprehensive and reliable.

Table 4.3: Breakability indices of the tested materials found in this investigation compared to previous literature

Material	$\alpha H/K_c^2$	$\alpha H/K_c^2$ from previous work
Paracetamol	0.0841	0.0539 (Bentham et al., 2004)
Aspirin	0.0534	0.0373 (Olusanmi et al., 2011)
α-lactose monohydrate	0.0179	0.0070 (Bentham et al., 2004) 0.0069 (Kwan et al., 2004)

The impact testing of paracetamol and aspirin found there to be a good unification

of the relationship between the extent of breakage and the materials physical

properties and impact conditions for all particle sizes tested. This indicates that

particle breakage varies linearly with particle size as predicted by the model.

However, α-lactose monohydrate does not show the same unification, with one

particle size found to have a greater extent of breakage. In Figure 4.17 the breakage

results achieved for unwashed α-lactose monohydrate in this investigation

compared to those from the work of Bentham et al. (2004) are shown. They

carried out the impact testing of particles sieved to the size range of 300 – 500 μm,

which were then washed with water and propan-2-ol. Their results are shown to

correlate with the breakage of sizes 300 – 355 μm and 355 – 425 μm. The

breakability index based on their results is 0.0070.
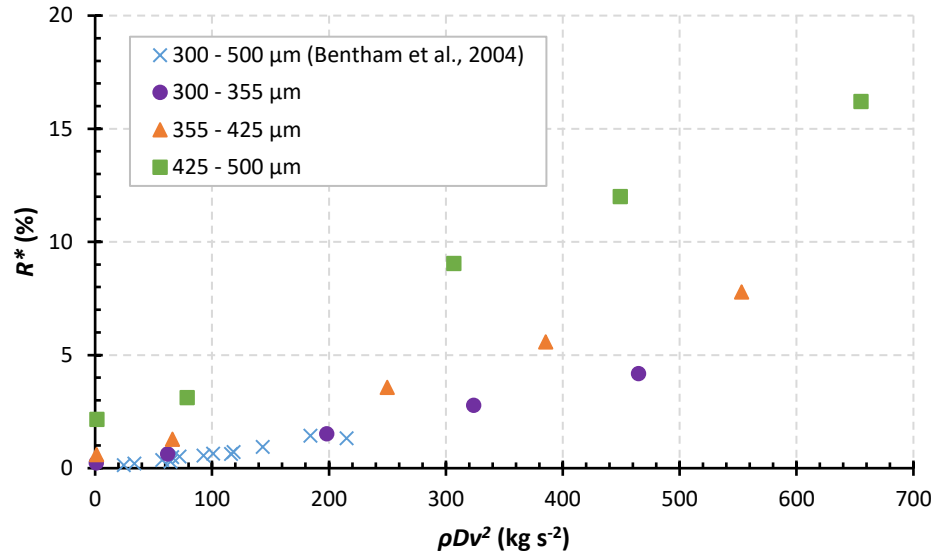
Figure 4.17: Extent of breakage results of unwashed α-lactose monohydrate as a function of ρDv^2 compared to previous research (Bentham et al., 2004)

The α-lactose monohydrate breakage results are compared to those of Kwan et al. (2004) in Figure 4.18. A similar correlation as with the results of Bentham et al. (2004) are seen. The breakability index from Kwan et al.'s results is 0.0069, which also compares to that found by Bentham et al.
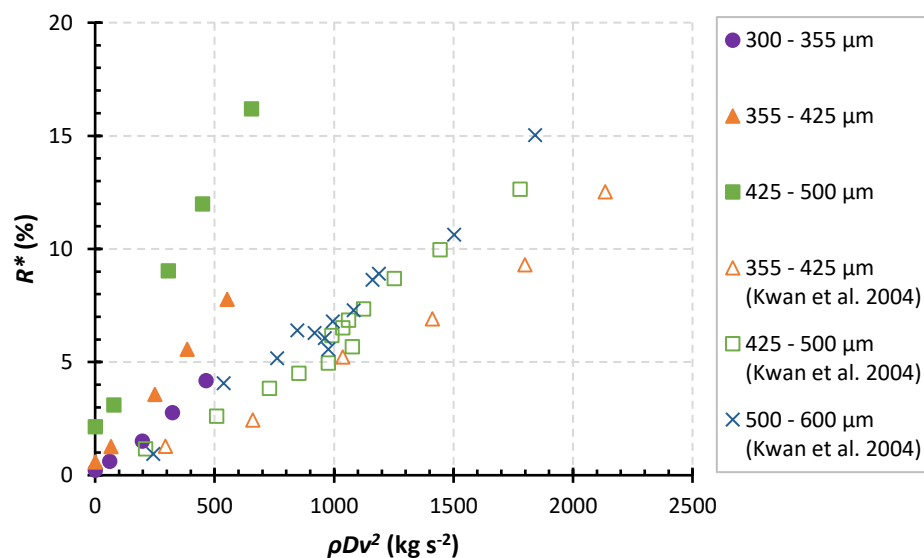
Figure 4.18: Extent of breakage results of unwashed α-lactose monohydrate as a function of ρDv^2 compared to previous research (Kwan et al., 2004)

Based on the results of Kwan et al. (2004), it can be seen that the minimum breakage velocity of α-lactose monohydrate is roughly proportional to D^{-2} (Figure 4.19).
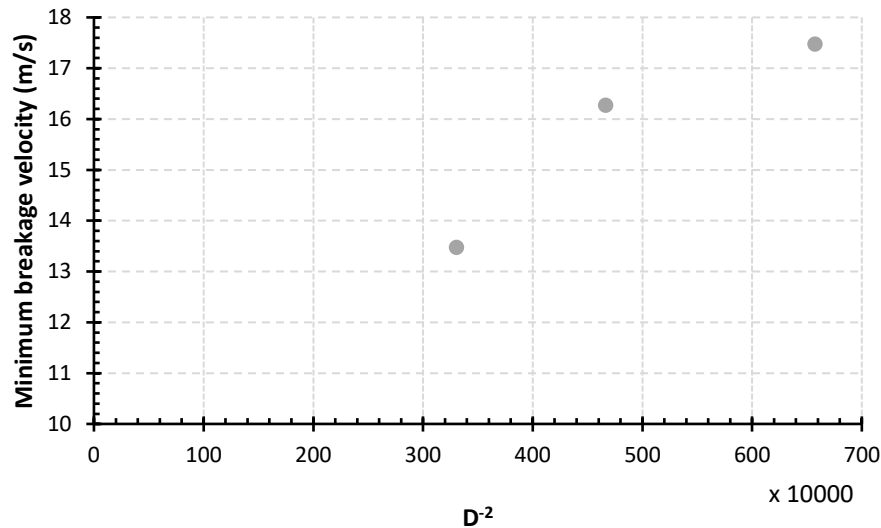
Figure 4.19: The minimum breakage velocity for α-lactose monohydrate as a function of D^{-2} based on the results of Kwan et al. (2004)

Further investigation is needed to determine the reason behind the increased breakability observed for α-lactose monohydrate compared to previous work. Possible causes could be the deterioration of the material by autoxidation, or environmental effects such as humidity.

The breakability index provides an indication of how readily materials break in relation to each other. Inferring the breakability index is a simple and cost efficient process, requiring as little as 2 g of material. A great benefit of the breakability index would be if it could be used to predict the breakage behaviour of a material in a larger, more intensive process such as spiral jet milling.

Chapter 5 Jet Milling of Active Pharmaceutical Ingredients and Excipients

5.1   Introduction

In the pharmaceutical industry, active pharmaceutical ingredients and excipients commonly used in drug formulations are produced by crystallisation. Controlling the growth of the material to produce a specific size, however, presents processing difficulties and therefore larger than desired size particles are the typical result of crystallisation.   The products of crystallisation are therefore passed on to a subsequent size reduction process to reach the required drug specifications.

Size reduction is achieved by the use of milling equipment, which employ compressive, impact or shearing forces to break material down from large to finer sizes. There are several mills used in the pharmaceutical industry, including the ball mill, hammer mill, and pin mill. When a sub-20 μm particle size is required, fluid-energy mills are the method of choice used in the pharmaceutical industry as they are capable of reducing particles to micron sizes, which are needed in order to compress the drug into appropriate sized tablets. They are able to mill material to narrow size distributions, which is a beneficial property when it comes to ensuring there is a good content uniformity in a dosage form. The mill also has no moving parts, and so there will be minimal wear of the equipment and the potential for contamination of the milled material is very low.

The spiral jet mill, shown schematically in Figure 5.1 is a commonly used type of fluid-energy mill. The mill comprises two pressurised air inlets: a particle injection

inlet (k) and a grinding gas inlet (c). Feed material enters the mill through the feed

chute (i) and falls into the Venturi injector system of the mill (b). The air pressure

in particle injection inlet accelerates feed material into the grinding chamber of

the mill (a), where size reduction takes place. The grinding gas passes through the

air supply ring (d) and then enters the grinding chamber through nozzles (f),

causing a circulating motion of the particles around the chamber. As the material

circulates, they encounter particle-particle and particle-wall interactions which

lead to breakage of the particles. Classification of the milled material is achieved

by the opposing effects of centrifugal (F_C) and drag (F_D) forces:

$$\boldsymbol{F}_C = \frac{\pi}{6} d_p^3 \rho_p \frac{v_t^2}{r} \tag{5.1}$$

where d_p is the particle diameter, $\boldsymbol{v}_t$ is the tangential velocity, and r is the radial

position of the particle,

$$\boldsymbol{F}_D = \frac{\pi}{8} C_D \rho_F \boldsymbol{v}_r^2 d_p^2 \tag{5.2}$$

where C_D is the drag coefficient, and $\boldsymbol{v}_r$ is the radial gas velocity. When the particle

is above a given size, known as the cut-off size, the centrifugal force acting on the

particle is greater than the drag force. This causes the particle to be pushed

towards the outer wall where it experiences extensive particle-particle and particle-

wall collisions. When the size of the particle reduces to below the cut-off size, the

drag force has a greater effect than the centrifugal force. The particle will then be

pulled towards the central outlet of the mill and will escape the chamber.
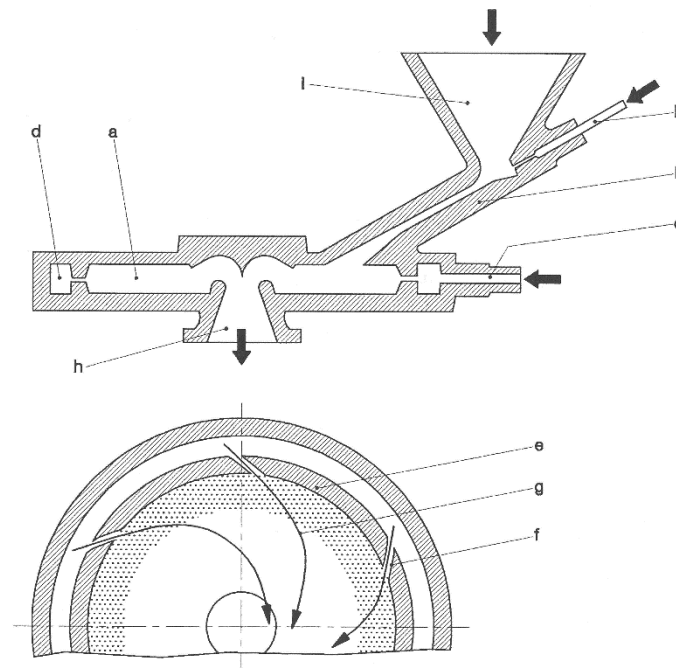
Figure 5.1: Principle of jet mill operation, where a) – grinding chamber, b) – venture injector, c) – grinding air supply, d) - air supply ring, e) – chamber wall, f) – grinding nozzle, g) – flow spirals, h) – central outlet, i) – feed chute, k) – injector nozzle (Hosokawa Alpine AG, 2004)

Another type of fluid energy mill commonly used is an opposed jet mill, depicted in Figure 5.2. In this mill particles are fed into a grinding chamber and then accelerated into each other by grinding nozzles on opposite sides. The ground material is then carried upwards with the gas into a classifier, where coarse particles are recycled back into the grinding chamber and finer particles of the desired size are passed through. Opposed jet mills have a lower energy requirement and can mill to a finer product size than spiral jet mills (Bernotat and Schönert, 2006). However spiral jet mills have a low maintenance cost and are easy to clean making them still very popular. Spiral jet mills can also be modified with a classifier to improve the degree of size reduction through controlled classification.
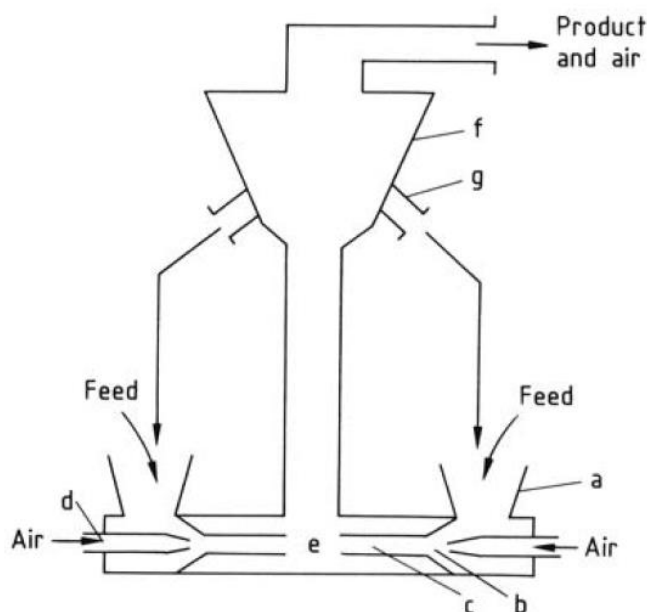
Figure 5.2: Schematic diagram of an opposed jet mill, where a = feed funnel, b = injector, c = acceleration pipe, d = propellant inlet, e = grinding chamber, f = classifier, g = outlet for recycling coarse fraction (Bernotat and Schönert, 2006)

In this chapter, the Hosokawa Alpine Aeroplex Spiral Jet Mill 50AS is used to mill the three pharmaceutical materials which were previously analysed by impact testing (i.e. paracetamol, aspirin, and α-lactose monohydrate) at a range of grinding conditions. The particle size distribution is measured by laser diffraction analysis using the Malvern Mastersizer 2000S from which the specific surface area of the milled products is calculated, and the relative change in the specific surface area of the materials is correlated with the breakability indices measured in Chapter 4.

5.2 Review of Spiral Jet Milling

Ramanujam and Venkateswarlu (1969) provided the first look into the effects of physical particle properties and grinding conditions on the milling behaviour of a 20 mm diameter spiral jet mill, using calcite as a test material. The solid feed rate (varied from 20 – 100 g/min) and grinding pressure (varied from 3 – 6 barg) were

found to be the two most influential parameters for particle size reduction. Particle size displayed a direct relationship with solid feed rate, with the lowest feed rate of 20 g/min at a grinding pressure of 4 barg leading to an 81.4 % reduction in d_{90} size from the feed, which was 0.88 mm. Interestingly, analysis of their results found there to be a power law relationship between d_{90} and the solid feed rate, while a more linear relationship was seen with d_{50}. Grinding pressure showed a positive correlation with particle size, with the d_{90} falling from 0.27 mm at 3 barg to 0.086 mm at 6 barg at a solid feed rate of 50 g/min. A power law relationship was also seen between d_{90} and the grinding pressure, however they did not show enough data to determine whether the same relationship existed with d_{50}. Further studies have found the same trend with different materials: Tuunila and Nyström (1998) used limestone and different types of gypsum (calcium sulphate dihydrate) fed at a rate of 1.2 – 6 g/min in a 100 mm mill and found a linear relationship between the d_{50} and both the solid feed rate and grinding pressure, although they carried out a limited number of experiments; Katz and Kalman (2007) tested sodium chloride in a 200 mm mill at solid feed rates of 17 – 417 g/min and found an inverse power law relationship between the percentage of particles under the feed size and the solid feed rate, and a linear relationship with the grinding pressure (though they showed a limited amount of results); Palaniandy and Azizli (2009) used talc (hydrated magnesium silicate) in a 100 mm fluidised jet mill; Vatsaraj et al. (2003) carried out experiments using lactose and sucrose. Sikong et al. (2008) suggest the d_{50} value of milled material is related to the grinding pressure by a power law equation:

$$d_{50} = aP^b \qquad\qquad\qquad (5.3)$$

where P is the pressure, and a and b are constants which were found to be related

to the feed particle size. They used grinding pressures and solid feed rates ranging

from 200 – 700 kPa (2 – 7 bar) and 12 – 120 g/min, respectively. They carried out

their investigations using materials undergoing size reduction in the brittle failure

mode, namely gypsum, barite, ilemenite, ferrosilicon and quartz. However they

did not use a common spiral jet mill, but rather an oval-shaped pneumatic

conveyor style jet mill. Despite the injector pressure contributing to the overall

fluid power input to the mill, various researchers have shown that the effect of

injector pressure on size reduction is actually negligible (Katz and Kalman, 2007;

Ramanujam and Venkateswarlu, 1969; Saleem and Smyth, 2010; Tuunila and

Nyström, 1998; Vatsaraj et al., 2003). Katz and Kalman (2007) highlighted that

the injector pressure only plays a significant role when the grinding pressure is

considerably low. The position of the grinding nozzles was shown to have some

effect on the degree of size reduction by Nair and Ramanujam (1992), who found

that there exists an optimum nozzle configuration. It should be noted, however,

that they used an oval-shaped pneumatic conveyor style mill rather than a

common circular spiral jet mill. The angle of the nozzles with the tangent at the

wall has been shown to have some effect on the size reduction, although it is not

significant. Tuunila and Nyström (1998) investigated nozzle angles of 23 – 43°,

while Katz and Kalman (2007) assessed angles of 45 – 70°. Product particle size

was found to decrease as the nozzle angle increased from 23° to 43°, and increasing

from 45° up to 70° led to a decrease in the product particle size. This suggests there is an optimum nozzle angle in the region of 43 – 45°.

While it is known that the mechanical properties of a material affect its milling behaviour, there has been little to no in-depth study of the relationship between mechanical properties and milling behaviour in a spiral jet mill. de Vegt et al. (2005a, 2005b) have investigated this relationship by first developing a rate of breakage (selection) function using dimensional analysis which incorporates the material mechanical properties of hardness and fracture toughness, and then carrying out experimental milling in a fluidised bed opposed jet mill for validation. They were able to show that the rate of breakage is influenced by the material mechanical properties, however there is no clear discernible trend. It should be noted that the mechanical properties used in their investigation were found from a combination of the bulk compression of materials and Heckel analysis (for yield strength) (Heckel, 1961), the solubility parameter (for fracture toughness) (Hancock et al., 1997) and inference from equations which relate hardness to yield strength (Marsh, 1964). Compression is not relevant to jet milling as particles reduce in size due to impacts between particles and with the wall which have a shorter contact time compared to compression, and thus may have different failure modes. Zügner et al. (2006) have also done so, looking at the relation of material hardness and Young's modulus to the milling behaviour of four materials: calcite, sodium ascorbate, α-lactose monohydrate, and sodium chloride. Calcite, the hardest material, was found to break to the coarsest particle size with the widest product size distribution at a given grinding condition. The hardest particle

should produce the finest platelets from breakage (Ghadiri and Zhang, 2002), which was not the case. There may therefore be other factors influencing the breakage beyond the mechanical properties. Sikong et al. (2008) also observed there was no straightforward relationship between mechanical properties and milling behaviour, acknowledging that the presence of cleavage planes has an influence. de Vegt et al. (2009) went deeper into the analysis of mechanical properties by investigating the effect of pre-existing flaws in sodium chloride from different sources. Using a fluidised bed opposed jet mill, they found that materials with a relatively low hardness have a higher rate of breakage compared to those with a higher hardness. They concluded that the higher rate of breakage is a result of a greater flaw density within the particle. However, flaw density is unrelated to the hardness of a material.

Other parameters have been investigated. Tuunila and Nyström (1998) found the height of the central outlet in the grinding chamber to have a linear, albeit insignificant relationship with the median particle size of milled material. The height of the grinding chamber was also found to have an insignificant effect on particle size by Katz and Kalman (2007). They, as well as Djokić et al. (2014a) also investigated the diameter of the grinding nozzle, whose influence was due to its effect on the input energy. Djokić et al. (2014a) also investigated the effect of the distance between the injector nozzle and the grinding chamber, which has a low influence on milling performance.

Müller et al. (1996) investigated the hold up and residence time of material in the spiral jet mill. By using radioactive tracers, they found that increasing the gas

pressure in the spiral jet mill reduces the residence time of the material. The hold up in the grinding chamber was also found to decrease with an increase in gas pressure, and was notably found to become independent of other influencing parameters such as material feed rate beyond a certain milling energy.

Physical modifications to the spiral jet mill have been made by some researchers in order to improve its performance. Kozawa et al. (2012) added a classifier (referred to as "particle-trap ring") to the exit of the classification zone to prevent large sized particles from escaping. They describe a shortcut flow of particles near the ceiling of the grinding chamber directly towards the central outlet due to them experiencing a smaller centrifugal force. Alfano et al. (1996) developed a prototype closed circuit spiral jet mill, which employed the recirculation of large sized material to reach a finer product size distribution.

Beyond the study of the effects of mill and material parameters on the milling performance of the spiral jet mill, the mill has been used in investigations of its effect on material properties and behaviour after milling. Hoyer et al. (2008) used the Hosokawa Alpine Aeroplex Spiral Jet Mill 50AS to produce stable, protein-loaded, thiolated microparticles with controlled drug release characteristics, showing potential for its use in large scale production. Matinde and Hino (2011) compared the effects of jet milling and mechanical crushing of high phosphorus iron ore on dephosphorisation behaviour. Jet milling was found to produce a lower iron yield than mechanical crushing, but had a much higher removal of gangue from the iron ore. Palaniandy and Azizli (2009) used a fluidised bed opposed jet mill to study the effects of jet milling on the mechanochemical effects of talc. The

term "mechanochemical effect" refers to mechanically initiated physicochemical effects in solid particles. They found that phase transformations took place, with the degree of crystallinity of talc decreasing as the extent of size reduction increased. Boudriche et al. (2014) compared the dry milling behaviour of three different mill types on attapulgite clay: the jet mill, the ball mill, and the vibration mill. The jet mill was found to have a lesser effect on the surface energy of the clay characterised by inverse gas chromatography than the other two milling methods. Not all materials undergo phase transformation. For example, limestone, fly ash and portland cement were found to undergo only physical size changes during milling, but no chemical changes (Sun et al., 2013). The same was seen with amiloride HCl (Djokić et al., 2014b). Muehlenfeld et al. (2013) carried out the co-grinding of griseofulvin and mannitol in the Hosokawa Alpine Aeroplex Spiral Jet Mill 50AS to improve the drug dissolution rate. Co-grinding was found to produce a drug mixture with a greater drug release rate than if the components had been pre-ground and then mixed together. The co-grinding process produced higher energy, metastable states of the components. Sun et al. (2013) also found co-grinding to be more effective than grinding separately. The capabilities of the spiral jet mill in regards to the milling of soft materials was investigated by Saleem and Smyth (2010). They used the Aljet mill with Pluronic® F-68, an alkylene copolymer. They found that the mill was not able to reduce the material to the desired particle size of 5 µm for pulmonary delivery, and that cryogenic ball milling was a more suitable method.

5.2.1 Summary

The effect of the grinding conditions of the jet mill has been extensively researched, and there is a generally accepted significant relation of the grinding pressure and material feed rate to the milling performance. The milled product size is inversely proportional to the grinding pressure, and directly proportional to the solid feed rate. While their effect has been found to be universal for all types of jet mill, only a few pieces of research have analysed their effect in a traditional circular-shaped spiral jet mill (Katz and Kalman, 2007; Tuunila and Nyström, 1998). A wide range of grinding pressures have been investigated, while the solid feed rate has tended to be at a high level. Tuunila and Nyström (1998) were found to use the lowest solid feed rate, which ranged from 1.2 – 6 g/min.

The spiral jet mill has been found to be a capable size reduction apparatus for breaking both brittle and semi-brittle materials. However, no in-depth study of the relationship between the milling behaviour and the material mechanical properties has been found. Particularly there has been no attempt to relate the milling behaviour to single particle impact breakage based on a mechanistic breakage model for semi-brittle materials such as that of Ghadiri and Zhang (2002). While literature has been found of the spiral jet milling of many pharmaceutical materials, interestingly there is none detailing the spiral jet milling behaviour of aspirin and paracetamol.

5.3 Experimental Test Method for Spiral Jet Milling of Active Pharmaceutical Ingredients and Excipients

5.3.1 Hosokawa Alpine Aeroplex Spiral Jet Mill 50AS

All milling experiments described in this chapter were carried out using the Hosokawa Alpine Aeroplex Spiral Jet Mill 50AS (Hosokawa Micron Ltd, UK), shown in Figure 5.3.

Figure 5.3: Hosokawa Aeroplex Spiral Jet Mill 50AS

The mill is made from stainless steel (grade 316L) with surface roughness $R_a < 0.8$ µm. The grinding chamber of the mill used (Figure 5.4) has a diameter of 50 mm and depth of 4 mm, and consists of four grinding nozzles, each with a 0.8 mm diameter and an angle of 50° with respect to the normal to the wall. The injector nozzle has a diameter of 0.9 mm.
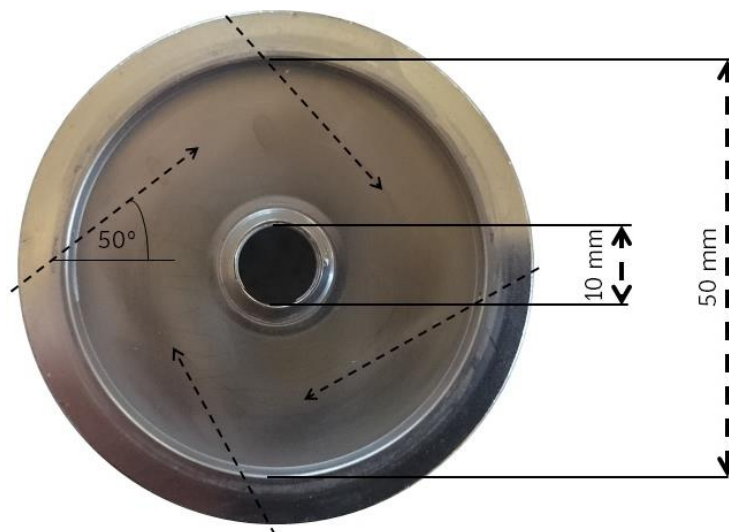
Figure 5.4: Grinding chamber used with the Hosokawa Alpine Aeroplex Spiral Jet Mill 50AS

Downstream of the mill is a GORE-TEX® filter bag which collects milled material but allows air to pass through and escape the system. The pneumatic unit of the mill was connected to a compressed air supply, which was capable of supplying air up to a gauge pressure of 600 kPa (6 barg).

5.3.2 Investigation of Steady-State Milling in the 50AS

α-lactose monohydrate was fed into the spiral jet mill at a feed rate of 5×10^{-5} kg/s (3 g/min) using the Retsch vibratory feeder DR 100. The mill was operated at two different pressure conditions: with a grinding and injector gauge pressure of 100 and 200 kPa (1.0 and 2.0 barg), respectively, and 200 and 400 kPa (2.0 and 4.0 barg), respectively. A timer was started when the first particle fell into the Venturi feed opening just above the injector nozzle. After a given amount of time had elapsed, both the injector and grinding pressure were abruptly cut off from the mill by closing the valve of the pneumatic unit, and the material feed was simultaneously stopped by turning off the vibratory feeder. The stopping times ranged from 5 to 180 s. The material present in the grinding chamber and the filter

bag were then collected and measured separately in the Malvern Mastersizer 2000S (wet dispersion), with enough material to achieve a laser obscuration of 5 – 10 %. Propan-2-ol was used as a dispersant.

5.3.3   Change in specific surface area of milled pharmaceutical material

Tests were carried out using paracetamol, aspirin and α-lactose monohydrate. 10 g of each material was fed into the mill using a vibratory feeder at a feed rate of approximately 5×10^{-5} kg/s (3 g/min). Table 5.1 shows the several grinding and injector pressure combinations tested, and the fluid power input of each. Fluid power input was calculated based on the specific work of expansion of the gas from the grinding and injector nozzles into the grinding chamber. This specific work is multiplied by the mass flow rate of air through the nozzles, which is calculated based on the assumption of adiabatic flow through a frictionless nozzle. The calculation of fluid power input is described in Chapter 7.

Table 5.1: Grinding and injector pressure combinations used in the 50AS

Pressure (barg)	Grinding	0.4	0.6	0.8	1.0	1.0	1.0	2.0	2.0	3.0	4.0	5.0
	Injector	0.4	0.6	0.8	2.0	3.0	4.0	3.0	4.0	4.0	5.0	6.0
	Fluid power input (mW)	0.2	0.3	0.4	0.7	0.8	0.9	1.2	1.3	1.7	2.2	2.8

After all the material had left the vibratory feeder, the mill was left to continue running for a further one minute. It was then stopped and left to rest for 10 minutes to allow any built up electrostatic charge to dissipate. An anti-static gun was also used to discharge the mill product. The milled material was then collected

from the filter bag. The Malvern Mastersizer 2000S (wet dispersion) was used to measure the product size distribution, from which the specific surface area of the milled materials was calculated. 2,2,4-trimethylpentane with 0.1 w/w % lecithin, 2,2,4-trimethylpentane, and propan-2-ol were used as dispersants for paracetamol, aspirin, and α-lactose monohydrate, respectively. The laser obscuration was between 5 – 10 %.

5.4 Results of Jet Milling of Active Pharmaceutical Ingredients and Excipients

5.4.1 Investigation of Steady-State Milling in the 50AS

Steady-state milling in the jet mill is signified by a constant value of SSA of the material present in the grinding chamber, and of the milled material collected in the filter bag, independent of milling time. The point at which steady-state is reached in the grinding chamber was found to depend on the grinding pressures used in the system. The SSA of the material present in the chamber fell until there was a balance between the feed rate of α-LM into the chamber and the α-LM chips and partially broken particles out of the chamber, and a constant SSA is reached. Figure 5.5 shows a constant SSA of approximately 0.2 m^2/g is reached in the grinding chamber after approximately 60 s when the grinding and injector gauge pressures are 100 and 200 kPa (1.0 and 2.0 barg), respectively. When the grinding and injector pressures are doubled to 200 and 400 kPa (2.0 and 4.0 barg), respectively, steady state is reached around 120 s, with an SSA in the grinding chamber of approximately 0.4 m^2/g. When the pressure is higher, α-LM breaks to a greater degree. This means that there will be a larger amount of chips produced, and thus a higher SSA.
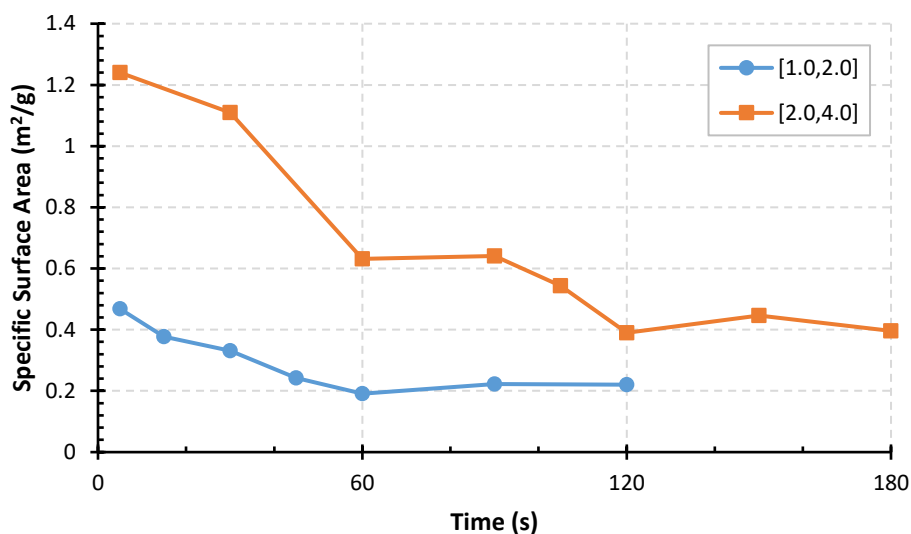
Figure 5.5: SSA of α-lactose monohydrate present in the grinding chamber at specific time intervals

When the grinding and injector pressures were low at 100 and 200 kPa (1.0 and 2.0 barg, respectively), there was an insignificant amount of material collected in the filter bag before 60 s, which in fact could not be detected (see Figure 5.6). After 60 s the milled material in the bag reached a constant SSA of approximately 2.0 m^2/g. At a higher grinding and injector pressure of 200 and 400 kPa (2.0 and 4.0 barg, respectively), the SSA of α-LM increases up to 30 s, and then decreases until 60 s, where it reaches a constant SSA value of approximately 2.8 m^2/g.
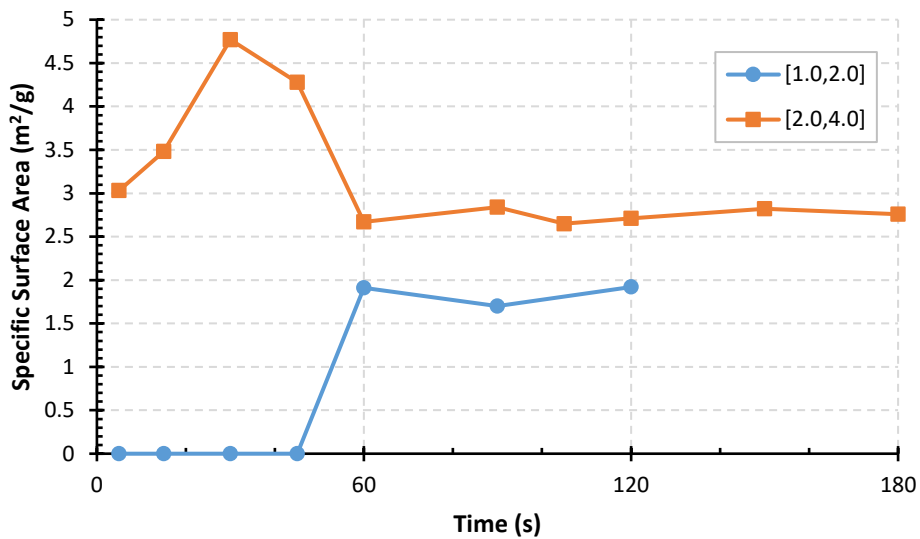
Figure 5.6: SSA of α-lactose monohydrate present in the filter bag at specific time intervals

These behaviours are an effect of the mechanical properties of α-LM. α-LM is difficult to mill, and at a low grinding pressure of 100 kPa (1.0 barg) it is not being broken down to a size which is capable of escaping from the grinding chamber due to drag force. As the milling process progresses, the grinding chamber continues to fill up with α-LM until the mass of material is sufficient enough that large sized particles can be classified and escape through the central outlet. As the grinding pressure is increased to 200 kPa (2 barg), the α-LM is broken to a higher degree and more fine material is produced that escapes the chamber due to drag forces. This is indicated by the increase in SSA up to 30 s. Beyond 30 s, the mass of large sized particles in the chamber is sufficient for them to be classified. The SSA of the material present in the filter bag in then reduced. After 60 s steady state operation is reached. Figures 5.7 and 5.8 show how the point of constant SSA in the grinding chamber and filter bag coincide for the two tested pressure conditions presented in Figures 5.5 and 5.6. At steady state with a grinding and injector pressure of 2.0

and 4.0 bar, respectively, it was noted that there was an average mass of 1.3 g of α-

lactose monohydrate present in the grinding chamber.
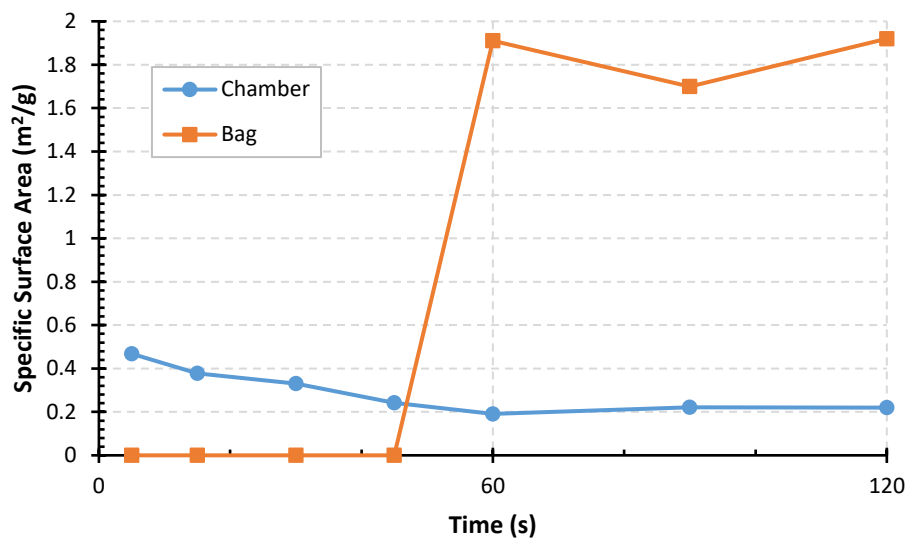
Figure 5.7: Comparison of SSA of α-lactose monohydrate in the grinding chamber and filter bag milled with grinding and injector gauge pressure of 100 and 200 kPa (1.0 and 2.0 barg), respectively
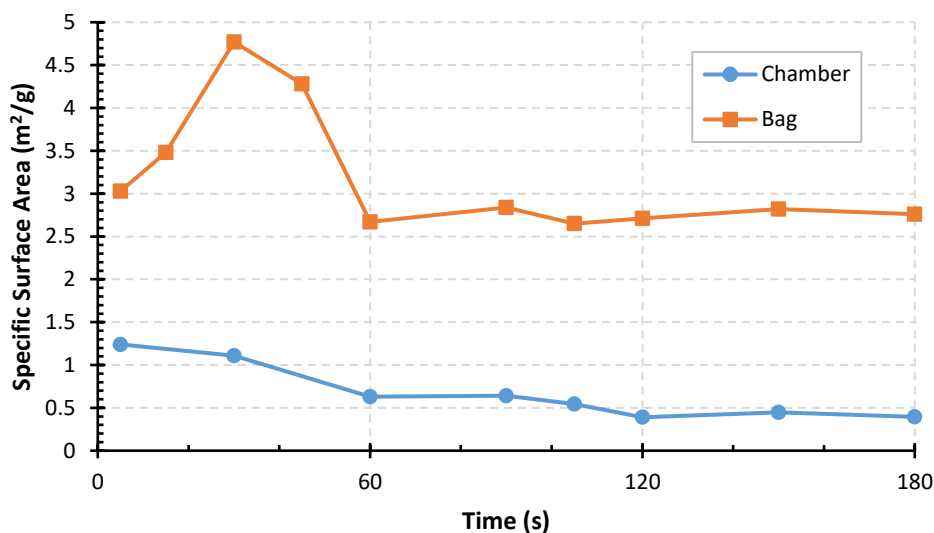
Figure 5.8: Comparison of SSA of α-lactose monohydrate in the grinding chamber and filter bag milled with grinding and injector gauge pressure of 200 and 400 kPa (2.0 and 4.0 barg), respectively

The point at which steady state is reached is a material dependent condition. Hard

to break materials will reach steady state at a later milling time than materials with

a higher breakability index. Spiral jet milling of aspirin and paracetamol will therefore reach steady state before 60 s.

5.4.2 Milling Behaviour of α-Lactose Monohydrate

The milling of α-lactose monohydrate was found to be tough, with large sized particles regularly being found in the grinding chamber as well as in the filter bag after milling was complete. The milled powder produced at low grinding pressures was found to flow well, with the powder easily pouring from the filter bag during collection. Powder milled at high pressures was found to clump together, and some light brushing was required to remove it from the bag. Figure 5.9 shows the product of milling α-lactose monohydrate at 100 kPa (1 barg) grinding gauge pressure collected from the filter bag. It consists of very small chippings of α-LM, as well as large fragments and virtually unbroken feed size particles.
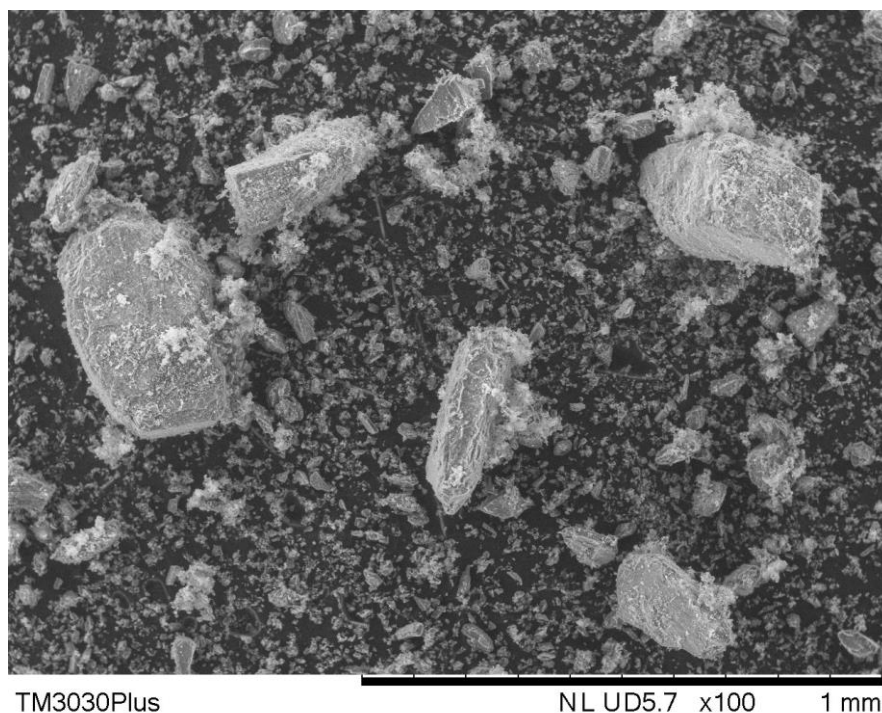
Figure 5.9: SEM image of α-lactose monohydrate 425 – 500 μm milled at 100 kPa (1 barg) grinding gauge pressure collected from the filter bag

When milled at a higher grinding gauge pressure of 300 kPa (3 barg), finer

fragments are produced and collected in the filter bag, which can be seen to clump

together in Figure 5.10. A large sized particle can also be seen, which is an

indication of how difficult it is to mill the material. The fine fragments, collected

from the filter bag, all appear to have polygonal shapes, as can be seen in Figure

5.11.
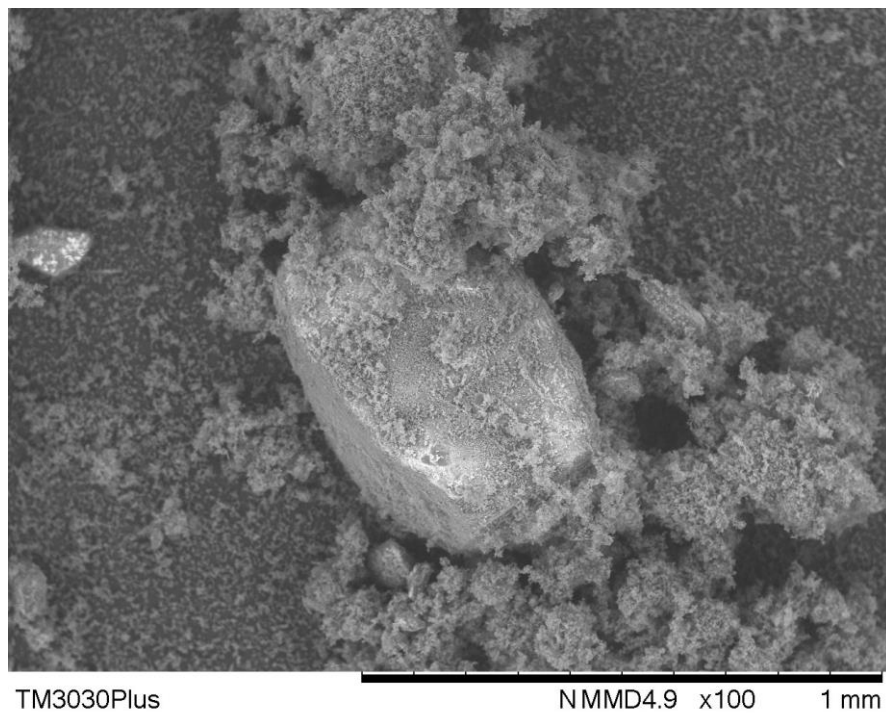
Figure 5.10: SEM of α-lactose monohydrate 425 – 500 µm milled at 300 kPa (3 barg) grinding gauge pressure
collected from the filter bag
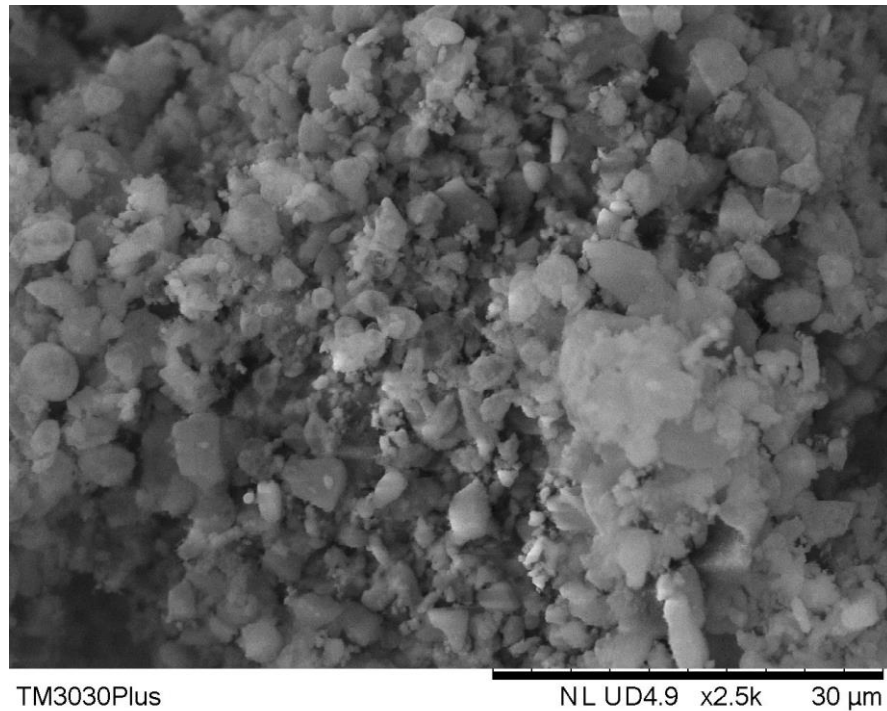
Figure 5.11: SEM image of fine debris of α-lactose monohydrate 425 – 500 μm milled at 300 kPa (3 barg) grinding gauge pressure collected from the filter bag

Analysis of the cumulative product size distribution of α-lactose monohydrate shows a change in the breakage mechanism (as previously described in Section 2.1 and Figure 2.4) as the grinding and injector pressures are increased. At a low grinding gauge pressure of 100 kPa (1 barg), α-lactose monohydrate appears to break via the chipping mechanism, with there being a large amount of fine particle below 200 μm as displayed in Figure 5.12. As the grinding gauge pressure increases up to 500 kPa (5 barg), the shape of the cumulative curves shift from chipping to fragmentation to disintegration.
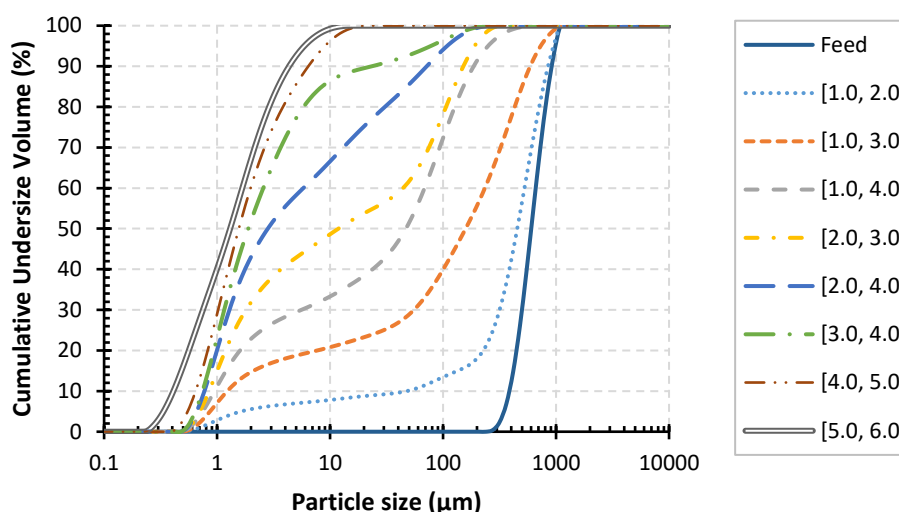
Figure 5.12: The cumulative product size distribution of α-lactose monohydrate 425-500 μm obtained by laser diffraction

5.4.3 Milling Behaviour of Aspirin

Aspirin was an easy material to break in the spiral jet mill at all milling conditions, reducing to the fine powder seen in Figure 5.13 even at 100 kPa (1 barg) grinding gauge pressure. The same degree of fineness was achieved with 300 kPa (3 barg) grinding gauge pressure, shown in Figure 5.14. Some material was found to remain in the grinding chamber when the grinding and injector gauge pressures were less than 100 and 200 kPa (1.0 and 2.0 barg), respectively. At all other conditions, the material exited the grinding chamber into the filter bag. The milled aspirin showed a great tendency to stick to the filter bag at all conditions listed in Table 5.1, and aggregated into lumps when collecting into a glass jar.
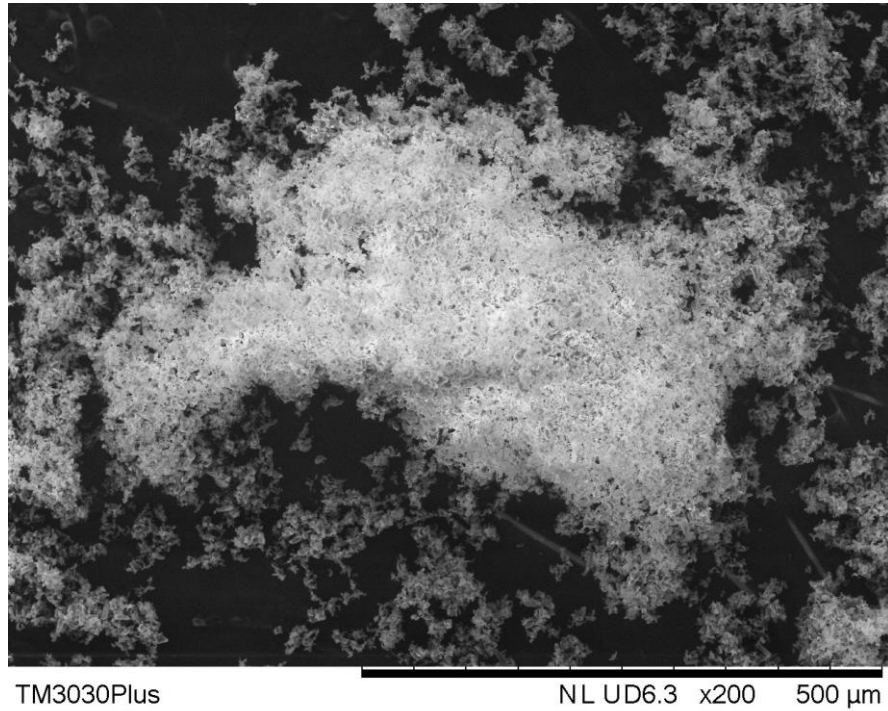
Figure 5.13: SEM image of aspirin 425 – 500 µm milled at 100 kPa (1 barg) grinding gauge pressure
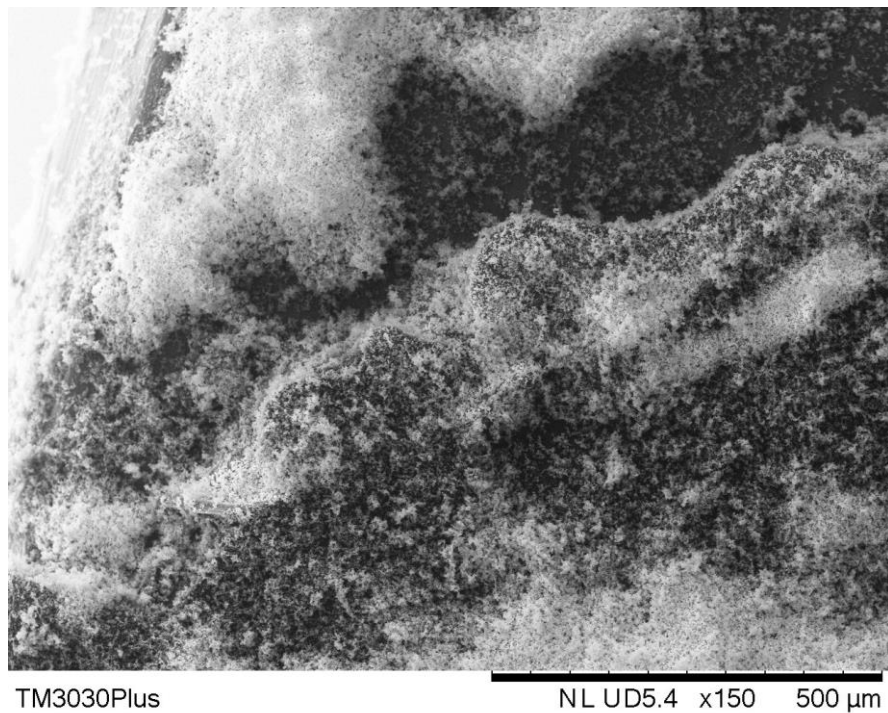
Figure 5.14: SEM image of aspirin 425 – 500 µm milled at 300 kPa (3 barg) grinding gauge pressure

Figure 5.15 shows that the aspirin milled into what can be described as short

needle/rectangle shapes, suggesting the existence of a cleavage plane, which

Olusanmi et al. (2011) describe as being on the (001) plane.

TM3030Plus   NL UD5.4   x2.0k   30 μm
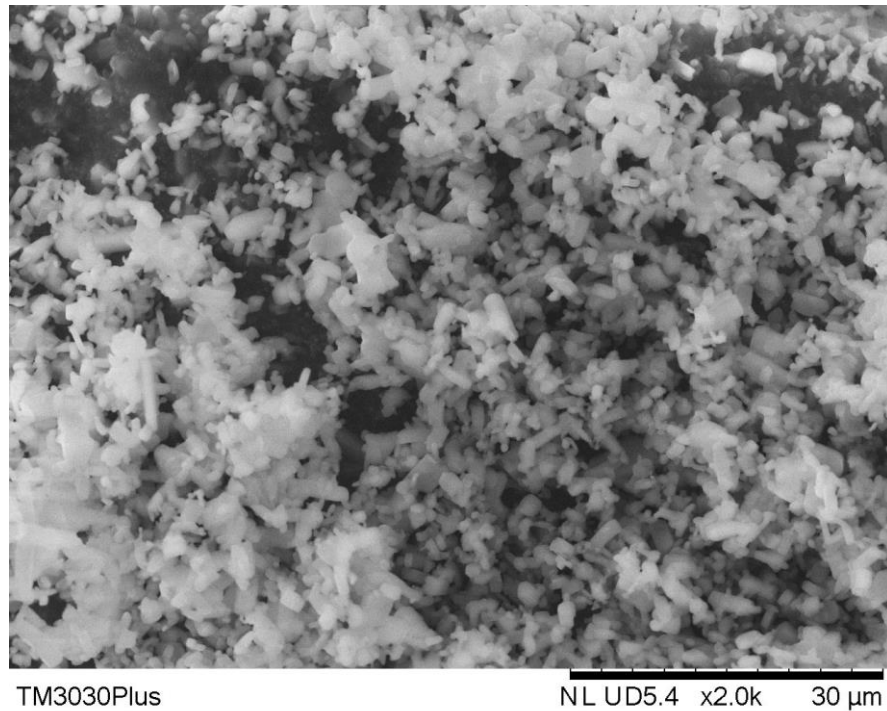
Figure 5.15: SEM image of fine debris of aspirin 425 – 500 μm milled at 3 barg grinding pressure

By comparison, aspirin breaks more readily than α-lactose monohydrate at the

same grinding conditions. Figure 5.16 shows that aspirin breaks by disintegration

to comparable size distributions at grinding gauge pressures of 100 kPa (1 barg) or

greater. From 40 – 80 kPa (0.4 – 0.8 barg), the product size distribution curve

demonstrates breakage within the chipping regime.
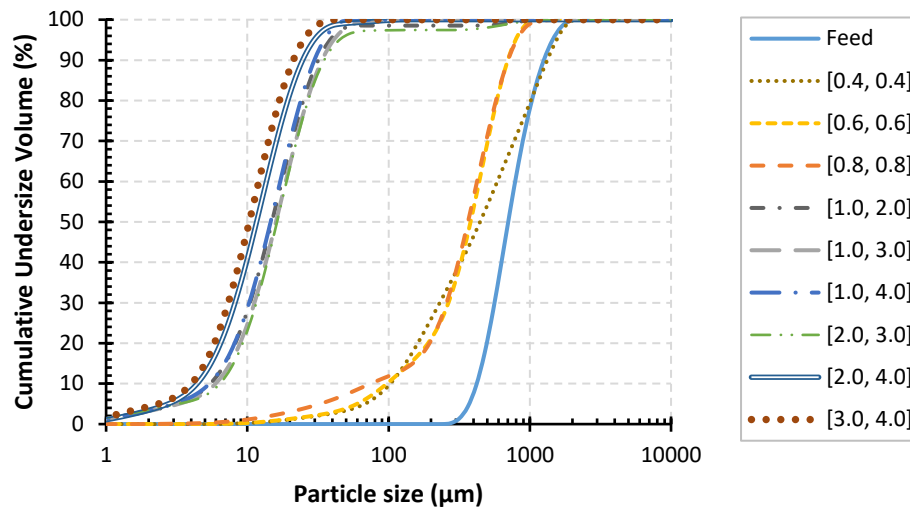
Figure 5.16: The cumulative product size distribution of aspirin 425-500 μm obtained by laser diffraction

5.4.4   Milling Behaviour of Paracetamol

Paracetamol milled similarly to aspirin, with the material milling to fine powder at all conditions. It was also found to stick to the filter bag and aggregate during collection, to a greater extent than aspirin. Figure 5.17 shows that paracetamol mills into needle shapes, suggesting there exists cleavage planes.
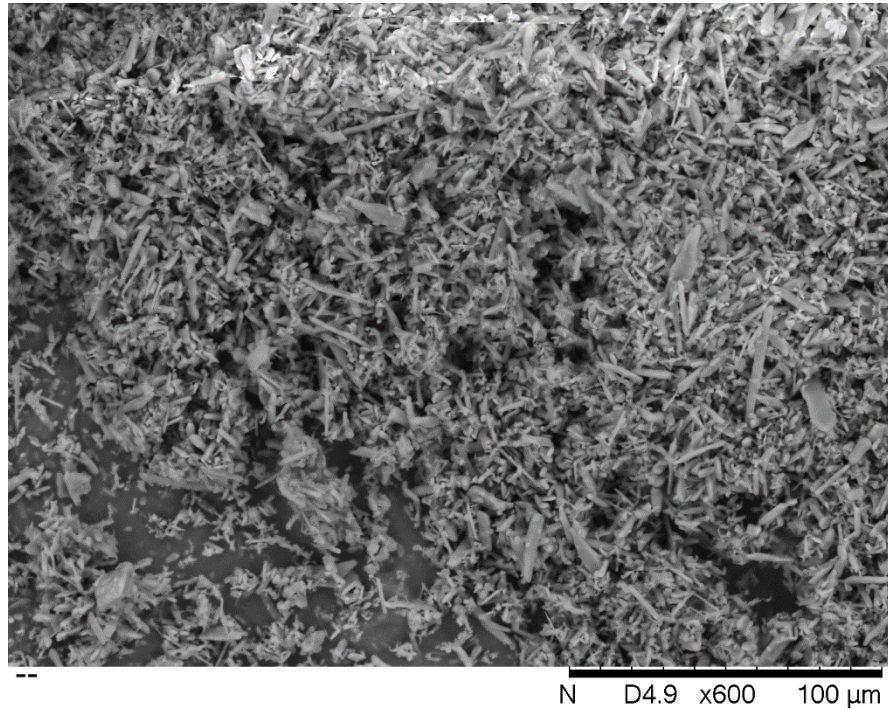
Figure 5.17: SEM image of paracetamol 425 – 500 μm milled at 300 kPa (3 barg) grinding gauge pressure

Paracetamol was found to break even easier than aspirin. The cumulative product size distribution in Figure 5.18 shows that no breakage in the chipping regime took place at any of the grinding conditions tested, but rather one case of fragmentation and the rest disintegration. The size distributions are also close to repeatable at grinding and injector gauge pressures of at least 60 kPa (0.6 barg) each.
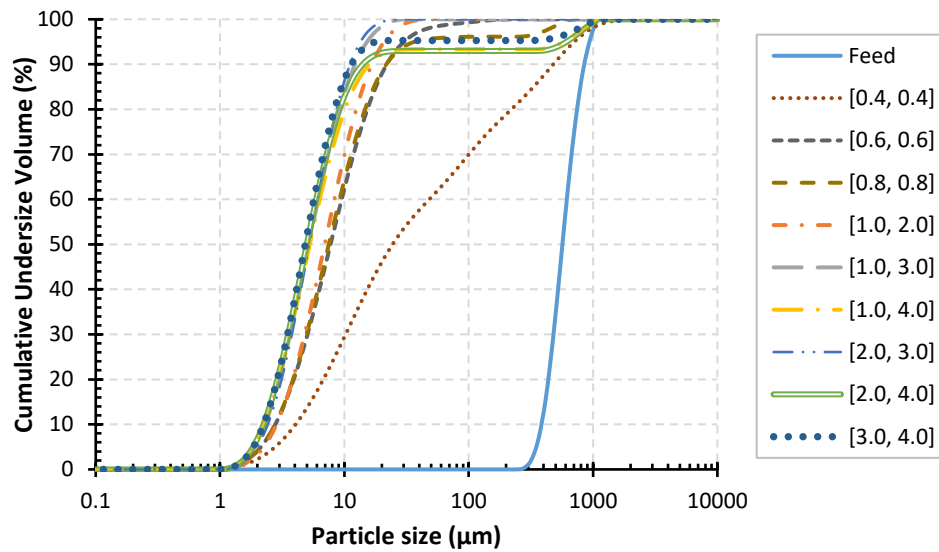
Figure 5.18: The cumulative product size distribution of paracetamol 425-500 μm obtained by laser diffraction

5.4.5   Correlation of the Change in Specific Surface Area to the Breakability Index of Materials

The breakability index gives an indication of how readily different semi-brittle materials break via chipping in relation to each other. When comparing two materials, that with the higher value of $\alpha H/K_c^2$ would break more readily. In theory, the material that breaks more should show a greater change in specific surface area from the feed material given that they break under the same mechanism.

Figure 5.19 illustrates the ease of milling of each material when comparing the $\Delta SSA/SSA_f$ (the ratio of the change in specific surface area of a milled material to the specific surface area of the feed material) of a given material at different grinding conditions. Aspirin and paracetamol have relatively the same $\Delta SSA/SSA_f$ for each feed particle size when the fluid power input/feed rate ratio is greater than

0.01 J/g. This suggests that the two materials have reached their grinding limit at this point. Below 0.01 J/g, paracetamol shows a steady increase in $\Delta SSA/SSA_f$ while aspirin displays a sharper change from virtually no change in specific surface area to its grinding limit. The contrary is seen with α-lactose monohydrate, which has an increasing $\Delta SSA/SSA_f$ with fluid power input for each feed particle size. The $\Delta SSA/SSA_f$ continues to increase up to the highest achievable fluid power input conditions. α-lactose monohydrate is therefore harder to mill and has not yet reached its limiting grinding size. This behaviour is further illustrated in Figure 5.20, which shows the d_{90} values for the milled materials as a function of the ratio of fluid power input to material feed rate. The d_{90} values for aspirin and paracetamol can be seen to reach a constant and become independent of the fluid power input to feed rate ratio, while the d_{90} for α-lactose monohydrate continues to decrease as the fluid power input to feed rate ratio increases.
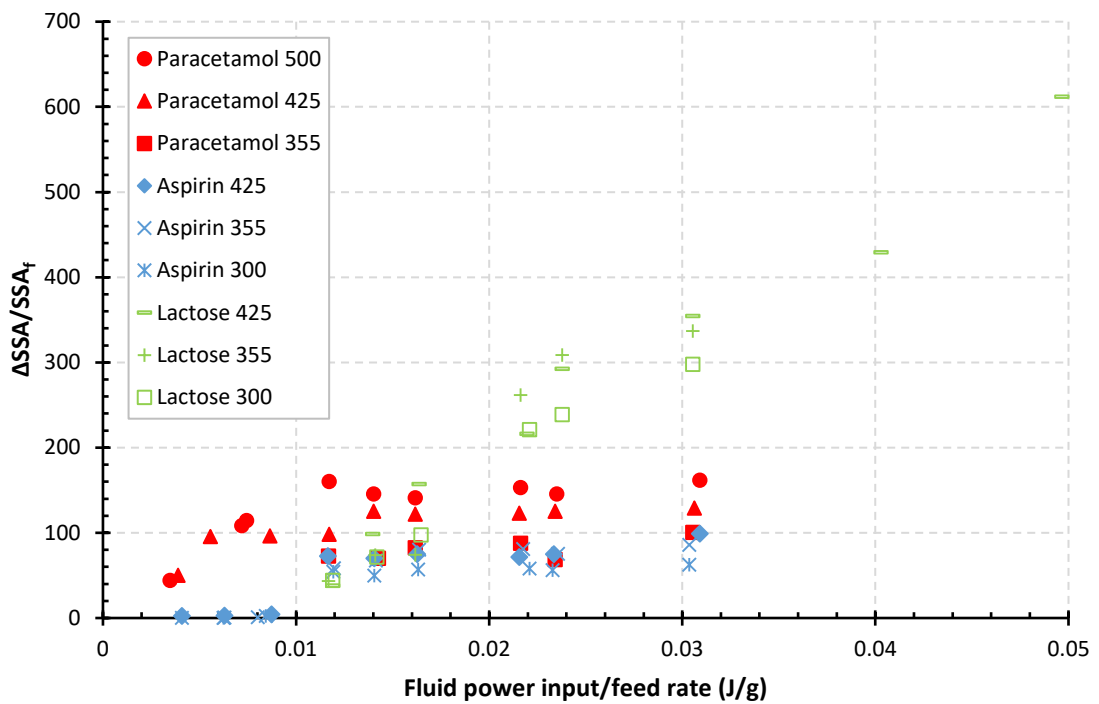
Figure 5.19: The $\Delta SSA/SSA_f$ as a function of the fluid power input/feed rate for paracetamol, aspirin and α-lactose monohydrate for the spiral jet mill
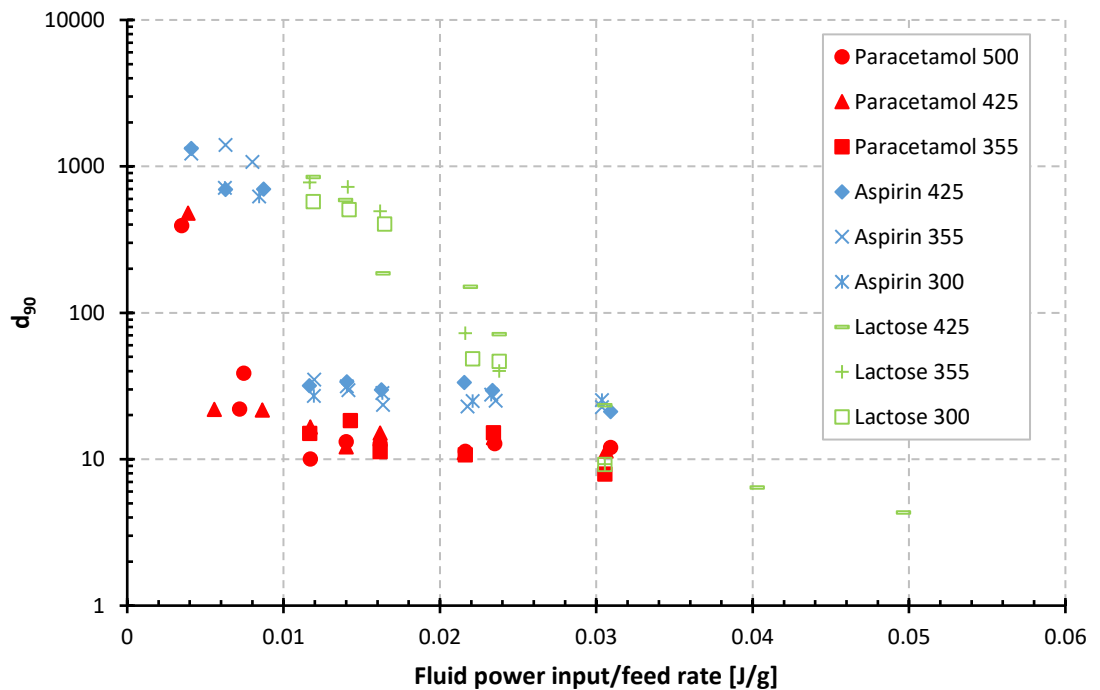
Figure 5.20: The d_{90} as a function of the fluid power input/feed rate for paracetamol, aspirin and α-lactose monohydrate for the spiral jet mill

ΔSSA/SSA$_f$ generally decreases as the particle size is decreased for each material (see the results for paracetamol in Figure 5.19), indicating that larger particles break more than smaller particles at a given fluid power. This is due to larger particle sizes having a greater amount of inertia, causing them to impact at a greater force. They will therefore undergo a larger amount of deformation and have a greater extent of breakage. This follows the model of Ghadiri and Zhang (2002) which shows that the fractional material loss per impact is proportional to the particle size.

Spiral jet milling shows interesting behaviour of the milled pharmaceutical materials in regards to their relative specific surface areas. Figure 5.19 shows that there is a greater ΔSSA as a result of spiral jet milling at high grinding pressures for α-lactose monohydrate compared to aspirin and paracetamol. This is contrary to what is expected, as it is more commonly assumed that the material with the greater propensity for breakage would break to a greater degree, and therefore have the higher value of ΔSSA. In this case, the material with the lowest breakability index actually has the highest ΔSSA for the same fluid power input. Comparison of the ΔSSA of aspirin and paracetamol falls in line with that expected from their $\alpha H/K_c^2$ values, with paracetamol having a higher ΔSSA than aspirin.

To ensure that this behaviour was not unique to laser diffraction measurements, BET surface area analysis was used as an alternative measure of the SSA. The Micromeritics TriStar 3000 was used to measure the specific surface area of the milled product of the feed sieve size 425 – 500 μm of each material, milled with a grinding and injector pressures of 300 and 400 kPa (3 and 4 barg), respectively.

The same trend in specific surface area of the three materials was seen, as shown

in Table 5.2.

Table 5.2: Specific surface area of milled materials at maximum fluid power input from feed sieve size 425 - 500 μm, from BET surface area analysis (BET) and laser diffraction (LD)

Material	$\alpha H/K_c^2$	Surface Area (m²/g)	
		BET	LD
α-lactose monohydrate	0.0179	2.72	2.47
Paracetamol	0.0841	1.37	1.11
Aspirin	0.0534	1.18	0.65

This behaviour may be due to the hardness of the materials. From indentation

fracture mechanics it is known that there is an inverse relationship between the

hardness of a material and the depth from the material free surface at which lateral

cracks are formed. Hard materials will therefore produce finer fragments when

broken via chipping as compared to softer materials. α-LM has a greater hardness

than paracetamol and aspirin, and thus breaks to produce finer chips and a greater

increase in specific surface area.

The existence of cleavage planes also means that materials will tend to break into

regular shapes. Where no cleavage planes exist, the breakage of the material will

be due to tensile stresses experienced by the particles. These particles will produce

polygonal-shaped chips. The specific surface area will therefore be higher than the

needle shapes produced by the presence of cleavage planes.

5.5   Conclusions

The pharmaceutical materials of paracetamol, aspirin and α-lactose monohydrate

were milled in a spiral jet mill and exhibited differing milling behaviour while

grinding conditions were kept constant, indicating that the materials mechanical properties have an effect.

Paracetamol and aspirin were found to break easily. Analysis of their product size distributions shows that both materials exhibit a transition from chipping to disintegration from very low milling pressures. SEM images of the materials show they break into needle-shaped particles, indicating the existence of cleavage planes. Compared to one another, paracetamol was found to produce the higher increase in specific surface area; a trend which falls in line with what is expected based on the results of the single particle impact testing detailed in Chapter 4.

α-lactose monohydrate showed a steady transition from chipping to fragmentation to disintegration in the product size distribution as the grinding pressure increased, indicating the difficulty of inducing breakage. It was found to produce polygonal shaped particles. The increase in specific surface area compared to paracetamol and aspirin, however, was found not to correlate with the findings of single particle impact testing, with the ΔSSA being higher than the other materials. This is attributed to thinner chips being produced due to high hardness of α-lactose monohydrate.

One of the limitations of the Hosokawa Alpine Aeroplex Spiral Jet Mill 50AS is the inability to see the milling process inside the grinding chamber, or to measure the impact velocities being experienced by the particles. This would allow for a better analysis of the breakage behaviour and its relationship with breakability index. Simulations could be used to provide an insight into the particle collision

behaviour and energy utilisation, and thus the breakage behaviour in the grinding

chamber.

Chapter 6 Simulation of a Spiral Jet Mill

6.1 Introduction

As mentioned previously, the spiral jet mill is a prevalent size reduction equipment in the pharmaceutical industry. This is the case despite the fact that the size reduction mechanism of the mill is not very well understood. The desired product size distribution is typically achieved through the trial and error of different injector and grinding nozzle gas pressures and solid feed rates. This can be an expensive process due to the potential to produce product that does not meet the required specifications. In order to improve the cost effectiveness of the spiral jet milling process, an attempt is being made in this work to use computer simulations to predict the macroscopic behaviour in the mill, and thus the milling performance.

In this chapter, Computational Fluid Dynamics (CFD) on its own and also CFD two-way coupled with the Discrete Element Method (DEM) are used to simulate the spiral jet mill. The grinding chamber of the Hosokawa Alpine Aeroplex Spiral Jet Mill 50AS is drawn using CAD and used as the simulating geometry. Using CFD, the ground particle size classification efficiency of the mill is analysed. Using DEM-CFD, the particle motion in the grinding chamber is simulated and the fluid-particle-wall energy transfer is investigated. The effects of the number of particles in the chamber and the grinding gas pressure on particle behaviour and the normal and shear stress of the particles are studied.

6.2   Review of Numerical Simulations Involving the Spiral Jet Mill

There have been few investigations of the spiral jet mill using simulations. Eskin et al. (1999) carried out one of the earliest work where they calculated the flow of gas through a jet nozzle operating with high suspended particle concentrations. While they did not directly investigate a typical jet mill geometry, their work involved the acceleration of particles by jets, which is a fundamental behaviour of a modern spiral jet mill. This was the foundation for further research into the efficiency of particle acceleration in different types of jet milling systems. It led to Eskin and Voropayev (2001) showing that the efficiency of particle acceleration decreases as the size of the feed particles increases. Eskin and Kalman (2002) developed a model to estimate the friction between particles and the wall of a jet mill nozzle.

Gommeren et al. (2000) simulated a closed loop spiral jet mill using the Direct Simulation Monte Carlo (DSMC) method in two dimensions. They provided very limited simulation results, showing how hold-up varies with time. They incorporated breakage into their simulations by creating a bond between two polygon elements, which broke upon experiencing a specified tensile stress. Han et al. (2002) produced the first work that simulated comminution in the spiral jet mill using combined DEM-CFD. Using the standard k-ε turbulence model, they conducted 2D simulations that incorporated the Ghadiri and Zhang breakage model (Ghadiri and Zhang, 2002). The mill simulated was that used by Tuunila and Nyström (1998). They showed the gas velocity vector direction in the grinding chamber, and found the fluid moves from the outer walls to the central outlet, with the velocity increasing as the radial distance from the centre decreases. The feed

particles were found to stay close together as they initially entered the chamber until they collided with the chamber wall, and then diffused into the rest of the chamber. Despite including assumptions of particle mechanical properties relevant to breakage, Han et al.'s analyses of particle feed rate, gas flow rate and nozzle angle were found to agree qualitatively with the experimental work of Tuunila and Nyström (1998), Gommeren et al. (2000), and Ramanujam and Venkateswarlu (1969). Levy and Kalman (2007) investigated the classification process of the spiral jet mill using just CFD. They ignored inter-particle interactions, using the Eulerian-Lagrangian approach (Lagrangian Particle Tracking) with the standard k-ε turbulence model. They fed the product size distribution from an experimental milling case into the simulation and found that not all particles escaped the mill. Teng et al. (2009) carried out single-phase gas flow simulations of a spiral jet mill using the k-ε turbulence model to study the influence of operating conditions on the fluid velocity. They found that the injector pressure has a less significant influence on the velocity magnitude of the fluid compared to the grinding pressure. Interestingly they also found there to be a decrease in the velocity magnitude of the fluid in the grinding chamber as the radial distance from the central outlet decreased, contrary to the results of Han et al. (2002). Teng et al. (2011) expanded their work by carrying out DEM-CFD coupled simulations. They showed how increasing the grinding pressure supplied to the mill caused an increase in the particle velocities. They analysed the inter-particle and particle-wall collisions in the system and found that inter-particle collisions have a higher average relative velocity compared to particle-wall collisions. The tangential component of the relative velocity of the inter-particle

collisions was found to be almost eight times greater than the normal component. From this, they concluded that inter-particle collisions occur mainly in a "side-swipe" motion, and thus breakage in a spiral jet mill is due to abrasion. However, it should be noted that these simulations were of a very dilute system with only 1000 particles. They found increasing the number of particles reduced the average particle velocity, and increased the frequency of inter-particle collisions at a greater rate than particle-wall collisions. Kozawa et al. (2012) used CFD with Lagrangian Particle Tracking to investigate the effect of a classifier on the radial and tangential components of the fluid velocity, and the classification efficiency of a mill. They found that the classification efficiency from experimentation was lower than that calculated from the CFD simulation. Rodnianski et al. (2013) conducted a parametric study of a spiral jet mill to see the effects of operational and structural parameters of the spiral jet mill on the velocity flow field and derived equations that could describe the field. Brosh et al. (2008) used DEM-CFD simulations to analyse particle motion and compared particle trajectories to their experimental behaviour. They found comparable particle motion in terms of both trajectory and velocity. Brosh et al. (2014) carried out DEM-CFD simulations of the spiral jet mill using their own DEM code, incorporating breakage (Brosh et al., 2011) and van der Waals forces.

6.2.1   Summary

The simulation of the spiral jet mill is a relatively new topic of investigation, with research utilising CFD and DEM dating back less than two decades. Some simulations have been shown to qualitatively compare to experimental milling behaviour. Research has shown the gas velocity flow field of the mill grinding

chamber, although some work seems to contradict each other, with Han et al. (2002) finding the gas velocity magnitude increases towards the central outlet while Teng et al. (2009) found the opposite.

The mechanism of particle breakage as well as the fluid-particle-wall energy transfer have not been thoroughly investigated. Knowledge of the degree of inclined impacts compared to normal impacts is limited, and may be useful in establishing the method of particle breakage within the spiral jet mill.

One untapped avenue of research is the simulation of particle breakage, with only one piece of work incorporating breakage into a 3D DEM-CFD simulation by Brosh et al. (2014). With the advances in computing power and software capabilities, this is more capable of being achieved. However there are a few key properties which must be considered which make it difficult to accurately represent particle breakage, such as particle shape and the existence of cleavage planes. Consideration of the energy dissipation from collisions in the system is a good elementary method of investigating the potential for breakage.

6.3   CFD Turbulence Models

There are several models available for the modelling of turbulence using the RANS equation.

6.3.1   k-epsilon

The k-epsilon (k-ε) turbulence model is a two equation model developed by Launder and Spalding (1972). It is the most popular turbulence model and is widely used due to its robustness, computational economy and reasonable accuracy for a wide range of turbulence cases. The two transport equations obtain

two variables: (i) the turbulent kinetic energy (k) (Eq. 6.1), which is the amount of energy in the turbulence, and (ii) the turbulent dissipation rate (ε) (Eq. 6.2), which determines the rate of dissipation of the turbulent kinetic energy.

$$\frac{\partial}{\partial t}(\rho_F k) + \frac{\partial}{\partial x_i}(\rho_F k u_i) = \frac{\partial}{\partial x_j}\left[\left(\mu + \frac{\mu_t}{\sigma_k}\right)\frac{\partial k}{\partial x_j}\right] + G_k + G_b - \rho_F \varepsilon - Y_M + S_k \tag{6.1}$$

$$\frac{\partial}{\partial t}(\rho_F \varepsilon) + \frac{\partial}{\partial x_i}(\rho_F \varepsilon u_i) = \frac{\partial}{\partial x_j}\left[\left(\mu + \frac{\mu_t}{\sigma_\varepsilon}\right)\frac{\partial \varepsilon}{\partial x_j}\right] + C_{1\varepsilon}\frac{\varepsilon}{k}(G_k + C_{3\varepsilon}G_b) - C_{2\varepsilon}\rho_F\frac{\varepsilon^2}{k} + S_\varepsilon \tag{6.2}$$

$$\mu_t = \rho_F C_\mu \frac{k^2}{\varepsilon} \tag{6.3}$$

where μ is the viscosity, G_k is the generation of turbulence kinetic energy due to the mean velocity gradients, G_b is the generation of turbulence kinetic energy due to buoyancy, Y_M is the contribution of the fluctuating dilation in compressible turbulence to the overall dissipation rate, $C_{l\varepsilon}$, $C_{2\varepsilon}$, $C_{3\varepsilon}$ and C_μ are constants, σ_k and σ_ε are the turbulent Prandtl numbers for k and ε, respectively, S_k and S_ε are user-defined source terms.

The standard k-ε model has been modified to form two variations: the RNG (renormalisation group theory) k-ε model, and the realisable k-ε model. The RNG model has an addition term in the ε equation which improves the accuracy of rapidly strained flows, and also for swirling flows (ANSYS Inc, 2013).

$$\frac{\partial}{\partial t}(\rho_F k) + \frac{\partial}{\partial x_i}(\rho_F k u_i) = \frac{\partial}{\partial x_j}\left[\alpha_k \mu_{eff}\frac{\partial k}{\partial x_j}\right] + G_k + G_b - \rho_F \varepsilon - Y_M + S_k \tag{6.4}$$

$$\frac{\partial}{\partial t}(\rho_F \varepsilon) + \frac{\partial}{\partial x_i}(\rho_F \varepsilon u_i) = \frac{\partial}{\partial x_j}\left[\alpha_\varepsilon \mu_{eff}\frac{\partial \varepsilon}{\partial x_j}\right] + C_{1\varepsilon}\frac{\varepsilon}{k}(G_k + C_{3\varepsilon}G_b) - C_{2\varepsilon}\rho_F\frac{\varepsilon^2}{k} - R_\varepsilon + S_\varepsilon$$

$$\tag{6.5}$$

$$\mu_t = \mu_{t0}f\left(\alpha_s, \Omega, \frac{k}{\varepsilon}\right) \tag{6.6}$$

where α_k and α_ε are the inverse effective Prandtl numbers for k and ε, respectively, μ_{t0} is the value of turbulent viscosity calculated without swirl modification, Ω is a characteristic swirl number, α_s is a swirl constant. The turbulent viscosity is modified to account for the effects of swirl or rotation.

The realisable k-ε model has an alternative formulation for the turbulent viscosity and a modified ε equation. As with the RNG model, the realisable model has shown improvements over the standard model with flows that include strong streamline curvature, vortices, and rotation (ANSYS Inc, 2013).

$$\frac{\partial}{\partial t}(\rho_F \varepsilon) + \frac{\partial}{\partial x_i}(\rho_F \varepsilon u_i) = \frac{\partial}{\partial x_j}\left[\left(\mu + \frac{\mu_t}{\sigma_\varepsilon}\right)\frac{\partial \varepsilon}{\partial x_j}\right] + \rho_F C_1 S\varepsilon - \rho_F C_2 \frac{\varepsilon^2}{k+\sqrt{\nu\varepsilon}} + C_{1\varepsilon}\frac{\varepsilon}{k}C_{3\varepsilon}G_b + S_\varepsilon$$

$$\tag{6.7}$$

where

$$C_1 = \max\left[0.43, \frac{\eta}{\eta+5}\right] \tag{6.8}$$

$$\eta = S\frac{k}{\varepsilon} \tag{6.9}$$

$$S = \sqrt{2S_{ij}S_{ij}} \tag{6.10}$$

6.3.2 k-omega

The k-omega (k-ω) turbulence model is another two equation model, developed by Kolmogorov (1941). The difference between the k-ε and k-ω models is that k-ω solves for the specific dissipation rate of the turbulent kinetic energy (ω).

$$\frac{\partial}{\partial t}(\rho_F k) + \frac{\partial}{\partial x_i}(\rho_F k u_i) = \frac{\partial}{\partial x_j}\left[\Gamma_k \frac{\partial k}{\partial x_j}\right] + G_k - Y_k + S_k \tag{6.11}$$

$$\frac{\partial}{\partial t}(\rho_F \omega) + \frac{\partial}{\partial x_i}(\rho_F \omega u_i) = \frac{\partial}{\partial x_j}\left[\Gamma_\omega \frac{\partial \omega}{\partial x_j}\right] + G_\omega - Y_\omega + S_\omega \tag{6.12}$$

where Γ_k and Γ_ω are the effective diffusivities of k and ω, respectively, G_ω is the generation of ω due to mean velocity gradients, Y_k and Y_ω are the dissipation of k and ω due to turbulence, respectively, and S_ω is a user-defined source term. The shear-stress transport (SST) k-ω model is a modification of the k-ω model developed by Menter (1994).

$$\frac{\partial}{\partial t}(\rho_F k) + \frac{\partial}{\partial x_i}(\rho_F k u_i) = \frac{\partial}{\partial x_j}\left[\Gamma_k \frac{\partial k}{\partial x_j}\right] + G_k - Y_k + S_k \tag{6.13}$$

$$\frac{\partial}{\partial t}(\rho_F \omega) + \frac{\partial}{\partial x_j}(\rho_F \omega u_i) = \frac{\partial}{\partial x_j}\left[\Gamma_\omega \frac{\partial \omega}{\partial x_j}\right] + G_\omega - Y_\omega + D_\omega + S_\omega \tag{6.14}$$

6.3.3 Reynolds stress model

The Reynolds Stress Model (RSM) is a seven equation turbulence model developed by Gibson and Launder (1978). The model solves transport equations for the

Reynolds stresses as well as the turbulent dissipation rate. It is the most accurate turbulence model as it is capable of accounting for the effects of curvature of flow streamlines, swirl, rotation, and rapid changes in strain rate (ANSYS Inc, 2013).

$$
\underbrace{\frac{\partial}{\partial t}\left(\rho_F \overline{u_i' u_j'}\right)}_{\substack{\text{Time rate} \\ \text{of change}}} + \underbrace{\frac{\partial}{\partial x_i}\left(\rho_F \bar{u}_k{}' \overline{u_i' u_j'}\right)}_{C_{ij}\,\text{convective}\atop\text{transport}} = \underbrace{P_{ij}}_{\substack{\text{Stress} \\ \text{production}}} + \underbrace{D_{Tij}}_{\substack{\text{Turbulent} \\ \text{diffusion}}} + \underbrace{\phi_{ij}}_{\substack{\text{Pressure} \\ \text{strain}}} - \underbrace{\varepsilon_{ij}}_{\text{Dissipation}} +
$$

$$
\underbrace{F_{ij}}_{\substack{\text{Body} \\ \text{forces}}} \tag{6.15}
$$

6.4 Simulation Set-up

6.4.1 CFD Set-up

CFD simulations were conducted using ANSYS Fluent 15.0.7 (ANSYS, USA). All simulations treated the gas as compressible, with fluids treated as ideal gases. The physical properties of the fluid are listed in Table 6.1. For compressible simulations, the fluid density is calculated as follows:

$$
\rho_F = \frac{p_{op}+p}{\frac{R}{M_W}T} \tag{6.16}
$$

where p_{op} is the operating pressure (which was set to 101325 Pa), p is the local static pressure relative to the operating pressure, R is the universal gas constant, M_w is the molecular weight, and T is the temperature computed by the energy equation. The SIMPLE pressure-velocity coupling scheme was used with first order implicit solution formulation due to second order being unstable and leading to divergence. The convergence criterion was set as 1×10^{-4} for all continuity, momentum and turbulence quantities. The boundaries and their type are detailed in Figure 6.1 and Table 6.2, respectively. The feed inlet and pressure outlet were

assumed to be atmospheric conditions, and therefore at zero gauge pressure, due to being open to the atmosphere in the experimental set-up. The under-relaxation factors used for the simulations are listed in Table 6.3. Under-relaxation is used to stabilise the convergence behaviour of the simulation.
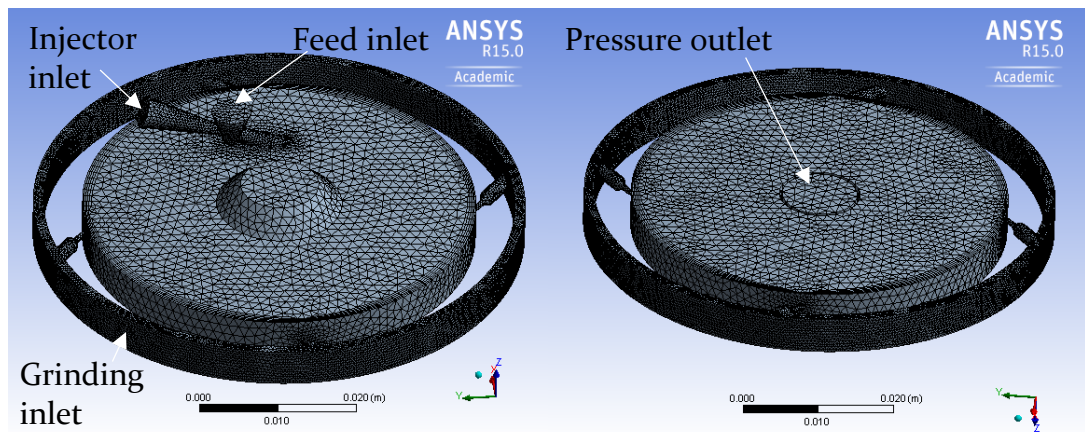
Figure 6.1: The boundary locations on the spiral jet mill geometry (mesh used in DEM-CFD simulations)

Table 6.1: Physical properties of the fluid simulated using FLUENT

Properties	Value
Specific heat, C_p (J/kg·K)	1006.43
Thermal conductivity (W/m·K)	0.0242
Viscosity (kg/m·s)	1.7894×10^{-5}
Molecular weight (kg/kgmol)	28.966

Table 6.2: Boundary conditions applied to the inlets and outlet of the spiral jet mill geometry

Boundary	Boundary type	Gauge Pressure (bar)	Diameter (m)
Feed inlet	Pressure inlet	0	0.005
Injector inlet	Pressure inlet	0 – 6	0.0009
Grinding inlet	Pressure inlet	0 – 6	0.0008
Pressure outlet	Pressure outlet	0	0.01

Table 6.3: Under-relaxation factors used for the CFD simulation in FLUENT

Pressure (-)	0.3
Density (-)	1
Body Forces (-)	1
Momentum (-)	0.7
Turbulent Kinetic Energy (-)	0.8
Turbulent Dissipation Rate (-)	0.8
Turbulent Viscosity (-)	1
Energy (-)	1

For each inlet and outlet boundary, the turbulent intensity was set to 10% and the hydraulic diameter was the diameter of the boundary, listed in Table 6.2.

6.4.1.1   Mesh Generation

Using the boundary conditions detailed in Table 6.2, with the injector inlet and grinding inlet both set to a pressure of 400 kPa (4 barg), steady-state simulations of the mill were done using four meshes, each with a different number of cells, as shown in Table 6.4. The meshes were unstructured, tetrahedron meshes. The k-ε turbulence model was used with standard wall functions, based on the law of the wall. The law of the wall gives the mean velocity near the wall:

$$U^* = \frac{1}{\kappa}\ln(C_E y^*) \qquad\qquad (6.17)$$

where U^* is the dimensionless velocity (which includes the mean velocity), y^* is the dimensionless distance from the wall, κ is the von Kármán constant (=0.4187), and C_E is an empirical constant (=9.793). y^* was within the law of the wall region ($y^* \approx 30$). An adaptive time step was used with an initial value of 1×10^{-5} s, which is where the time step is changed as the simulation progresses based on the estimation of the truncation error associated with the time integration scheme (ANSYS Inc, 2011). Each case was run until it converged, and the mass-averaged

velocity magnitude of the fluid was recorded (listed in Table 6.4). Increasing the number of cells in the mesh saw an increase in the calculated mass-average velocity magnitude in the grinding chamber. The change in the velocity magnitude when increasing the number of cells from 1.1×10^6 to 2.6×10^6 was 0.6% compared to a change of 3.5% when increasing the number of cells from 1.9×10^5 to 1.1×10^6. Figure 6.2 shows the contour plots of the four different meshes, taken from the plane in which lies the centre of the grinding nozzles. It can be seen that there is an identical fluid flow field for meshes 2 – 4. Figure 6.3 presents the instantaneous tangential velocity profile of the grinding chamber, taken along the plane illustrated in Figure 6.4 once the simulation had converged. The tangential velocity profiles show similar behaviour for meshes 2-4, although the velocity is slightly lower in mesh 2 compared to the 3 and 4. The drop in the velocity to 0 m/s at r/R of ± 0.2 is due to the presence of the wall of the central outlet at these locations. Due to the small increase in accuracy compared to the great increase in computational time between mesh 2 and 3, mesh 2 was used for all simulations.

Table 6.4: Mass average velocity magnitude in the grinding chamber with different number of mesh cells

Mesh No.	Number of cells	Max skewness	Mass average velocity (m/s)
1	1.0×10^4	0.97	70.2
2	1.9×10^5	0.84	104.8
3	1.1×10^6	0.80	108.5
4	2.6×10^6	0.80	109.2
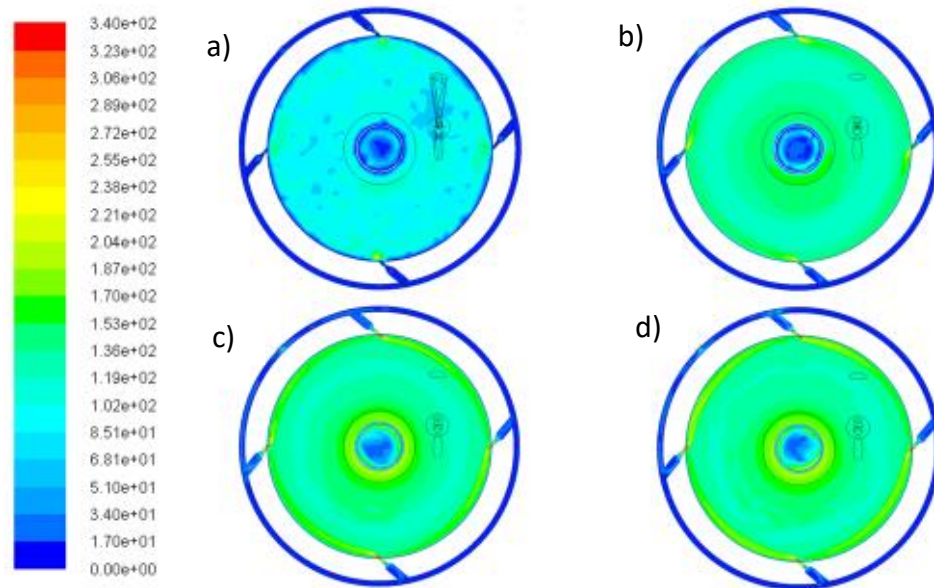
Figure 6.2: Contours of velocity magnitude with four different numbers of mesh cells: a) 1.0×10^4; b) 1.9×10^5; c) 1.1×10^6; d) 2.6×10^6 cells
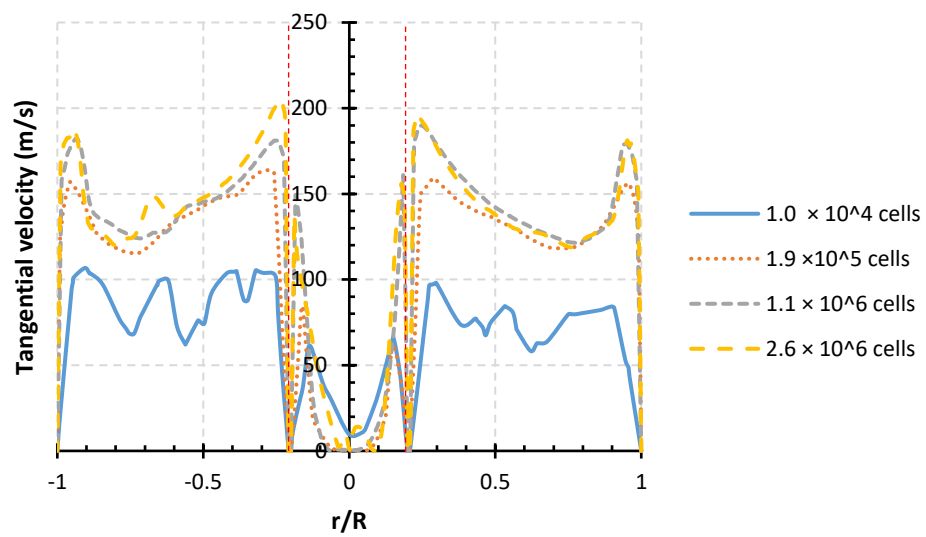
Figure 6.3: Instantaneous tangential velocity profiles of four different meshes after convergence and fully developed flow (taken along the plane illustrated in Figure 6.4)
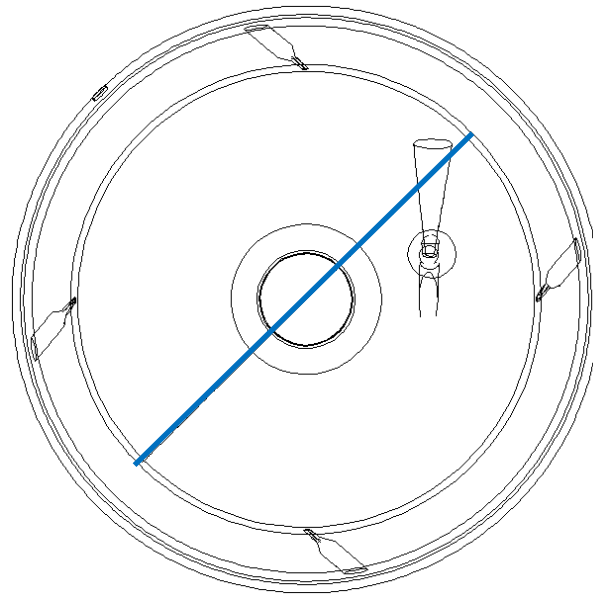
Figure 6.4: Blue line representing the plane along which the tangential velocity profiles are taken

6.4.1.2 Turbulence model comparison

The mill was simulated at a grinding and injector pressure of 400 kPa each with different turbulence models to see the effect on the velocity gradients in the velocity flow field. The simulations were run until they converged and the fluid flow was fully developed. The velocity magnitude contours were found to be identical for all the tested turbulence models, as shown in Figure 6.5. Figure 6.6 shows the instantaneous tangential velocity profiles of the different turbulence models, taken along the plane shown in Figure 6.4 after convergence. The k-omega model generally has the lowest tangential velocity, which the k-epsilon realisable model has the highest. Overall the profiles of the turbulence models are almost identical.
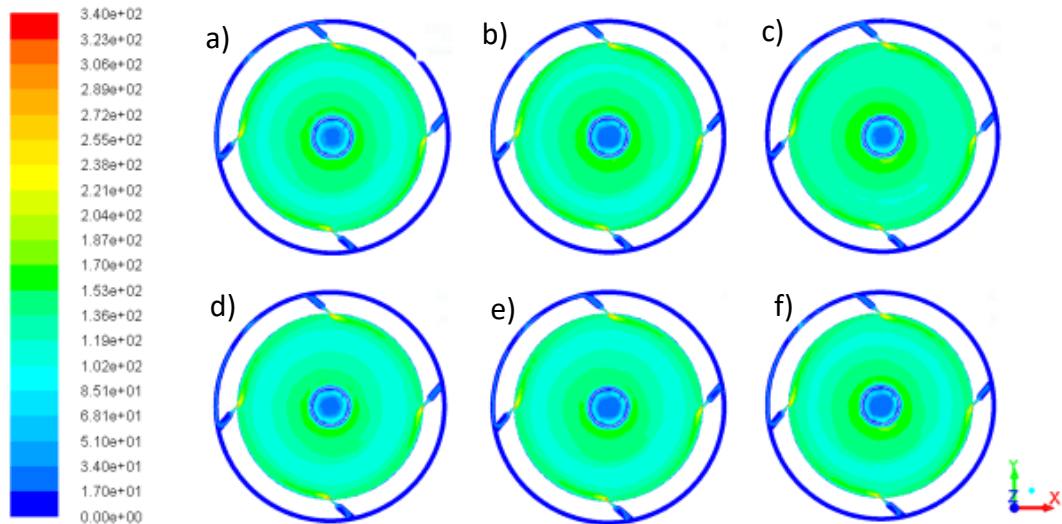
Figure 6.5: Velocity magnitude contours with a) k-epsilon standard, b) k-epsilon RNG, c) k-epsilon realisable, d) k-omega standard, e) k-omega SST, f) Reynolds Stress Model
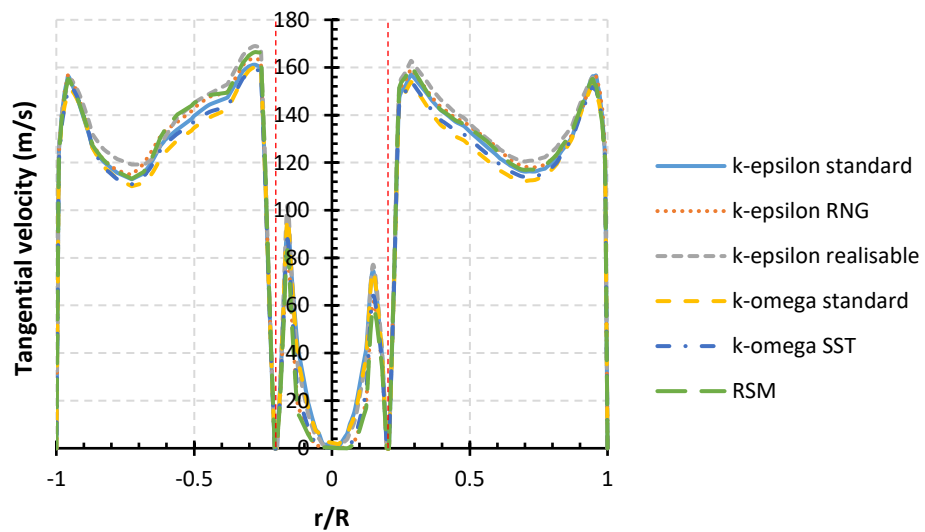
Figure 6.6: Instantaneous tangential velocity profiles of the different turbulence models after convergence and fully developed flow (taken along the plane illustrated in Figure 6.4)

6.4.1.3 Validation

The design of the Hosokawa Alpine Aeroplex Spiral Jet Mill 50AS does not allow for the visual observation of the particle motion in the spiral jet mill. Moreover, the thickness of the wall of the mill housing the grinding chamber and the particle velocities prevent the particle motion being classified by a method such as Positron

Emission Particle Tracking (PEPT). The simulation model must therefore be validated based on what can be measured experimentally: the outlet gas flow rate as a function of applied pressure.

The gas from the outlet of the grinding chamber was passed through a volumetric gas flowmeter (Hamilton Gas Products, Northern Ireland). The mill was run at different combinations of grinding and injector pressures ranging from 0 to 400 kPa (0 to 4 bar) (Table 6.5), without any particles present.

Table 6.5: Combinations of grinding and injector gauge pressures used for validation

Grinding pressure (bar)	0	0	0	0	1	2	3	4	1	1	1	2	2	3
Injector pressure (bar)	1	2	3	4	0	0	0	0	2	3	4	3	4	4

The mill was allowed to run for one minute, and the total gas flow was measured at set nozzle pressures. CFD simulations were run under the same pressure conditions, also without any particles. The volumetric flow rate through the outlet boundary was calculated. The simulations were run twice; once using the k-epsilon turbulence model, and the other with the Reynolds Stress model.

There was found to be a good correlation between the measured and calculated flow rates, with the average error between the two being 10 %, as shown in Figure 6.7. The calculated flow rates were found to be virtually identical between the k-epsilon and Reynolds Stress model. Both models are therefore suitable for flow rate calculations. The k-ε model was selected to be used for all the simulations due it being less computationally intensive than the Reynolds stress model.
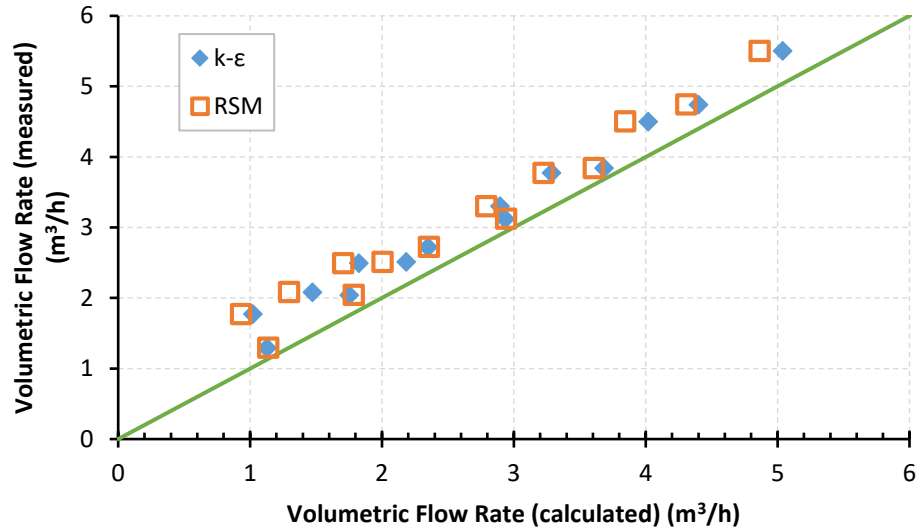
Figure 6.7: Flow rate validation – the measured air volumetric flow rate from the mill compared to the calculated flow rate

It was noted that at low grinding pressures, there is a greater contribution of air from the feed inlet to the total amount of air passing through the outlet of the chamber. It can be seen in Figure 6.8 that when the grinding pressure is 1 barg, 10 % of the total air comes from the feed inlet. When the grinding pressure is increased to 2 barg, the significance of the air entrainment through the feed inlet decreases, falling to 5 %. At 3 barg it falls to 2 %.
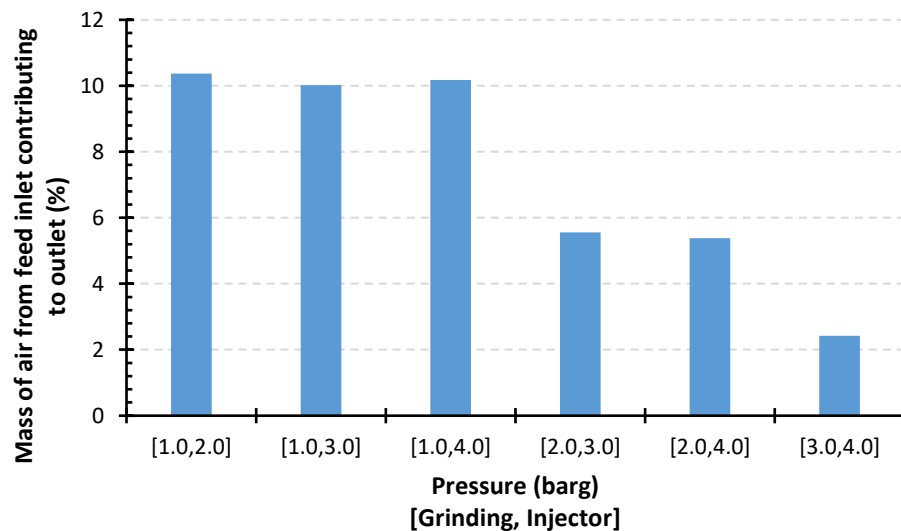
Figure 6.8: The contribution of air from the feed inlet to the total air passing through the pressure outlet

97

6.4.2   DEM Set-up

DEM calculations were carried out using EDEM 2.7.1 (DEM Solutions, UK). Two contact models were utilised in these investigations: Hertz-Mindlin no-slip (Mindlin, 1949) and the Pasha et al. (2014) models. As described in Chapter 2, the Hertz-Mindlin model is based on Eqs. 2.12 and 2.16, and the Pasha et al. model is based on Eqs. 2.26 and 2.27. The material and interaction properties used for the simulations are listed in Table 6.6 and Table 6.7, respectively. The parameters used for the Pasha et al. model can be found in Table 6.8. These stiffnesses were acquired from the load-displacement relationship of α-lactose monohydrate particles during compression using the Instron 5566 Mechanical Testing machine. For the Pasha et al. model, the coefficient of restitution can be calculated from the plastic and elastic work in the force-overlap response of contacting particles. The coefficient of restitution was calculated as approximately 0.7. A time step of 20% of the Rayleigh time step was used. There was no simulation of particle breakage.

Table 6.6: Material properties used in EDEM

Material property	Particle	Wall
Poisson's ratio, v	0.35	0.29
Density, ρ_p (kg/m^3)	1525	8000
Shear modulus, G (GPa)	0.1	0.78

Table 6.7: Interaction properties between the materials in EDEM

Interactional property	Particle-Particle	Particle-Wall
Coefficient of restitution, e	0.5 (0.7 in Pasha model)	0.5 (0.7 in Pasha model)
Coefficient of sliding friction, μ_f	0.5	0.5
Coefficient of rolling friction, μ_r	0.01	0.01

Table 6.8: Parameters used for Pasha et al. model

Parameter (N/m)	Particle-Particle	Particle-Wall
k_e (N/m)	2600	5170
k_p (N/m)	5819	11470
k_{cp} (N/m)	0	0
k_t (N/m)	5819	11470
f_0 (N)	0	0
f_{0p} (N)	0	0

6.4.3   DEM-CFD Coupling

The EDEM-FLUENT coupling is a two-way coupling module, allowing two-way momentum exchange between the solid and fluid phases. The modified continuity and momentum equations are shown in Eqs. 6.18 and 6.20, respectively.

$$\frac{\partial(\phi\rho_F)}{\partial t} + \frac{\partial}{\partial x_i}(\rho_F\phi\bar{u}_i) = 0 \tag{6.18}$$

$$\phi = 1 - \sum_{particles}\frac{n_c}{N}V_p \tag{6.19}$$

where ϕ is the fluid volume fraction, n_c is the number of sample points of a particle within the mesh cell and N is the total number of sample points. Sample points are randomly generated within the bounding box of each particle using the Monte Carlo method. Figure 6.9 shows a typical array of sample points within the bounding box of a particle.
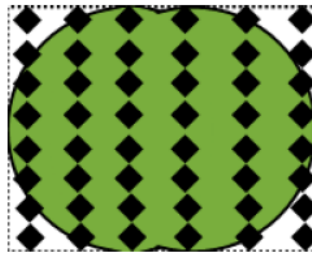
Figure 6.9: Typical array of sample points within the bounding box of a particle (DEM Solutions Ltd., 2012)

$$\frac{\partial}{\partial t}(\rho_F \phi \bar{u}_i) + \frac{\partial}{\partial x_i}(\rho_F \phi \bar{u}_i \bar{u}_j) = \frac{\partial}{\partial x_i}\left[\mu \phi \left(\frac{\partial \bar{u}_i}{\partial x_j} + \frac{\partial \bar{u}_j}{\partial x_i}\right)\right] - \frac{\partial p}{\partial x_j} + \frac{\partial}{\partial x_i}\left(-\rho_F \phi \overline{u_i' u_j'}\right) + F_b + F_s$$

(6.20)

where F_s is as follows:

$$F_s = \frac{\sum_i^n F_D + F_{saff} + F_{Mag}}{V_m}$$

(6.21)

where V_m is the CFD mesh cell volume, F_D is the drag force, F_{saff} is the Saffman lift force, and F_{Mag} is the Magnus lift force. The Di Felice drag model was used:

$$F_D = 0.5 C_D \rho_F A_p (v_f - v_p)|v_f - v_p| \cdot \phi^{-(\chi+1)}$$

(6.22)

$$C_D = \left(0.63 + \frac{4.8}{Re^{0.5}}\right)^2$$

(6.23)

$$\chi = 3.7 - 0.65 \exp\left[-\frac{(1.5 - log_{10} Re)^2}{2}\right]$$

(6.24)

The Saffman (Eq. 6.25) and Magnus (Eq. 6.26) lift forces are as follows:

$$\boldsymbol{F}_{saff} = 1.61 d_p^2 (\mu_f \rho_F)^{1/2} |\boldsymbol{\omega}_f|^{-1/2} [(\boldsymbol{v}_f - \boldsymbol{v}_p) \cdot \boldsymbol{\omega}_f] \tag{6.25}$$

where $\boldsymbol{\omega}_f$ is the fluid vorticity.

$$\boldsymbol{F}_{Mag} = 0.125 \pi d_p^3 \rho_F \frac{Re_S}{Re_\Omega} C_L [(0.5\boldsymbol{\omega}_f - \boldsymbol{\omega}_p) \cdot (\boldsymbol{v}_f - \boldsymbol{v}_p)] \tag{6.26}$$

$$C_L = 0.45 + \left(\frac{Re_\Omega}{Re_S} - 0.45\right) \exp(-0.05684 Re_\Omega^{0.4} Re_S^{0.3}) \tag{6.27}$$

Fluid-induced torque, $\boldsymbol{T}_{fp}$, was also applied to the simulation.

$$\boldsymbol{T}_{fp} = \frac{\rho_F d_p}{2} C_R^5 \left|\frac{1}{2}\boldsymbol{\omega}_f - \boldsymbol{\omega}_p\right| \left(\frac{1}{2}\boldsymbol{\omega}_f - \boldsymbol{\omega}_p\right) \tag{6.28}$$

$$C_R = \begin{cases} \dfrac{64\pi}{Re_\Omega} & Re_\Omega \leq 32 \\ \dfrac{12.9}{Re_\Omega^{0.5}} + \dfrac{128.4}{Re_\Omega} & 32 \leq Re_\Omega \leq 1000 \end{cases} \tag{6.29}$$

The fluid-induced torque is incorporated as follows:

$$I \frac{d\boldsymbol{\omega}_p}{dt} + \boldsymbol{\tau}_i + \boldsymbol{T}_{fp} = \boldsymbol{M} \tag{6.30}$$

where $\boldsymbol{\tau}_i$ is as previously shown in Eq. 2.21.

6.4.4 Lagrangian Particle Tracking

For the discrete phase simulations using only FLUENT software, particles were

modelled using the Lagrangian approach. This is also referred to as Lagrangian

Particle Tracking. FLUENT predicts the trajectory of the particles by solving the particle motion equation, as shown:

$$\frac{dv_p}{dt} = F_d(\bar{u} - v_p) + \frac{g(\rho_p - \rho_F)}{\rho_p} + \frac{F_{saff}}{\rho_p} \tag{6.31}$$

The drag force is given by:

$$F_d = \frac{18\mu}{\rho_p d_p^2} \frac{C_D Re}{24} \tag{6.32}$$

where the Reynolds number, *Re*, is based on the relative velocity of the particle, as given by:

$$Re = \frac{\rho_F d_p |v_p - \bar{u}|}{\mu} \tag{6.33}$$

Turbulent dispersion was taken into account in the Lagrangian Particle Tracking simulations using the discrete random walk model. Walls were given a roughness height of 0.8 μm and roughness constant of 0.5. Wall collisions were set for particles to reflect upon impact with a coefficient of restitution of 0.5 in both the normal and tangential direction.

6.4.5   Simulation Cases

Using CFD coupled with DEM, the following cases were investigated:

1. The transfer of energy between the fluid, particles, and grinding chamber wall (all with a constant grinding and injector pressure of 300 kPa and 400 kPa, respectively)

   - Cases 1 – 4

2. The effect of gas pressure and particle concentration on the particle velocities and fluid flow

- Case 5

Table 6.9 shows details of the number of particles and their sizes used for each simulation case, and Table 6.10 shows the particle size distributions used for cases 1 – 4. Hertz-Mindlin was used for the energy transfer simulation cases 1 – 4 (described in Section 6.5.2 below). The Pasha et al. model was used for the simulations in case 5.

Table 6.9: Number and size of particles used in CFD-DEM simulations

	Number of particles	Particle size (µm)	Contact model
Case 1	10,000	10 – 100 (Distr 1)	Hertz-Mindlin
Case 2	10,000	10 – 100 (Distr 2)	Hertz-Mindlin
Case 3	100,000	10 – 100 (Distr 1)	Hertz-Mindlin
Case 4	1,000,000	10 – 100 (Distr 1)	Hertz-Mindlin
Case 5	2,500 5,000 10,000 20,000	425	Pasha et al.

Table 6.10: Number % of each particle size in the poly-disperse simulations

Particle size (µm)		10	20	50	75	100
Number	Distr 1	62.9	31.4	5.03	0.60	0.07
%	Distr 2	20	20	20	20	20

The particles in the energy transfer simulation cases 1 and 2 were generated in the factory shown in Figure 6.10. The factory used for all other simulations (cases 3 – 5) is shown in Figure 6.11.
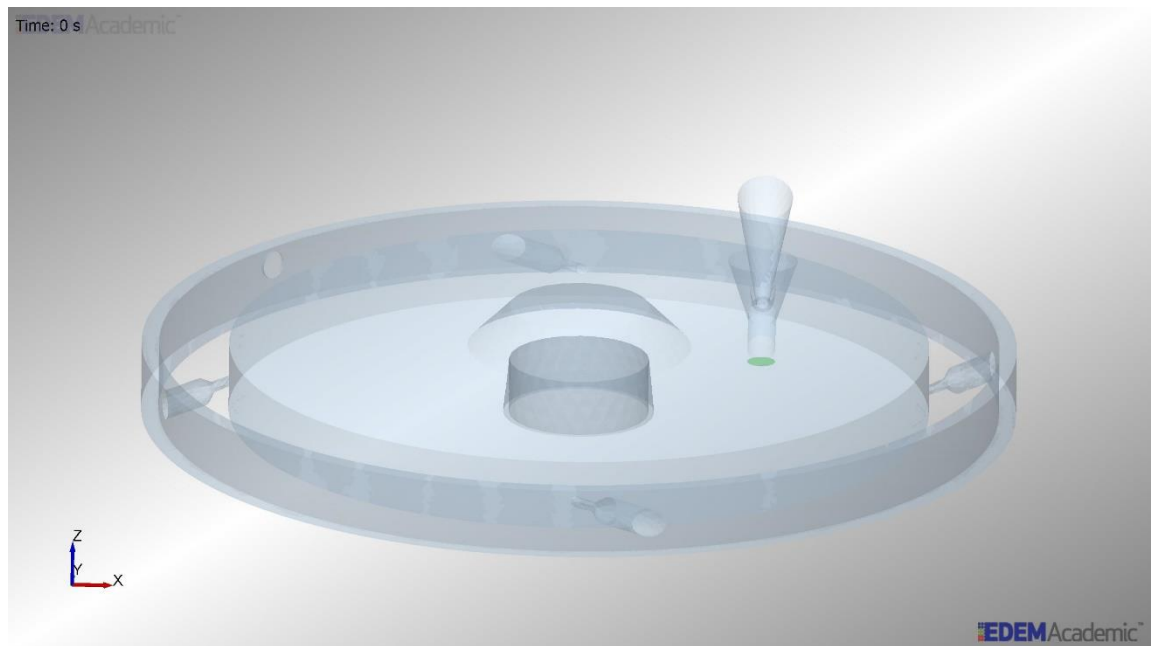
Figure 6.10: Factory in which particles are generated in energy transfer simulation cases 1 and 2 (green section at injector nozzle)
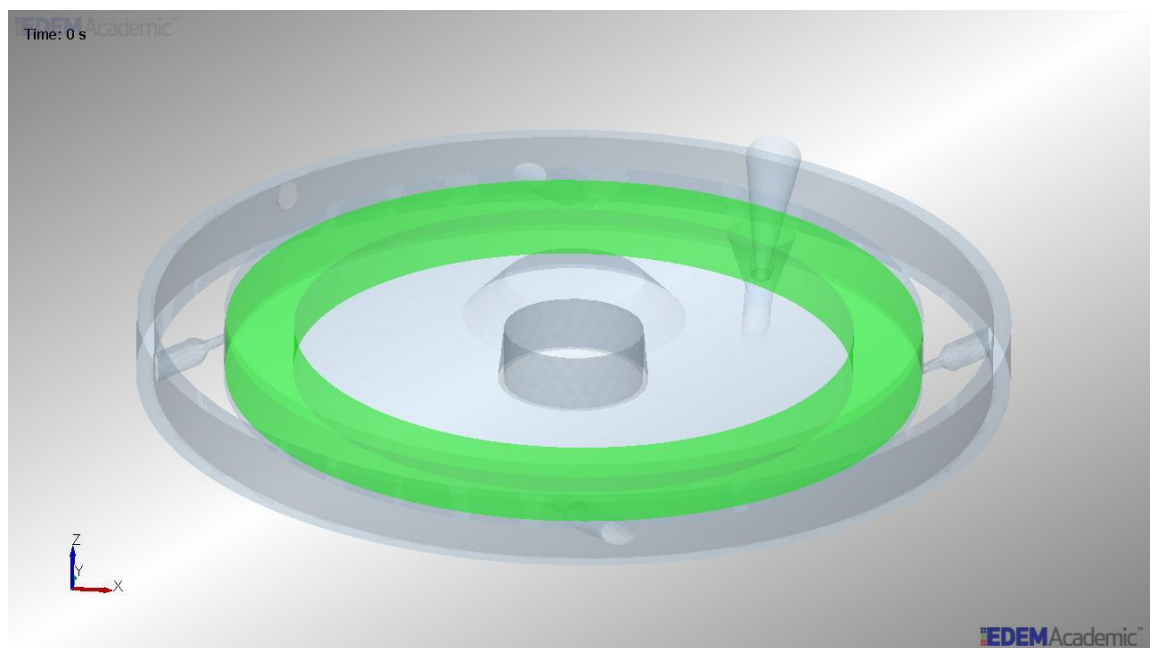
Figure 6.11: Factory in which particles are generated in cases 3 – 5 (green section)

Elghobashi (1991) described there as being three types of particle-fluid flow which depends on the particle concentration in the fluid. When the particle concentration is less than 10^{-6}, the particle-fluid mixture is described as a dilute suspension, where the presence of the particles has a negligible effect on

turbulence in the system. For concentrations between 10^{-6} and 10^{-3}, the particle-fluid mixture is considered a dilute suspension, however the particle concentration is large enough to have an effect on the turbulent flow of the fluid. This is two-way coupling. When the concentration is above 10^{-3}, the suspension is considered dense, and particles affect both the fluid and each other through particle-particle collisions. Elghobashi (1991) called this four-way coupling. Table 6.11 lists the particle volume fractions for the various simulated cases. All cases were found to have a concentration of particles which affect the fluid turbulence. The simulations with poly-disperse particles from size 10 – 100 μm (Cases 1 – 4) all had a concentration which corresponds to a dilute suspension. The simulations with mono-sized 425 μm particles (Case 5) were considered dense suspensions.

Table 6.11: Particle volume fractions in the grinding chamber of the simulated DEM-CFD cases

	No. of particles	Particle volume fraction	Details
Case 1	10,000	8×10^{-6}	Dilute, two-way coupling
Case 2	10,000	2×10^{-4}	
Case 3	100,000	8×10^{-5}	
Case 4	1,000,000	8×10^{-4}	
Case 5	2,500	1.2×10^{-2}	Dense, four-way coupling
	5,000	2.4×10^{-2}	
	10,000	4.7×10^{-2}	
	20,000	9.4×10^{-2}	

For a stable simulation, the CFD mesh cell size must be larger than the largest particle size. It is recommended that the mesh size be at least double the particle diameter (Chaumeil and Crapper, 2014). The limitations of this are that the mesh must be coarsened to accommodate for larger sized particles, thus decreasing the accuracy of the CFD calculations. However, the jet mill geometry is complex and contains small sized components such as the grinding nozzles which need a fine

cell size in order to mesh properly. The outer wall of the central chamber region where the particles are contained was restricted to have a minimum mesh cell size that is the size of the largest particle in the simulation. Inflation was also used at the outer wall, with a minimum of 5 layers and a growth rate of 1.1. The nozzles had 8 mesh cells across their diameter. Using a mesh with a cell size of double the maximum particle diameter of 100 μm used in the energy transfer simulations in Section 6.5.2 below led to considerably lengthy simulation times and was not feasible. A mesh size of five times the diameter was used instead. For the simulations where the particle diameter was 425 μm, a cell size of double the diameter was used. The mass average velocity of gas in the mill for each mesh is listed in Table 6.12. It can be seen that there is a decrease in the velocity compared to that of the meshes for CFD only simulations (Table 6.4). However, it was noted that the coarsening of the mesh did not have an adverse effect on the velocity magnitude contours, as shown in Figure 6.12. Similar velocity gradients to those in Figure 6.5 are seen, suggesting the turbulent behaviour is the same. The tangential velocity profiles illustrated in Figure 6.13 also show the same trend in velocity across the grinding chamber and similar velocities in the central region and close to the outlet. However the tangential velocity is lower at the outer wall and inside the outlet when the cell size is 2×425 μm compared to 5×100 μm.

Table 6.12: Mass average velocity magnitude of coarsened meshes for DEM-CFD simulations

Mesh cell size	Number of cells	Max skewness	Mass average velocity (m/s)
2×100 μm	1.85×10^5	0.89	96.9
5×100 μm	1.80×10^5	0.93	90.4
2×425 μm	1.76×10^5	0.87	83.4
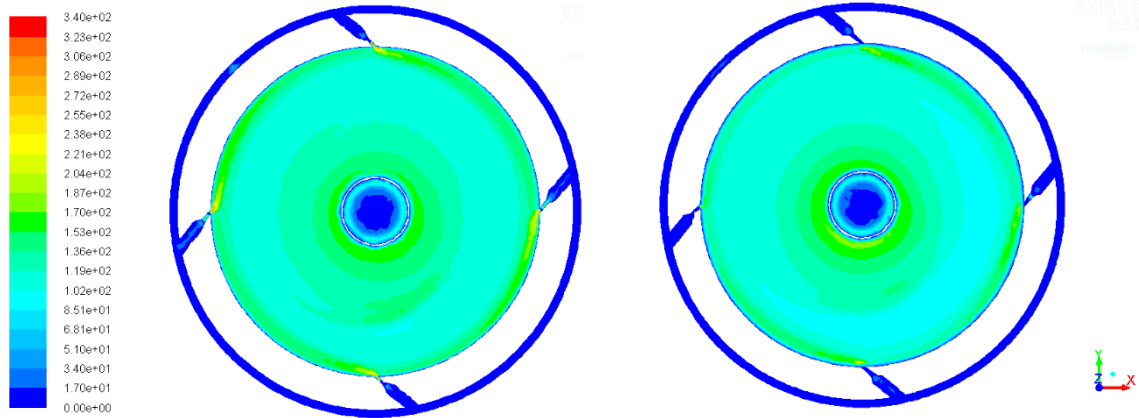
Figure 6.12: Velocity magnitude contours with mesh cell sizes (left: 5 × 100 μm | right: 2 × 425 μm)
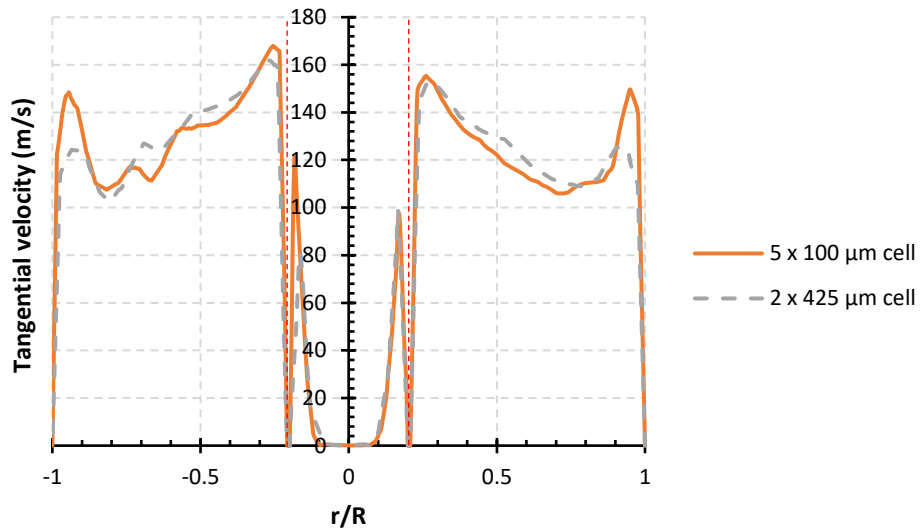
Figure 6.13: Instantaneous tangential velocity profiles of the different mesh cell sizes after convergence and fully developed flow

Before particles were inserted into the coupled simulations, the fluid flow calculation was allowed to reach steady state. Steady state was regarded as there being a constant gas velocity magnitude with respect to time within the grinding chamber. In the 50 mm grinding chamber, this was reached after 0.03 s of simulation.

6.5   Results of the Simulation of the Spiral Jet Mill

6.5.1   Classification efficiency

Using CFD with Lagrangian Particle Tracking and no interparticle interactions, 1,000 monosized particles were inserted into the grinding chamber from the feed inlet boundary. The particle sizes ranged from 1×10^{-7} m (0.1 μm) to 5×10^{-4} m (500 μm). The grinding and injector pressures ranged from 100 – 400 kPa (1 – 4 barg).

Particle sizes of 2 μm were found to be the largest size that can escape from the Hosokawa Alpine Aeroplex Spiral Jet Mill 50AS by internal classification, as illustrated in Figure 6.14. Increasing the grinding gas pressure led to a reduction in the particle size that underwent internal classification. Figure 6.15 shows the classification efficiency results with respect to the particle concentration present in the grinding chamber. It can be seen that when the classification efficiency reaches a constant level once the particle concentration is smaller than 10^{-6}, which is the solid volume fraction below which the particles have an insignificant effect on the turbulence in the fluid, as described by Elghobashi (1991). Above 10^{-3}, which is where the solid volume fraction is large enough that the particles affect both the fluid behaviour and their own, no particles escape from the chamber.
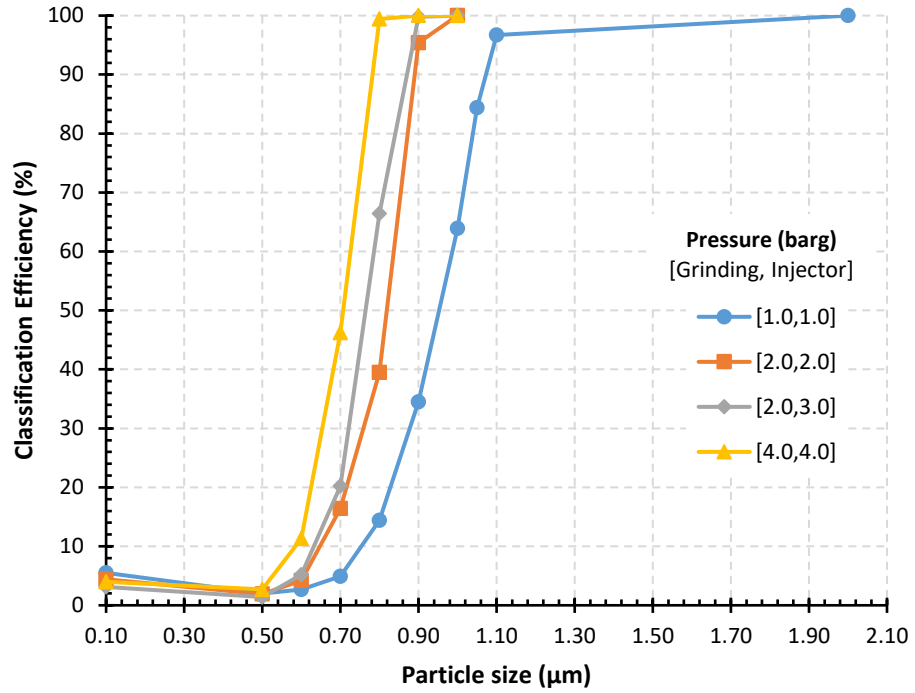
Figure 6.14: Classification efficiency with respect to particle size at different grinding pressures of the Hosokawa Alpine Aeroplex Spiral Jet Mill 50AS
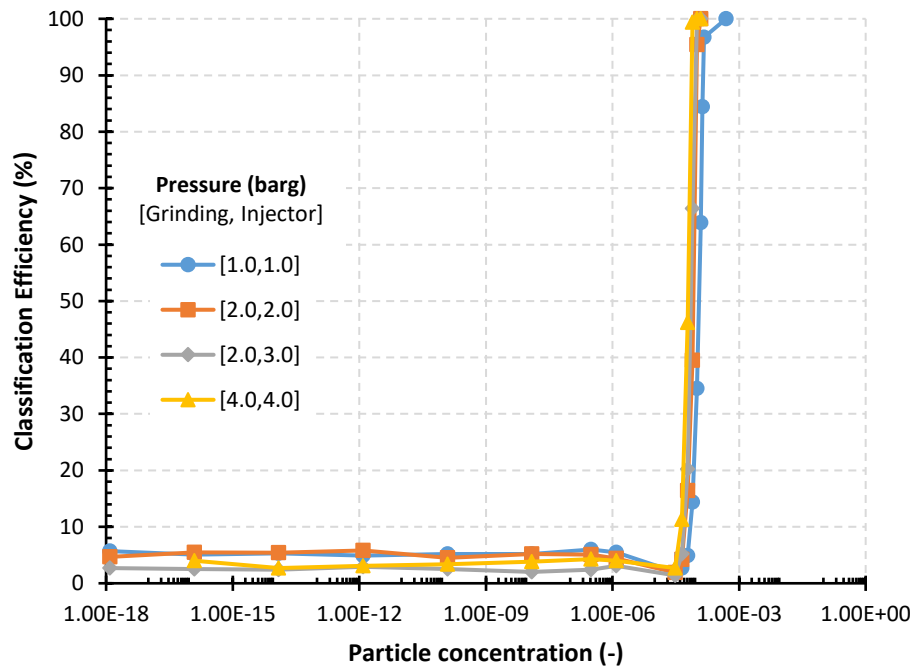
Figure 6.15: Classification efficiency with respect to particle concentration at different grinding pressures of the Hosokawa Alpine Aeroplex Spiral Jet Mill 50AS

This classification behaviour suggests that fluid forces alone are not responsible for particles escaping from the grinding chamber. The simulation indicates that only

very small particle sizes are removed from the chamber due to drag forces. As was seen in Chapter 5, as the feed particles fill the chamber some are forced out of the chamber by the increasing particle mass within. The particle mass present in the grinding chamber, and internal classification are therefore both important parts of the classification process. The particle mass will influence the interparticle behaviour in the mill. Particle shape can also have an effect, as it affects the amount of drag acting on the particles.

6.5.2 Fluid-Particle-Wall Energy Transfer (Cases 1 – 4)

In this section, a different particle size distribution was used for simulations, with the particle number percentage distribution detailed in Table 6.9 and Table 6.10. Case 2 used an equal number of each particle size to remove any potential effect of the large number of fine particles compared to coarse particles on the energy transfer. For all simulations, a grinding and injector pressures of 300 kPa and 400 kPa (3.0 and 4.0 barg), respectively, were used.

Using simulation Case 1, the dissipated energy of inter-particle and particle-wall collisions were analysed. It was found that the dissipated energy from inter-particle collisions are greater than that of particle-wall collisions, illustrated in Figure 6.16. This indicates that the former has a greater contribution to particle breakage than the latter.
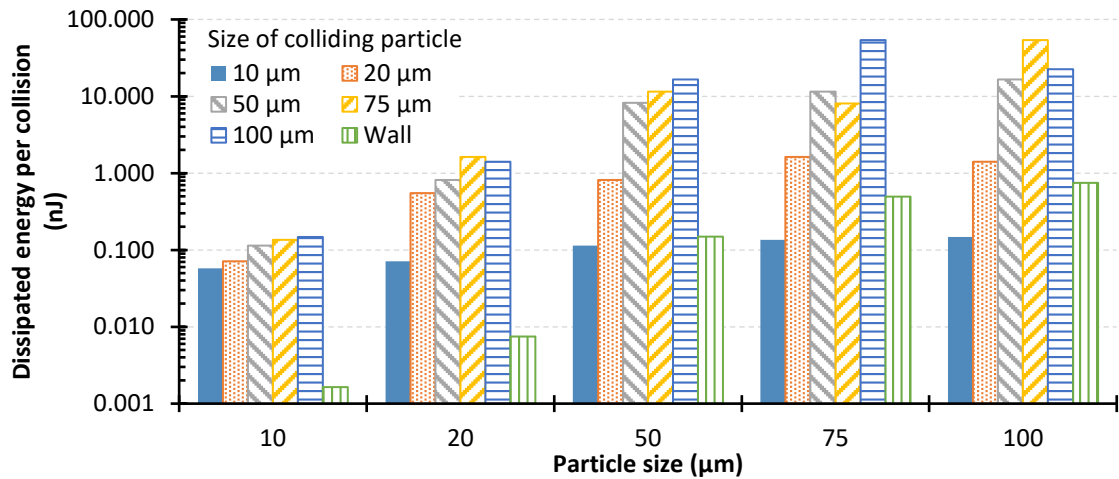
Figure 6.16: Dissipated energy per normal inter-particle and particle-wall collisions (Case 1)

Looking further into the energy transfer during collisions, the various possible particle size combinations of inter-particle collisions in Case 1 were analysed and are illustrated in Figure 6.17. The x-axis indicates the pair of colliding particles; for example, "10 × 10" is an inter-particle collision between two 10 μm particles, while "20 × 75" is between a 20 and 75 μm particle. For each pair of colliding particles, the amount of specific energy dissipated from the collision was identified, as well as the frequency of occurrence of that amount of energy dissipation. The frequency was normalised by the maximum frequency value to show the relative contributions. It shows that collisions between 10 and 20 μm particles have the highest frequency of occurrence compared to the other possible collisions. They also have a moderately high specific dissipated energy of 101 – 150 J/kg. This suggests that collisions between these two particles will have the highest rate of breakage compared to others.
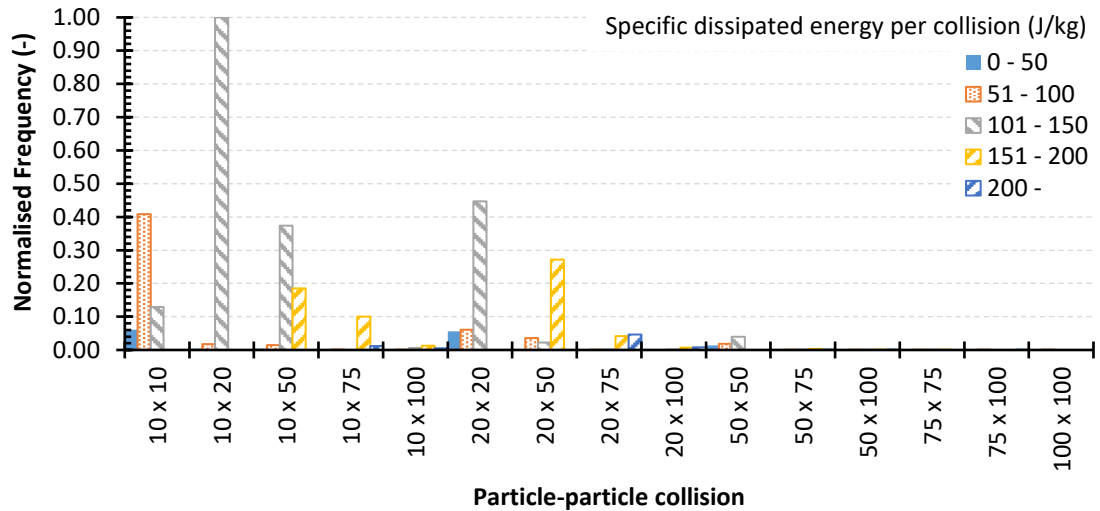
Figure 6.17: Specific dissipated energy per collision and its normalised frequency for every possible inter-particle collision (Case 1)

In the collision theory of chemical reactions, the collision frequency of two reacting particles is given by the following equation:

$$Z_{AB} = N_A N_B (r_A + r_B)^2 \sqrt{\frac{8\pi K_B T}{\mu_{AB}}} \qquad (6.34)$$

where N_A and N_B are the number of A and B particles, respectively, r_A and r_B are the radii of particles A and B, respectively, k_B is the Boltzmann constant, T is the temperature, and μ_{AB} is the reduced mass of particle A and B. Figure 6.18 shows the collision frequency of the particles in the system based on Eq. 6.34. The same bimodal trend as that in Figure 6.17 can be seen.
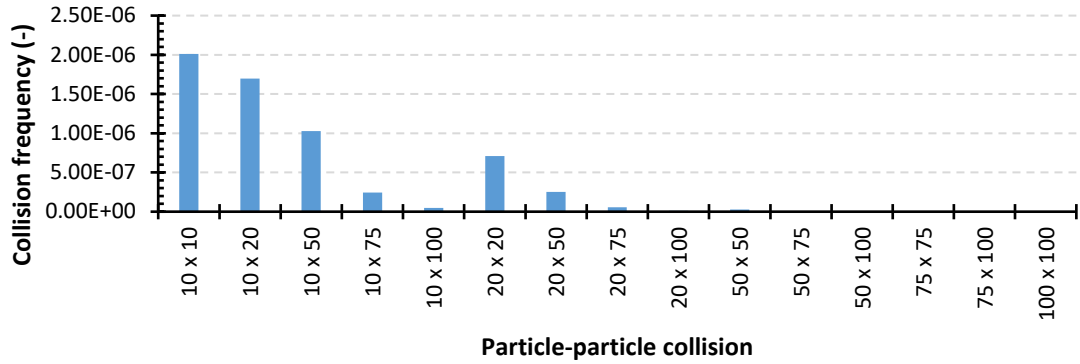
Figure 6.18: Collision frequency in Case 1 based on the collision frequency equation

The same analysis was carried out with Case 2 (the same particle sizes as Case 1 but with an equal number of each particle), the results of which can be seen in Figure 6.19. Again 10 and 20 μm particle collisions have the highest collision frequency, as well as high specific dissipated energy values of at least 301 J/kg. This shows that the high collision frequency was not a result of the particle size distribution. It also suggests the existence of an optimum size ratio for particle breakage in the mill.
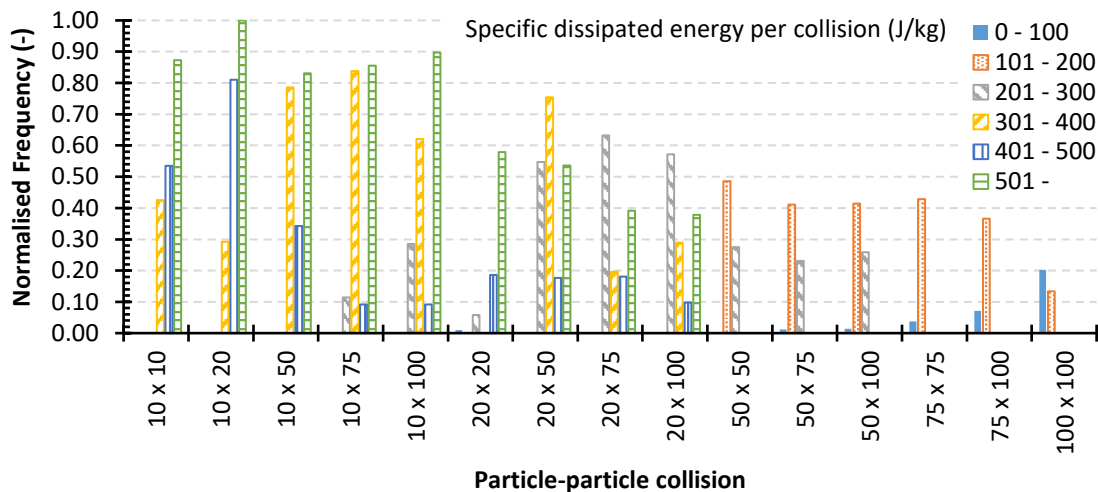
Figure 6.19: Specific dissipated energy per collision and its frequency for every possible inter-particle collision (Case 2)

The 10 and 20 μm particles were found to have the highest relative collisional velocities, illustrated by the probability density function in Figure 6.20. This

113

further supports the idea that collisions between 10 and 20 µm particles may have

the highest rate of breakage and may be an optimum colliding particle size pair.
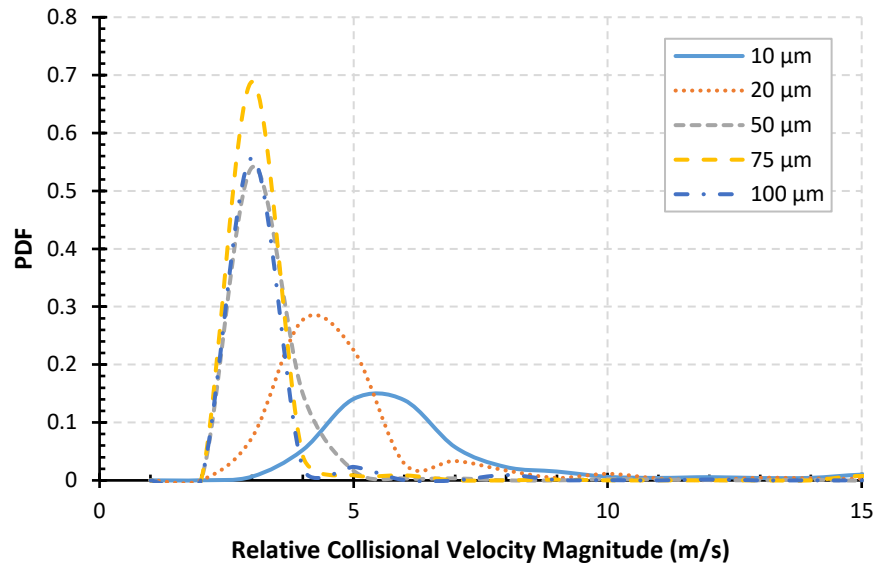
Figure 6.20: Velocity distribution of different particle sizes

The particles were found to segregate based on their size as they circulate around

the outer wall, as can be seen in Figure 6.21. Close to the outer wall (between

0.0248 – 0.025 m), the size of the particles increases as the radial distance from

the central outlet decreases. Less than 0.0248 m, it can be seen that there are a

number of 10 µm particles, which have been blown away from the wall by the

grinding nozzle.
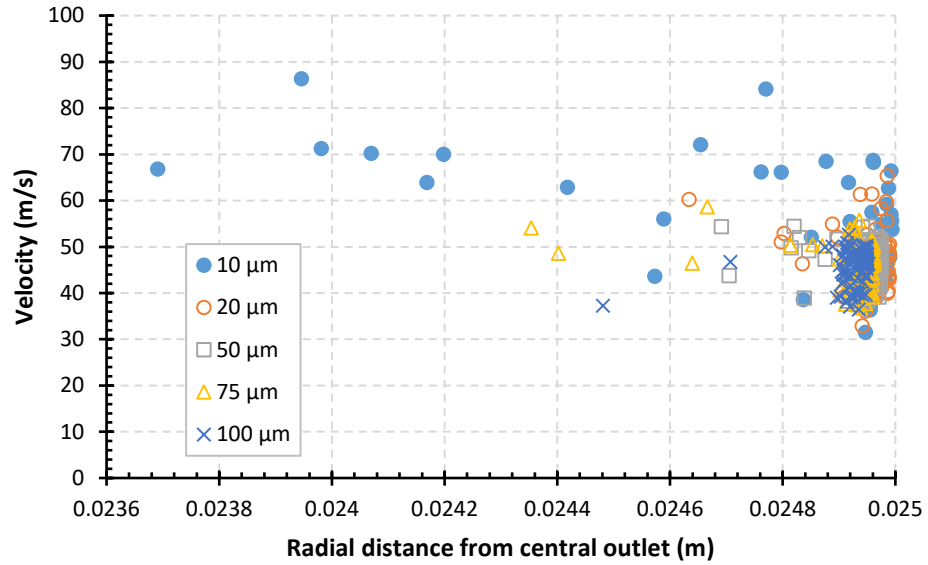
Figure 6.21: Velocity magnitude and distance from central outlet of the different particle sizes (2000 of each particle size)

Using the collision frequency equation in Eq. 6.34, a bimodal trend is seen, as with Figure 6.19. The high collision frequency of the fine particles is not represented, however, as the collision frequency equation only considers a binary particle system and so does not take into account the particle segregation seen in the grinding chamber, and the impedance caused the presence of the other particle sizes.
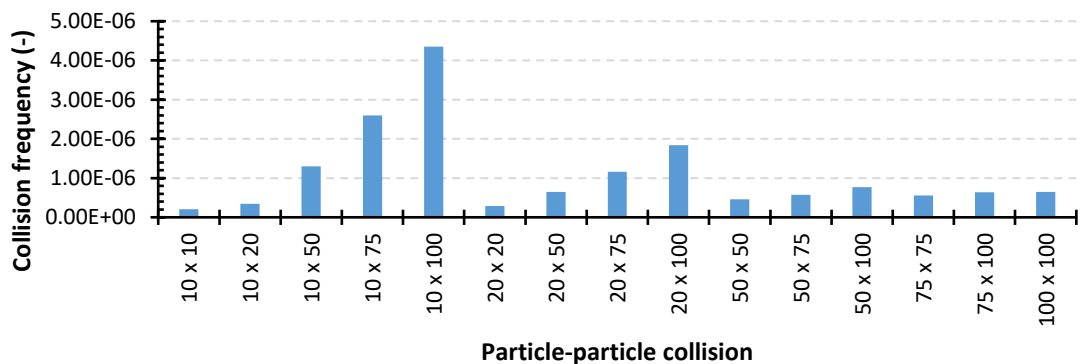
Figure 6.22: Collision frequency in Case 2 based on the collision frequency equation

Using distribution 1 detailed in Table 6.10, the dominant type of collision was found to be influenced by the number of particles present in the grinding chamber, shown in Table 6.13. When there are 10^4 particles (Case 1) the majority of collisions are particle-wall (96.5%) rather than inter-particle collisions (3.5%). Most of the dissipated energy in the system comes from the particle-wall collisions (95.9%). When the number of particles increases to 10^5 particles (Case 3), the proportion of inter-particle collisions increases to 40.8%, but most of the dissipated energy is now lost through this type of collision (71.2%). With 10^6 particles (Case 4), inter-particle collisions are dominant both in terms of number and dissipated energy. The degree of transfer of energy from the fluid to the particles was also analysed. This was calculated by dividing the total amount of energy present in the particles by the kinetic energy of the fluid input to the system. It was found that the amount of energy transferred from the fluid to the particles increased with the number of particles. Overall there is a very small amount of energy transferred to the particles, with only 0.02% being transferred to 10^6 particles. This highlights the energy inefficiency of the spiral jet mill.

Table 6.13: Change in the dominant collision type with number of particles

No of particles	10^4	10^5	10^6
Total no of collisions	11×10^6	48×10^6	642×10^6
No. of inter-particle collisions (%)	3.5	40.8	89.5
No of particle-wall collisions (%)	96.5	59.2	10.5
Particle-particle energy (%)	4.1	71.2	97
Particle-wall energy (%)	95.9	28.8	3
Fluid-particle energy transfer (%)	0.012	0.016	0.02

6.5.3 Effect of gas pressure and particle number (Case 5)

Case 5 examines the effect of gas pressure and the number of particles in the grinding chamber on the particle velocities and the fluid flow. As mentioned in Table 6.9, the simulations contained a single particle size of 425 μm.

6.5.3.1 Effect of gas pressure

With 20,000 particles present in the chamber, there is generally an increase in the particle velocity magnitude with the pressure, albeit insignificant, as seen in Figure 6.23. The velocity magnitude increases from 1.44 to 1.88 m/s. The distribution of the particle velocity magnitude can also be seen to widen as the gas pressure increases.
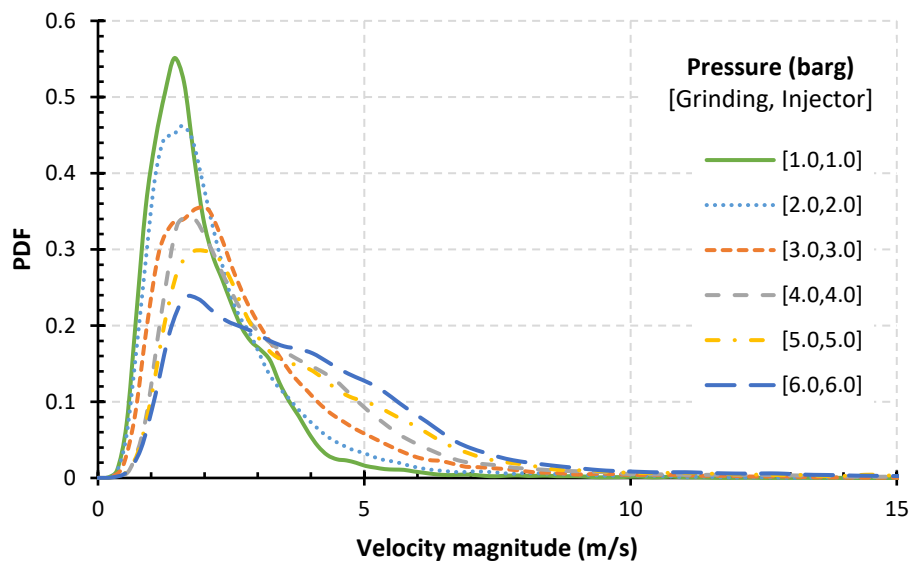
Figure 6.23: Velocity magnitude distribution of 20,000 particles at different grinding conditions

With 10,000 particles, the particle velocity magnitude increases as the grinding pressure increases, shown in Figure 6.24. The velocity magnitude increases from 2.0 to 3.5 m/s at the investigated pressures, and as with 20,000 particles, the distribution of particle velocities also increases with the pressure.

117
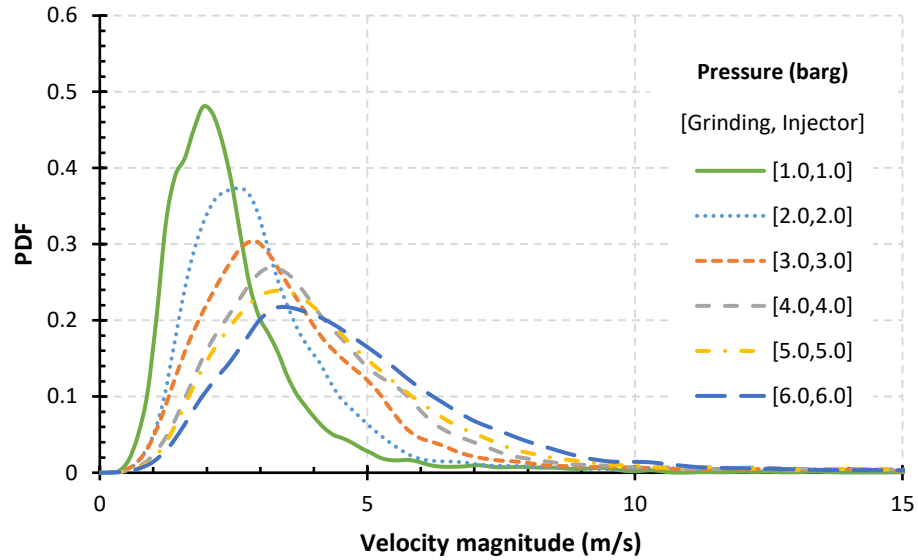
Figure 6.24: Velocity magnitude distribution of 10,000 particles at different grinding conditions

With 5,000 particles there is an increase in the particle velocity magnitude compared to 10,000 particles, with particles having the highest probability of having a velocity magnitude of between 2.5 – 5.5 m/s at the investigated pressures. This is due to particles having a greater amount of space in the chamber to accelerate and reach higher velocities before experiencing a collision. The velocity distribution is shown in Figure 6.25.
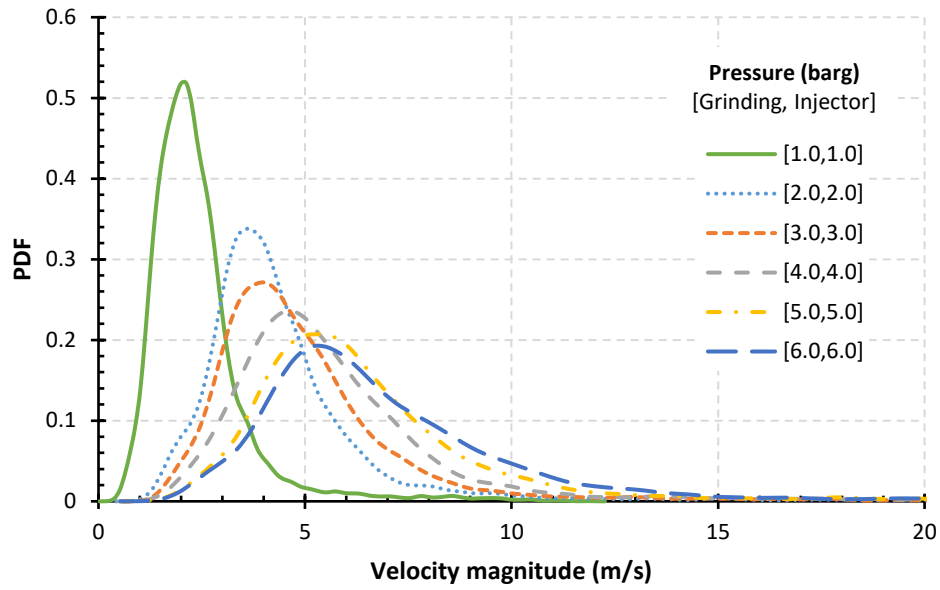
Figure 6.25: Velocity magnitude distribution of 5,000 particles at different grinding conditions

The particle velocities further increase when reducing the number of particles to 2,500, illustrated in Figure 6.26. Particles have the greatest probability of having a velocity magnitude that falls between 4 m/s to 8.5 m/s.
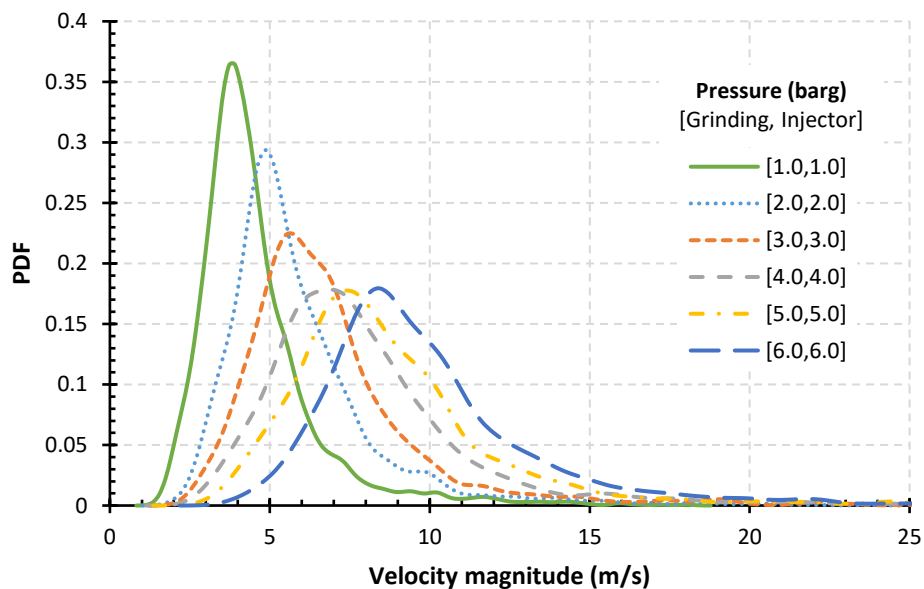
Figure 6.26: Velocity magnitude distribution of 2,500 particles at different grinding conditions

In the case of relative velocities of inter-particle collisions, the changes in the average relative velocity and the velocity distributions with 20,000 particles are

less pronounced. The average relative velocity magnitude increases from 0.2 – 0.35 m/s when the grinding and injector nozzle pressures are increased as shown in Figure 6.27, together with the distribution. Decreasing the number of particles leads to larger relative velocities (ranging from 0.5 – 1.5 m/s, 1.5 – 3.0 m/s and 3.5 – 7.5 m/s for 10,000, 5,000 and 2,500 particles, respectively) and wider relative velocity distributions, as can be seen in Figures 6.21 – 6.23.
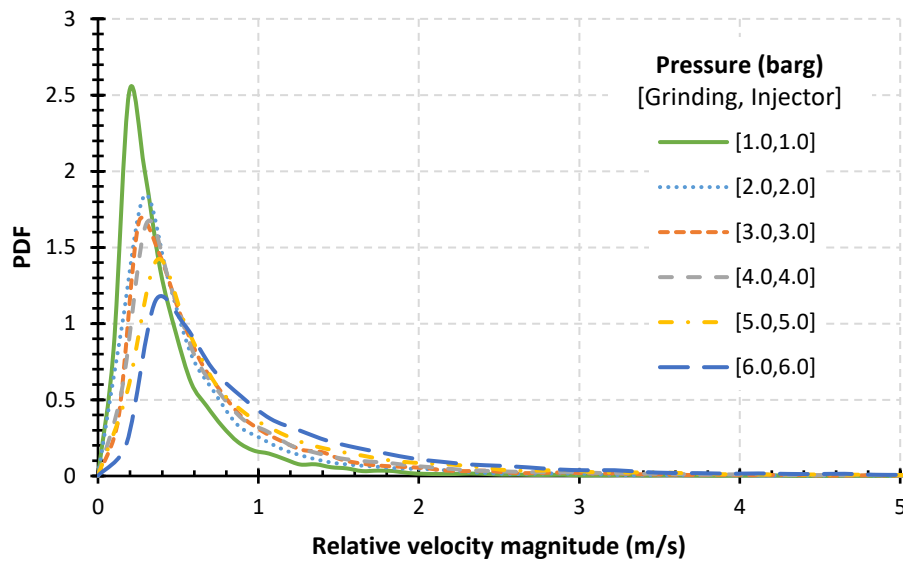
Figure 6.27: Relative velocity magnitude distribution of 20,000 particles at different grinding conditions
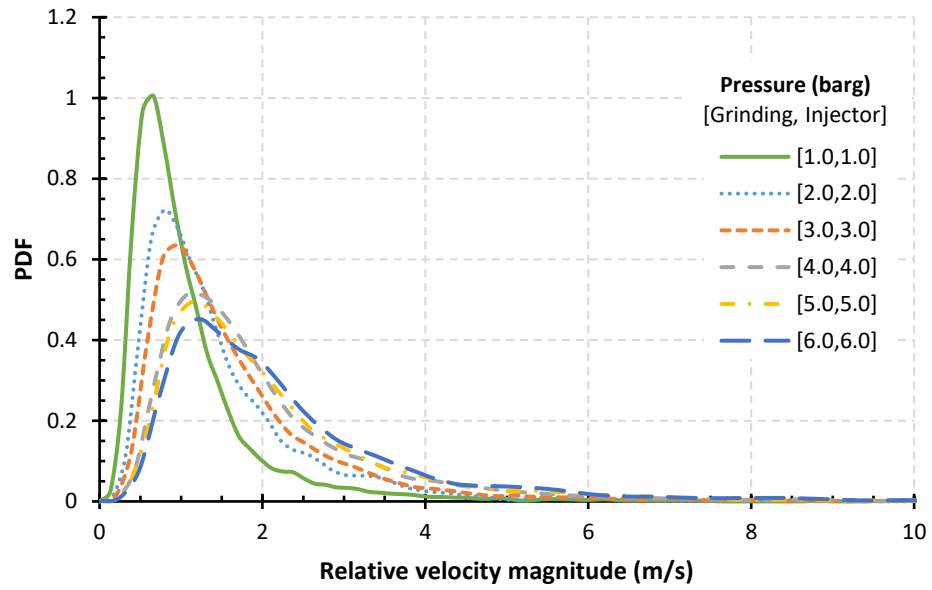
Figure 6.28: Relative velocity magnitude distribution of 10,000 particles at different grinding conditions
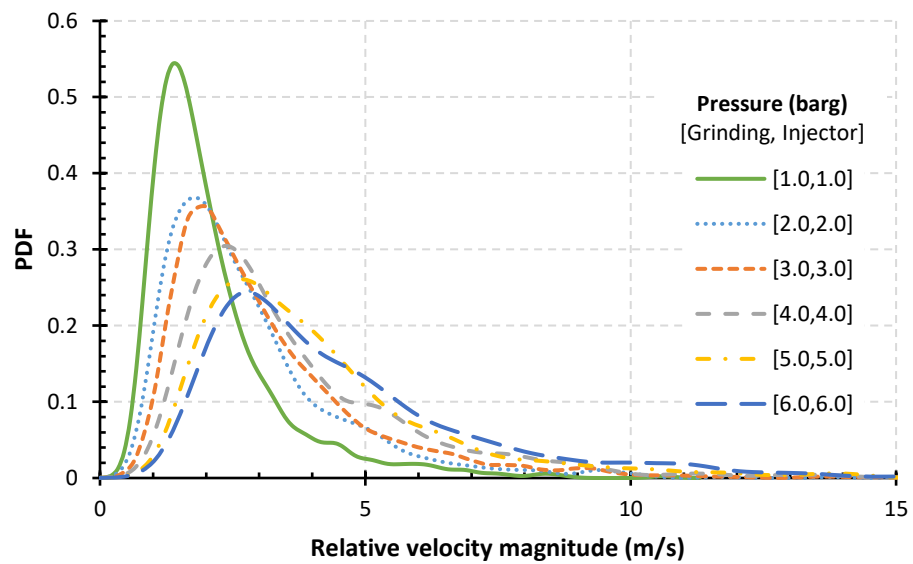
Figure 6.29: Relative velocity magnitude distribution of 5,000 particles at different grinding conditions
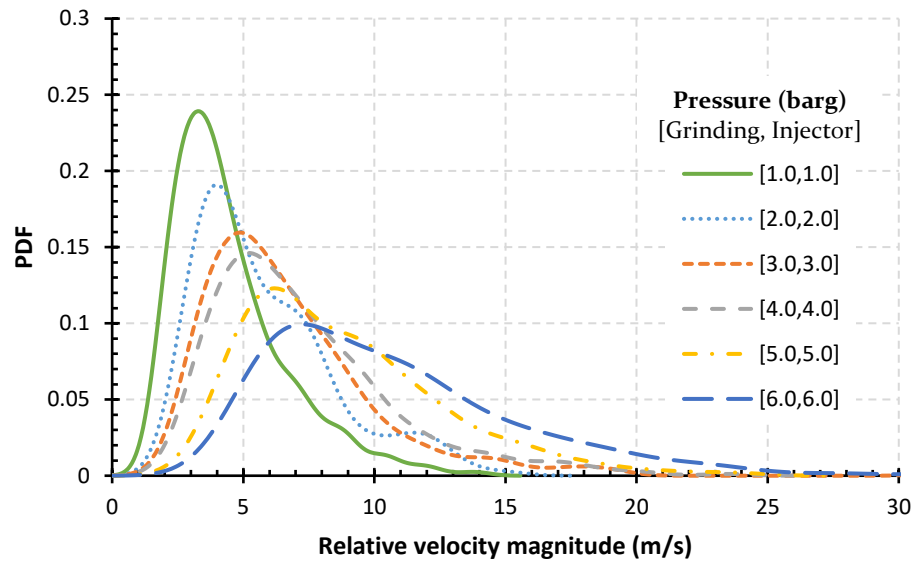
Figure 6.30: Relative velocity magnitude distribution of 2,500 particles at different grinding conditions

6.5.3.2   Effect of number of particles

At a given pressure, decreasing the number of particles leads to an increase in the particle velocity magnitudes, and their relative collisional velocities. The increase in the velocity magnitude of the particles when the number of particles is halved is generally low at all tested pressure conditions except when the number of particles decreases from 5,000 to 2,500 at a grinding and injector pressure of both 600 kPa (6.0 barg). This is illustrated in Figure 6.31. From Figure 6.32 it can be seen that the increase in relative collisional velocity is small when the number of particles is decreased from 20,000 to 10,000 and from 10,000 to 5,000, ranging from 0.5 to 0.9 m/s and 0.5 to 1.7 m/s, respectively. The increase is greater when reducing the number of particles from 5,000 to 2,500, ranging from around 2.0 – 4.5 m/s.
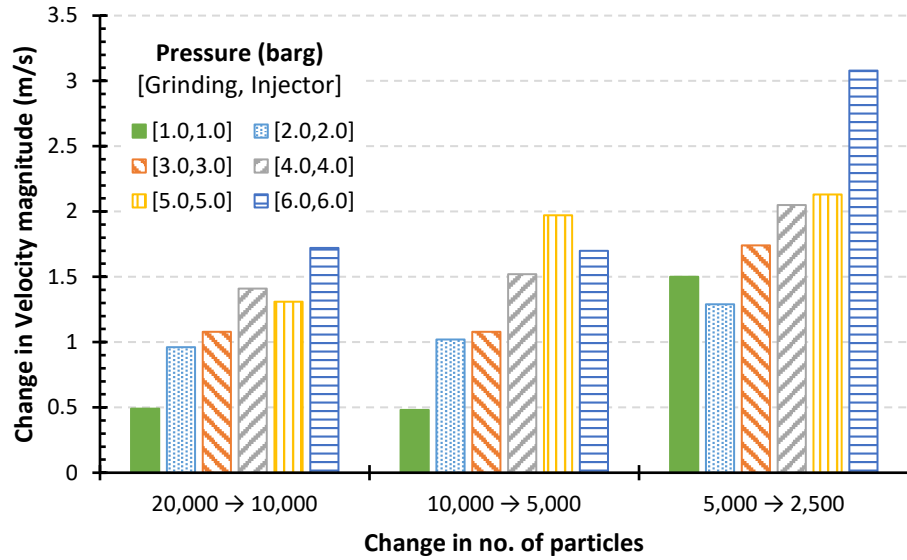
Figure 6.31: Increase in velocity magnitude with change in number of particles
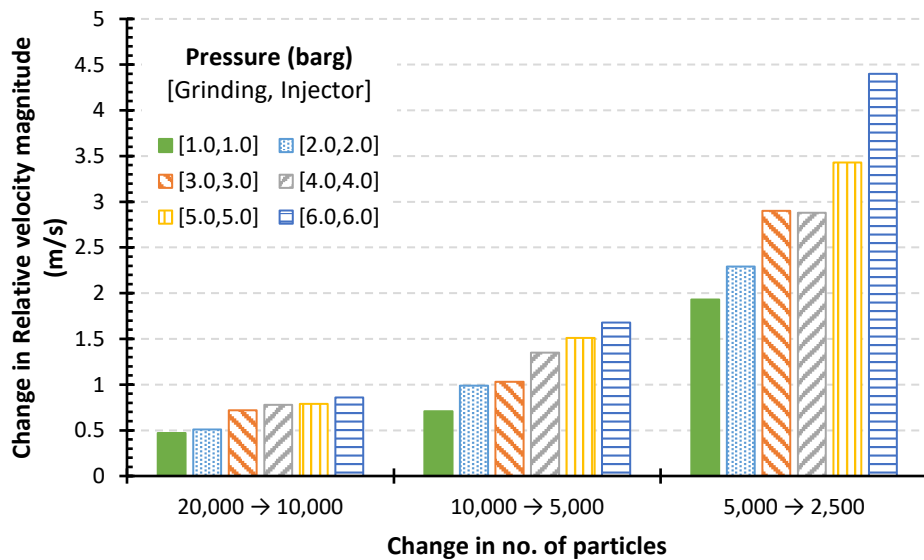
Figure 6.32: Increase in relative collisional velocity magnitude with change in number of particles

The relative collisional velocities and the collision frequency at different number of particles and grinding and injector nozzle pressures are shown in Table 6.14. The collision frequencies are the highest with 20,000 particles, however the relative collisional velocities are considerably small, and would potentially produce little to no breakage. As the number of particles decreases, the relative velocities increase while the collision frequencies decrease. Although the collision

frequencies decrease, the collisional velocities are increasing to values which may produce more considerable extents of breakage compared to the cases where the number of particles is large, and hence a higher breakage rate. Decreasing the number of particles further would lead to further decreases in collision frequency, and subsequently rate of breakage. This suggests there exists an optimum number of particles.

Table 6.14: The relative collisional velocities and collision frequency for different number of particles and grinding and injector nozzle pressures

		[1.0,1.0]	[2.0,2.0]	[3.0,3.0]	[4.0,4.0]	[5.0,5.0]	[6.0,6.0]
20,000	**Relative collisional velocity (m/s)**	0.19	0.29	0.25	0.3	0.37	0.36
	Collision frequency (s^{-1}) ($\times 10^8$)	187	226	255	261	273	280
10,000	**Relative collisional velocity (m/s)**	0.66	0.8	0.97	1.08	1.16	1.22
	Collision frequency (s^{-1}) ($\times 10^8$)	57.8	67.1	72.1	80.0	86.5	93.7
5,000	**Relative collisional velocity (m/s)**	1.37	1.79	2	2.43	2.67	2.9
	Collision frequency (s^{-1}) ($\times 10^8$)	17.1	21.9	23.8	25.8	27.0	28.3
2,500	**Relative collisional velocity (m/s)**	3.3	4.08	4.9	5.31	6.1	7.3
	Collision frequency (s^{-1}) ($\times 10^8$)	6.0	7.0	7.3	7.6	7.8	8.6

The CFD-DEM simulations are two-way coupled, and so the presence of the particles affects the fluid flow field. The particles hinder the gas flow, leading to a reduction in the gas velocity. Looking at the tangential velocity profiles of the grinding chamber when the grinding and injector pressure are each 1.0 bar (Figure 6.33), the tangential velocity can be seen to drop significantly, especially near the

outer wall of the chamber. This is also illustrated in the velocity contour plots in Figure 6.34. Larger concentrations of particles are seen to cause a greater decrease in the gas phase velocity in the chamber. This reduced gas phase velocity combined with the concentration of particles at the wall results in particles travelling around the grinding chamber with a low average velocity.
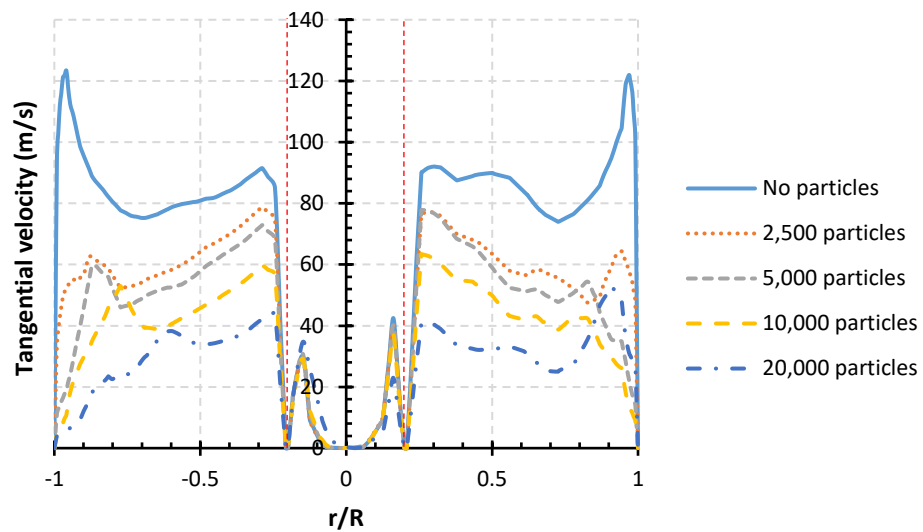
Figure 6.33: Instantaneous tangential velocity profile in the grinding chamber with a grinding and injector pressure of 1.0 bar each, and a different number of particles present in the chamber
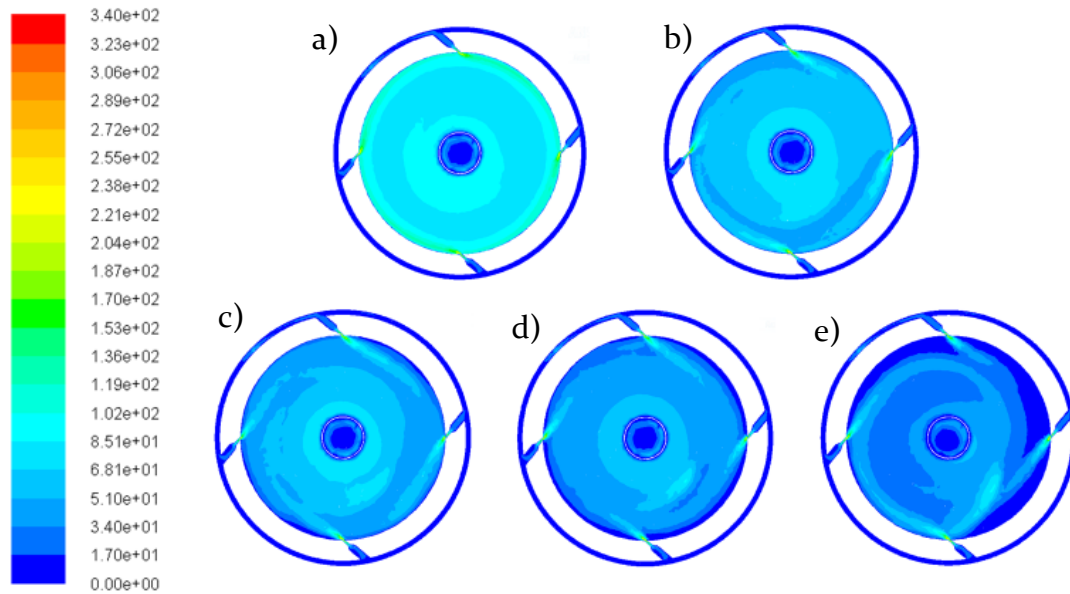
Figure 6.34: Velocity magnitude contours in the grinding chamber with a grinding and injector pressure of 1.0 bar each, with a) no particles; b) 2,500 particles; c) 5,000 particles; d) 10,000 particles; e) 20,000 particles

Analysis of the vectors of the velocity magnitude of the fluid gives a further indication of the effect of the particles on the fluid. Comparison of the fluid with no particles and with 2,500 particles shows there is a disturbance in the circular motion of the fluid near the wall, as can be seen in Figure 6.35. With 20,000 particles there is an even greater disturbance caused in the fluid flow than with 2,500 particles, shown in Figure 6.36. The large particle concentration causes a great hindrance to the fluid flow and creates a dead zone where a minimal amount of fluid can pass through.
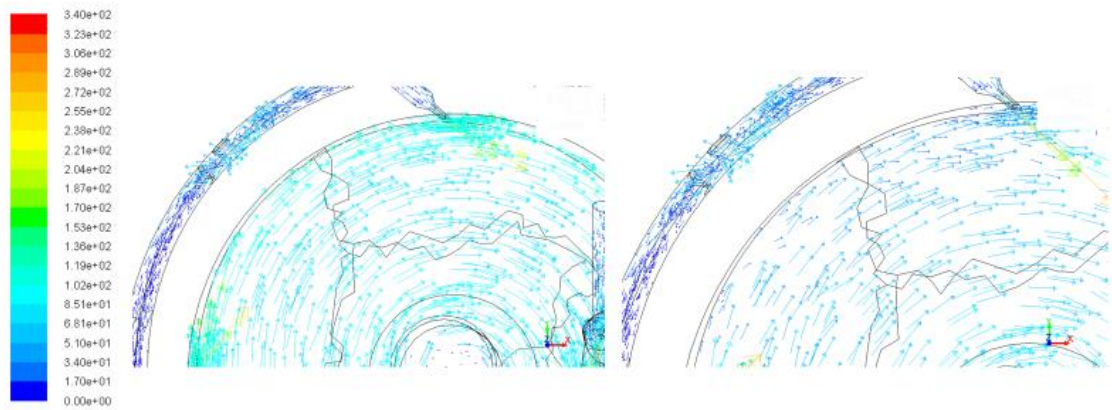
Figure 6.35: Vectors of fluid velocity magnitude in the grinding chamber with a grinding and injector pressure of 1.0 bar each (left: no particles | right: 2,500 particles)
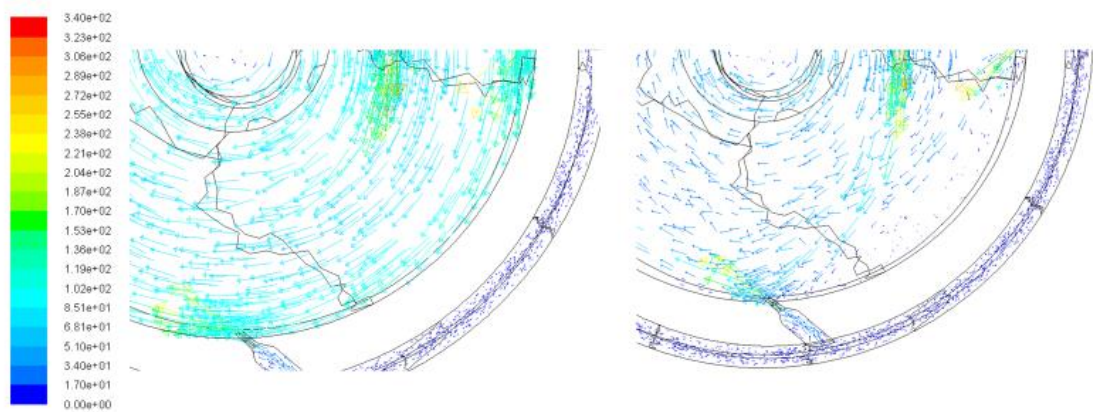
Figure 6.36: Vectors of fluid velocity magnitude in the grinding chamber with a grinding and injector pressure of 1.0 bar each (left: no particles | right: 20,000 particles)

At higher grinding and injector pressures of 6.0 bar each, the same effect on the tangential velocity with regards to the change in particle concentration can be seen, as illustrated in Figure 6.37 and Figure 6.38.
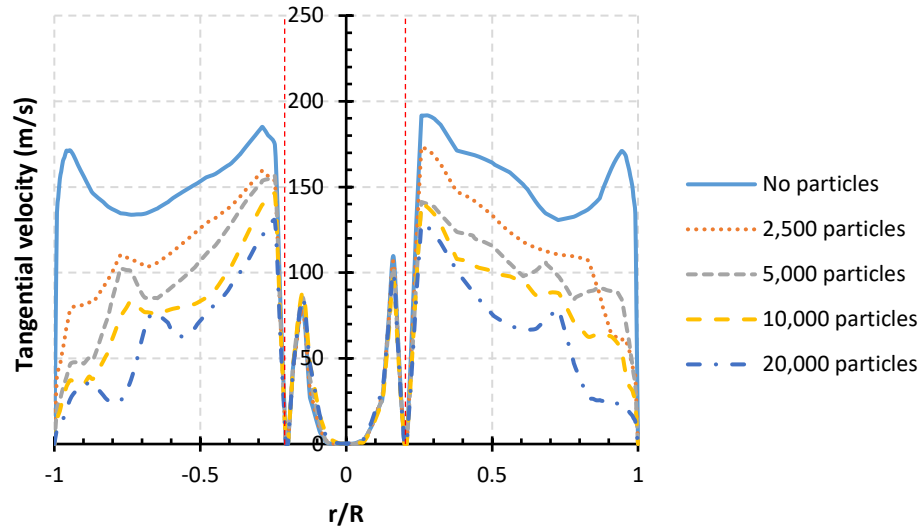
Figure 6.37: Instantaneous tangential velocity profile in the grinding chamber with a grinding and injector pressure of 6.0 bar each, and a different number of particles present in the chamber
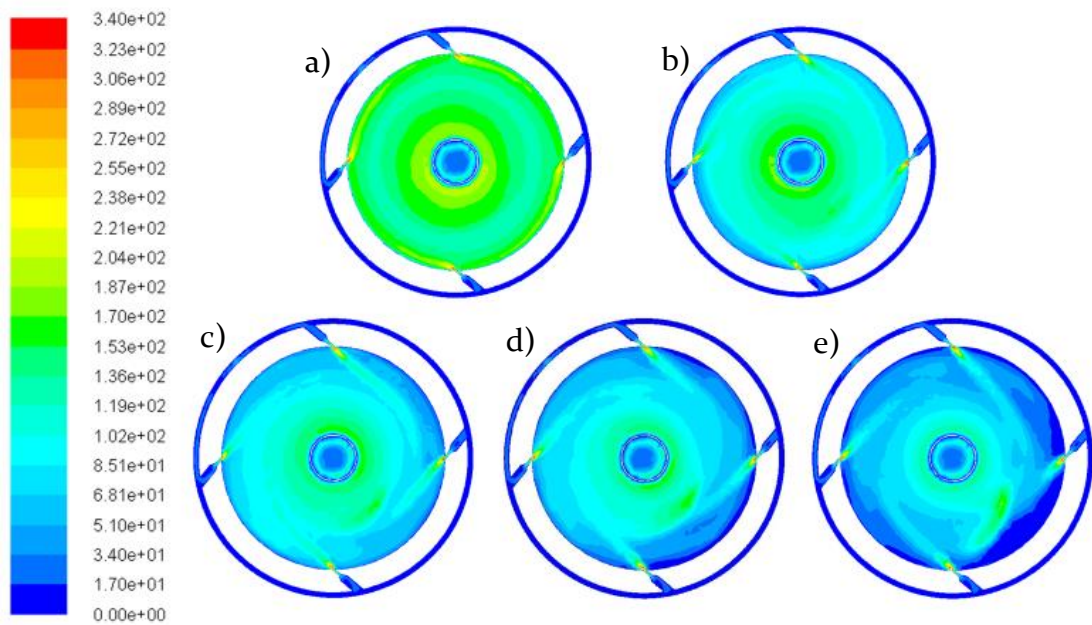
Figure 6.38: Velocity magnitude contours in the grinding chamber with a grinding and injector pressure of 6.0 bar each, with a) no particles; b) 2,500 particles; c) 5,000 particles; d) 10,000 particles; e) 20,000 particles

As with the case at the lower pressure of 1.0 bar, the presence of 2,500 and 20,000 particles both affect the motion of the fluid in the grinding chamber, shown in Figure 6.40 and Figure 6.41, respectively.
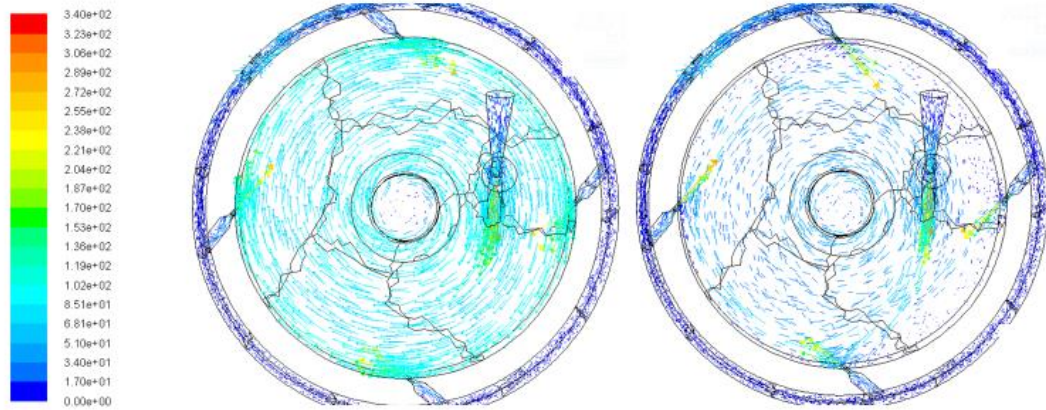
Figure 6.39: Vectors of fluid velocity magnitude in the grinding chamber with a grinding and injector pressure of 6.0 bar each (left: no particles | right: 2,500 particles)
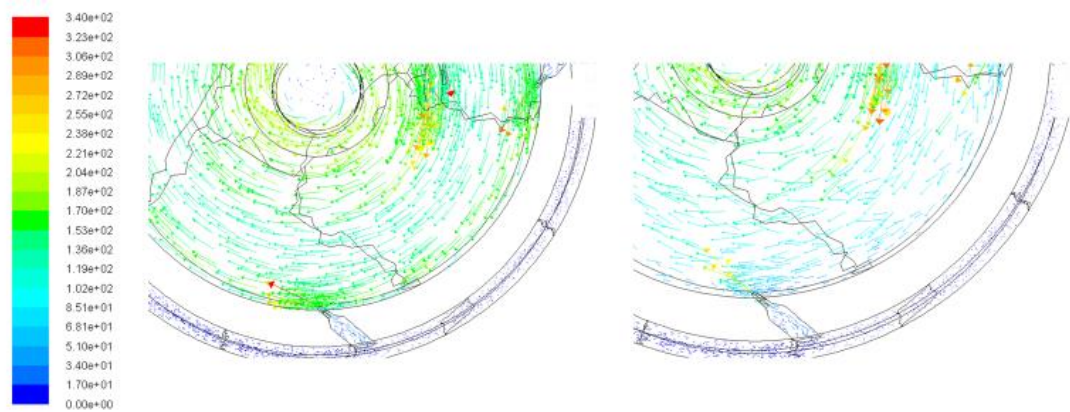
Figure 6.40: Vectors of fluid velocity magnitude in the grinding chamber with a grinding and injector pressure of 6.0 bar each (left: no particles | right: 2,500 particles)
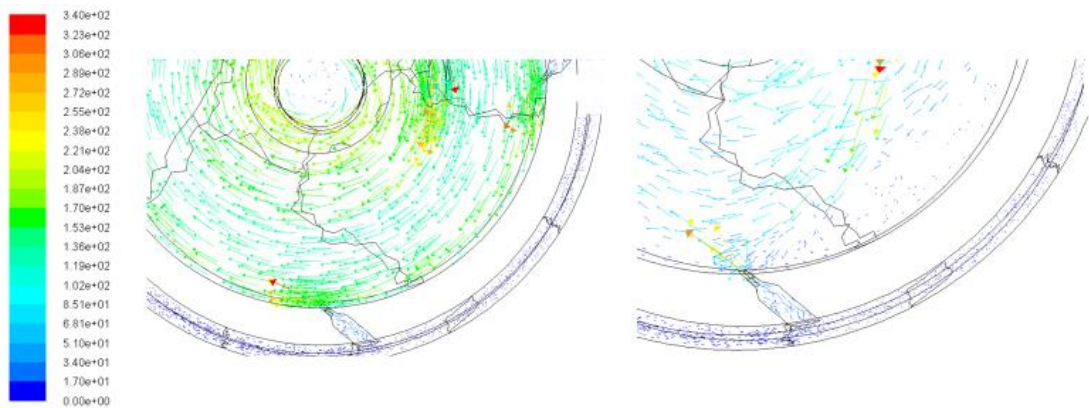
Figure 6.41: Vectors of fluid velocity magnitude in the grinding chamber with a grinding and injector pressure of 6.0 bar each (left: no particles | right: 20,000 particles)

The effect of the 425 μm particles on the fluid is a contrast to that of the finer

particles present in Case 2. From Figure 6.42 it can be seen that the tangential

velocity near the outer wall is insignificantly reduced with the presence of particles. Figure 6.21 also shows that the particles present in the chamber are travelling at much higher velocities compared to the particles in the Case 5 simulations. This highlights that there is less hindrance of the fluid and the particle acceleration.
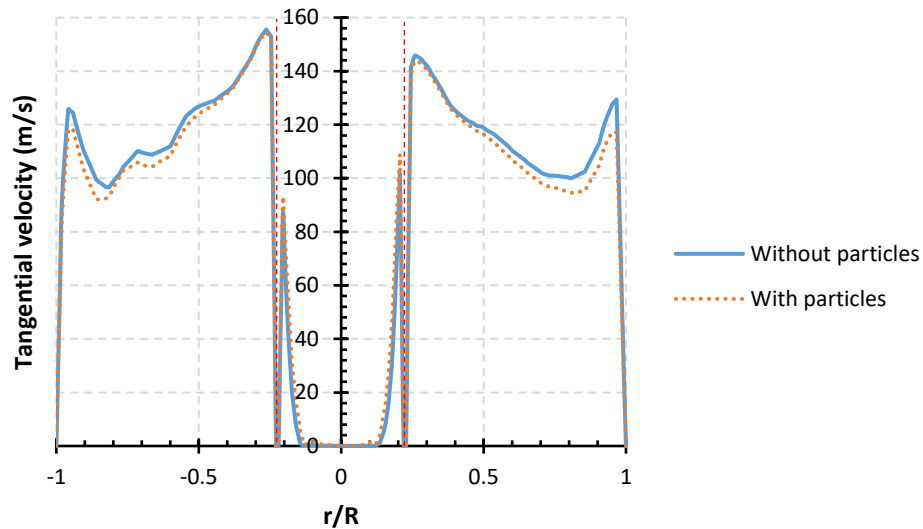
Figure 6.42: Instantaneous tangential velocity profile of case 2 with and without particles

Table 6.15 lists the volume fraction of the grinding chamber occupied by the four different particle concentrations simulated, as well as the mass of particles present. The volume fraction occupied by the 20,000 particles can be compared to the that of the jet milling experiments detailed in Section 5.4.1, in which a particle mass of 1.3 g was found to be present in the grinding chamber after steady state conditions had been reached.

Table 6.15: Volume fraction of particles in the grinding chamber

Number of particles	Volume fraction	Particle mass (g)
2,500	0.012	0.15
5,000	0.024	0.31
10,000	0.047	0.61
20,000	0.094	1.23

While the particle concentration with 20,000 particles can be compared in terms of mass to the milling experiment described in Chapter 5, there are some important differences to consider. In a typical milling experiment, the particle size present in the mill would change from the initial feed size to a particle size distribution which includes sizes smaller than the feed. Particles would also be escaping the mill. The individual particle and relative particle velocity magnitudes presented from these simulations are therefore most related to the initial conditions in the grinding chamber when the feed particles are present in the chamber. From the relative particle velocity data in the simulation, it may be possible to predict the likelihood of a particle undergoing breakage based on the single impact behaviour investigated in Chapter 4. Using the single impact rig allows for the minimum breakage velocity for a particle to be found, which can then be compared to the velocities seen in the simulations.

6.5.4 Stresses

The normal and shear stresses experienced by the particles was analysed at three different bin locations near the outer wall: before the nozzle, at the nozzle, and after the nozzle (shown in Figure 6.43). Each bin was five particle diameters in width and length, and the height was that of the chamber.
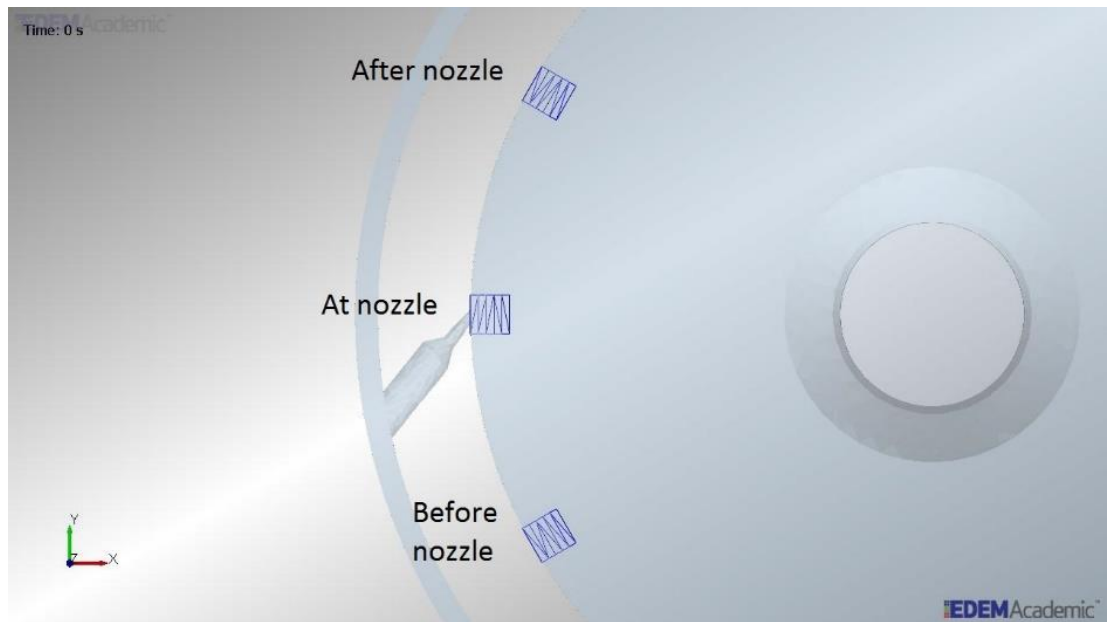
Figure 6.43: Location of cells

Each bin was divided into five sub-bins, with bin 1 being nearest the outer wall and bin 5 being furthest away, as illustrated in Figure 6.44.
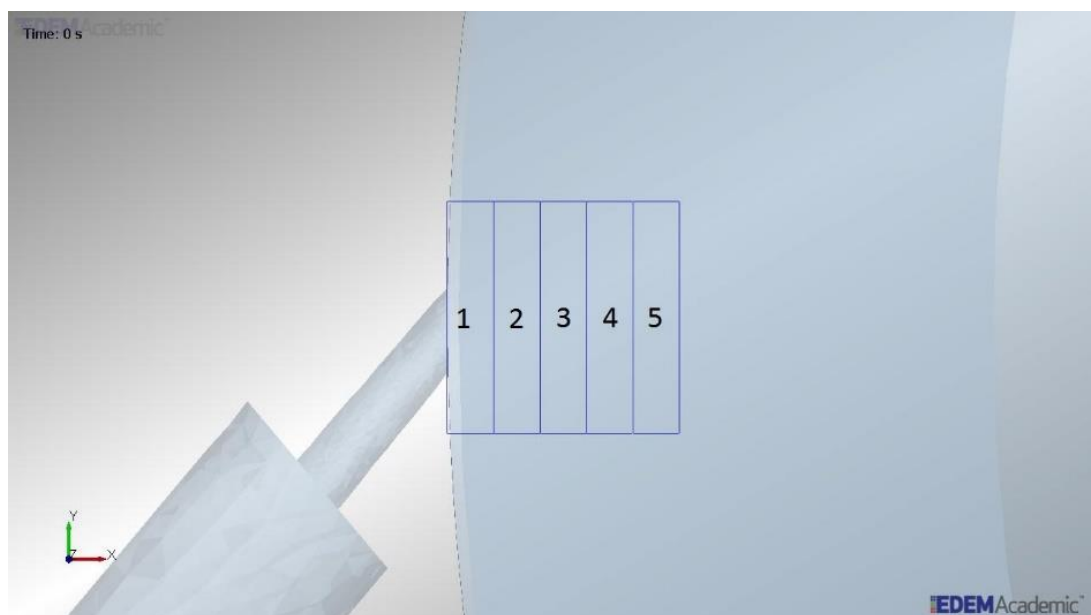
Figure 6.44: Bin divisions

The approach of Bagi (1996) for the evaluation of stress in a granular assembly is used for the stress calculations. The normal and shear stresses in each sub-bin are

estimated by considering the forces acting on all the particles whose centres lie within the sub-bin using the following equation:

$$\sigma_{ij} = \frac{1}{V_B} \Sigma_1^{N_B} \boldsymbol{F}_{ij} \cdot R_p \qquad (6.35)$$

where σ_{ij} is the *ij*-component of stress tensor, V_B is the volume of the bin, N_B is the number of particles in the bin, and $\boldsymbol{F}_{ij}$ is the force acting in the direction *i* on face *j* of the particle using Cartesian coordinates. The major, intermediate and minor principal stresses are calculated from the stress tensors, and are used to calculate the hydrostatic stress, σ_H, and deviatoric stress, τ_D. These stresses are taken as the normal and shear stress, respectively. They are calculated as follows:

$$\sigma_H = \frac{\sigma_{xx} + \sigma_{yy} + \sigma_{zz}}{3} \qquad (6.36)$$

$$\tau_D = \frac{\sqrt{\left(\sigma_{xx} - \sigma_{yy}\right)^2 + (\sigma_{xx} - \sigma_{zz})^2 + \left(\sigma_{yy} - \sigma_{zz}\right)^2}}{\sqrt{6}} \qquad (6.37)$$

The simulations in Case 5, the stresses were calculated as the average over a time period of 0.01 s when the fluid had reached steady state and fully developed, and the particles in the grinding chamber reached a constant average velocity magnitude.

Just before the nozzle, the normal and shear stresses experienced by the particles generally decrease as the distance from the wall increases, shown in Figure 6.45.
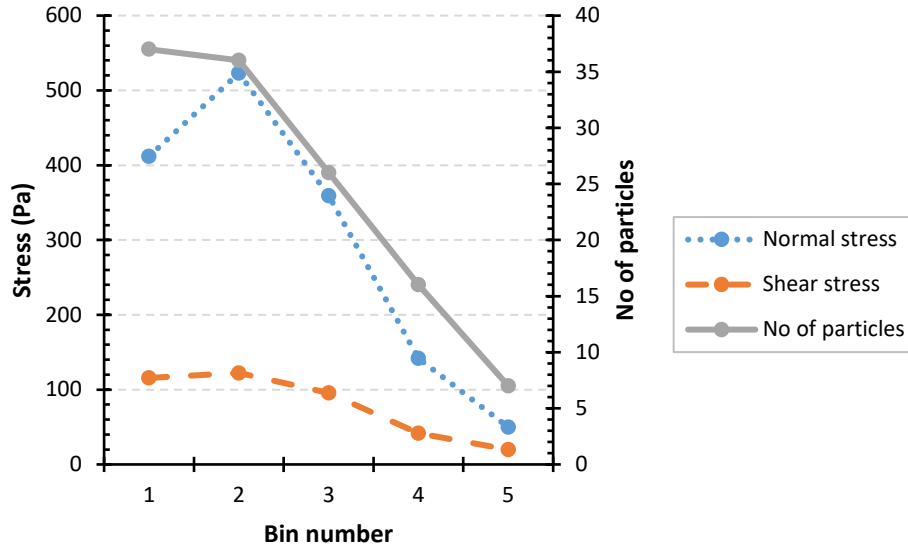
Figure 6.45: Normal and shear stress before nozzle with 10,000 particles and grinding and injector pressures of [1.0,1.0]

Increasing the grinding and injector gas pressures lead to an increase in the level of stress experienced by the particles, with the normal stress remaining higher than the shear stress as illustrated in Figure 6.46 where the nozzle gas pressures have been increased to [6.0,6.0].
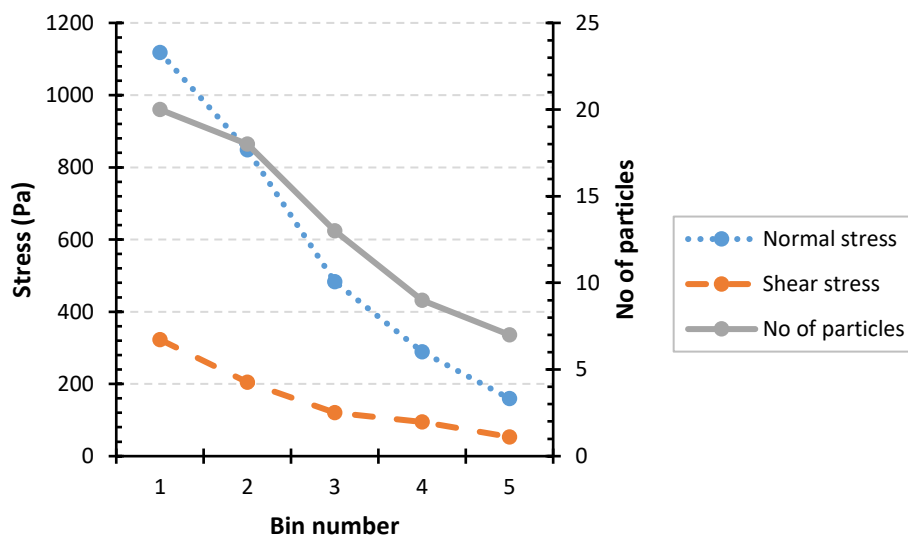
Figure 6.46: Normal and shear stress before nozzle with 10,000 particles and grinding and injector pressures of [6.0,6.0]

135

Reducing the number of particles to 2,500 results in a reduced level of normal and shear stress, as can be seen comparing Figures 6.28 and 6.30. As with the case of 10,000 particles, the normal and shear stresses also increase with the gas pressure (Figure 6.48).
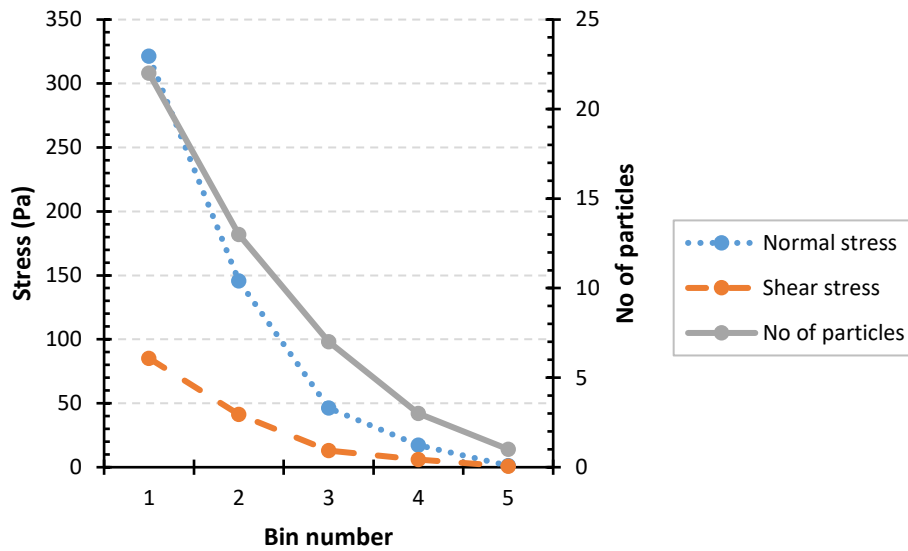
Figure 6.47: Normal and shear stress before nozzle with 2,500 particles and grinding and injector pressures of [1.0,1.0]
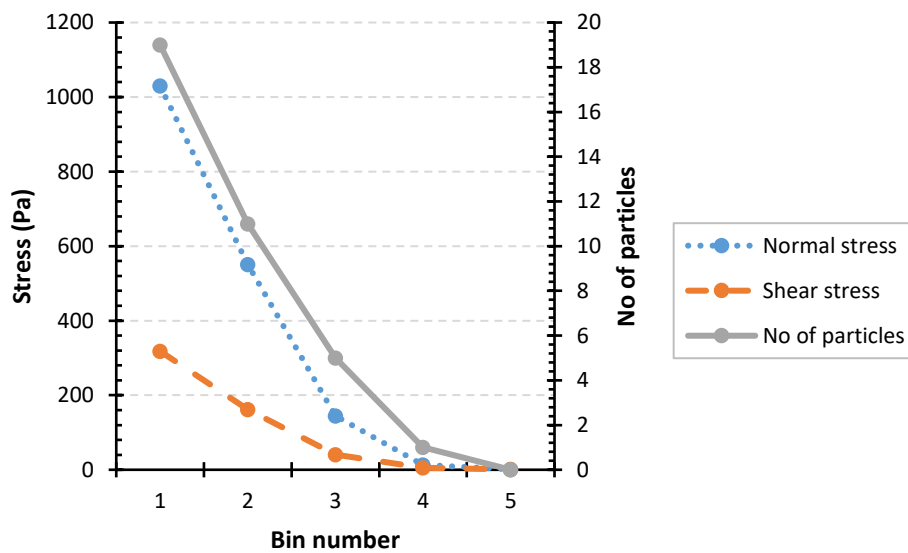
Figure 6.48: Normal and shear stress before nozzle with 2,500 particles and grinding and injector pressures of [6.0,6.0]

In the area directly in front of the nozzle, the stresses experienced by the particles also increase with the nozzle pressure. The normal stress is larger than the shear stress close to the wall, with the difference between the two decreasing as distance from the outer wall increases. This can be seen in Figure 6.49.
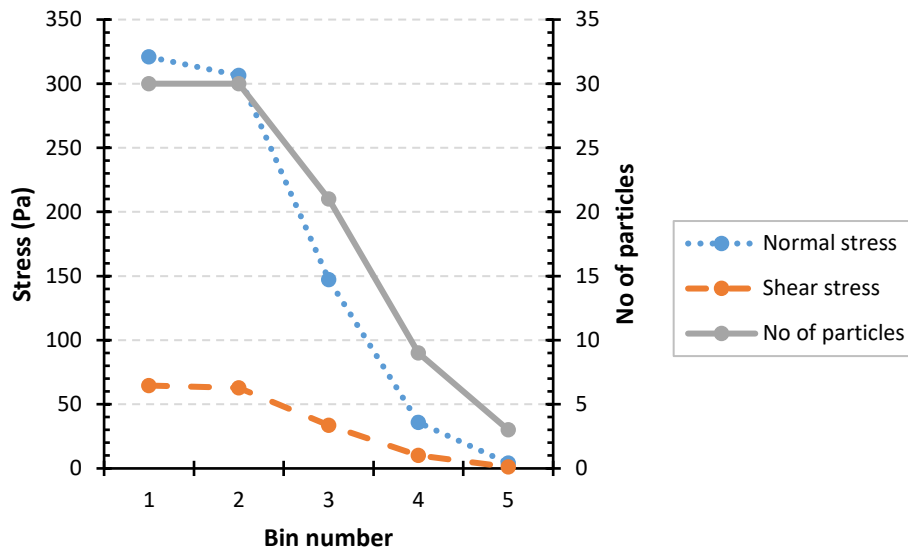
Figure 6.49: Normal and shear stress at the nozzle with 10,000 particles and grinding and injector pressures of [1.0,1.0]

As the number of particles decreases, there is a significant change in the stresses with relation to the distance from the outer wall. There is huge drop in the normal stress from bin 1 to 3, as seen in Figure 6.50.
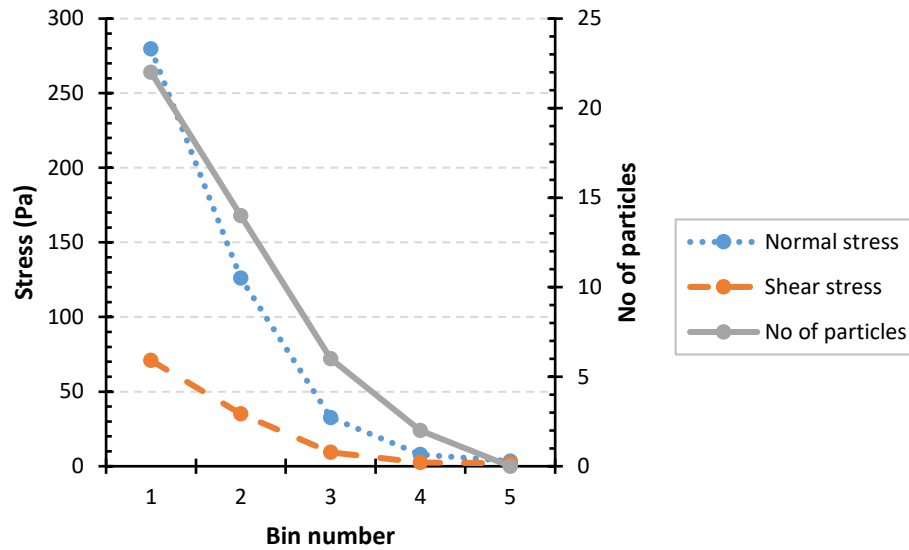
Figure 6.50: Normal and shear stress at the nozzle with 2,500 particles and grinding and injector pressures of [1.0,1.0]

Stresses were found to generally be the highest before the nozzle compared to at the nozzle and after the nozzle. This is due to there being a larger number of particles present near the wall before the nozzle, and so they undergo many inter-particle collisions which leads to a large level of stresses. At the nozzle, the gas jet propels several particles away from the wall, illustrated in Figure 6.51. There will therefore be less inter-particle collisions at this location and directly after the nozzle.
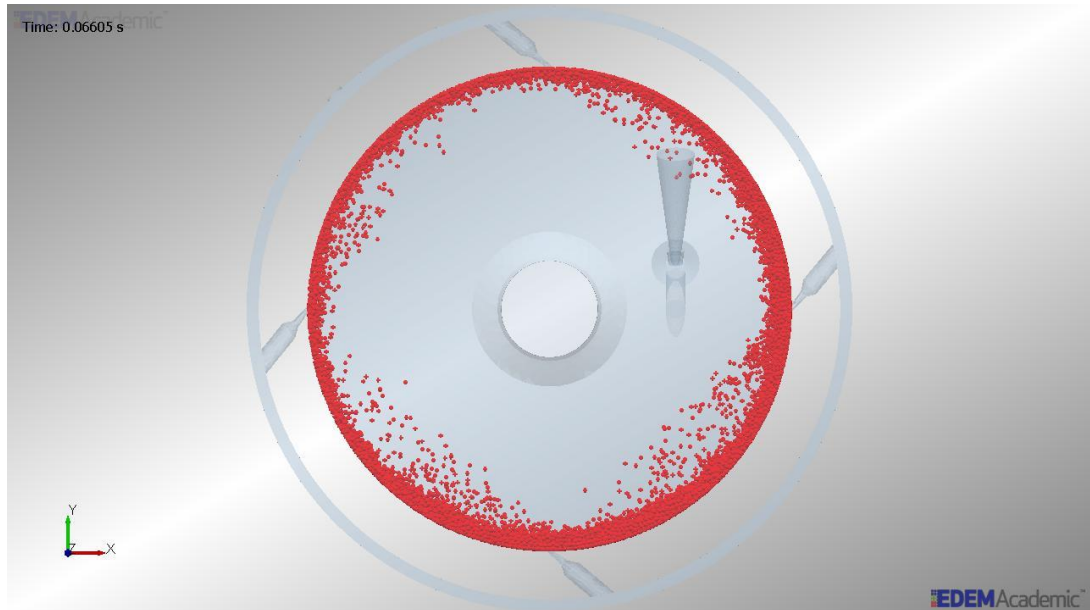
Figure 6.51: Particle propulsion in the grinding chamber

The stresses at and after the nozzle were found to be comparable at the majority of the tested conditions.

Analysis of the contact between the particles has found that the vast majority of the particles do not maintain any contacts while in the grinding chamber. When the number of particles is 20,000, there are on average only 3-5 contacts between any of the particles present in the cells before, after and at the nozzle, as shown in Figure 6.52. This small ratio of contacts to particles is unaffected by the number of particles in the chamber or the grinding nozzle pressures, which can be seen by the comparison of Figures 6.35 – 6.38. The implication of this is that stresses experienced by the particles are a result of instantaneous interparticle collisions, even when particles move in a bulk. The shear stress is a result of glancing interparticle collisions rather than the movement of particle layers past each other.
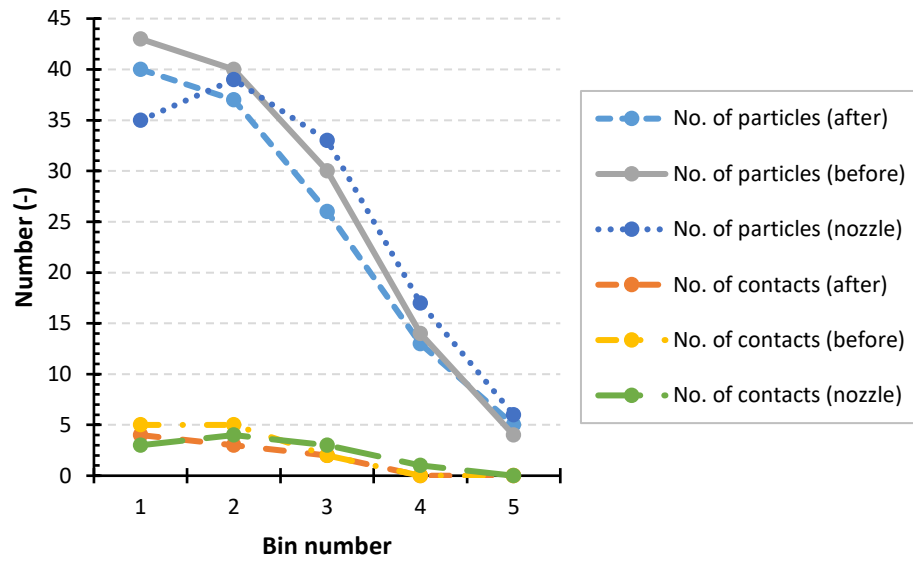
Figure 6.52: Number of particles and contacts with 20,000 particles and grinding and injector pressures of [1.0,1.0]
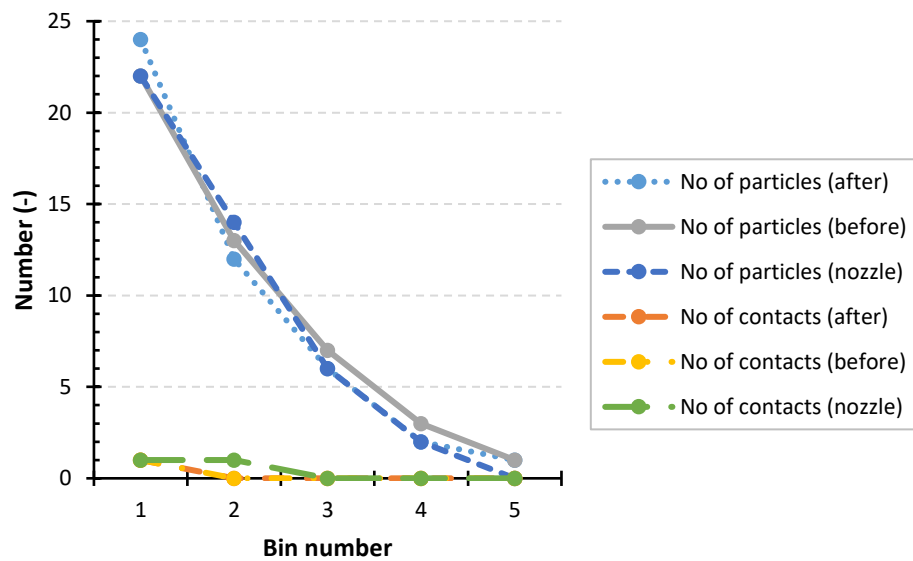
Figure 6.53: Number of particles and contacts with 2,500 particles and grinding and injector pressures of [1.0,1.0]
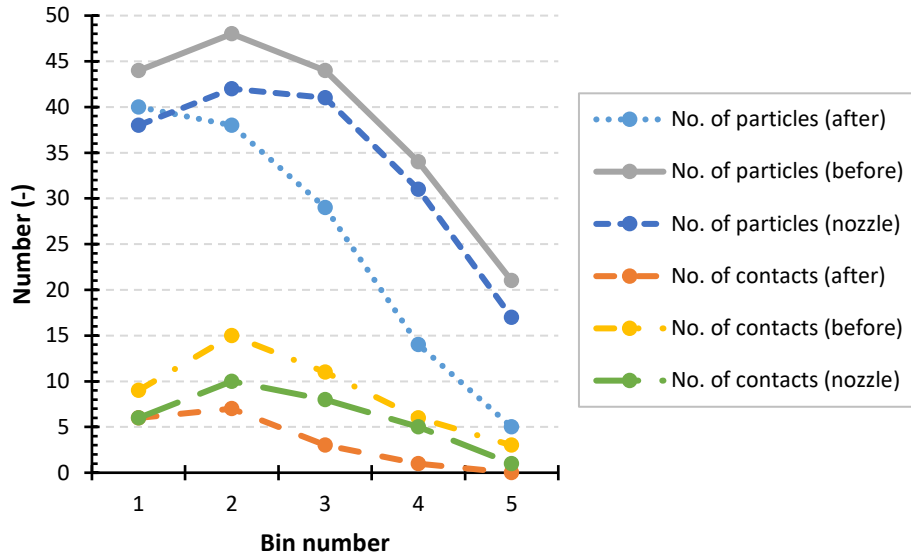
Figure 6.54: Number of particles and contacts with 20,000 particles and grinding and injector pressures of [6.0,6.0]
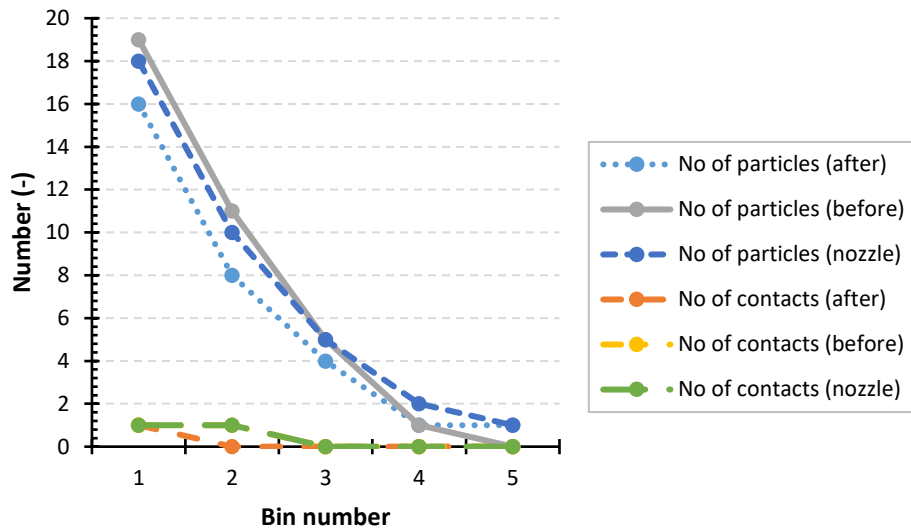
Figure 6.55: Number of particles and contacts with 2,500 particles and grinding and injector pressures of [6.0,6.0]

The same can be seen with the 10^6 particle simulation from Section 6.5.2 above (Case 4). At 12 evenly spaced locations at the outer wall (Figure 6.56), the number of contacts was found to be much lower than the number of particles, as shown in Figure 6.57.

141
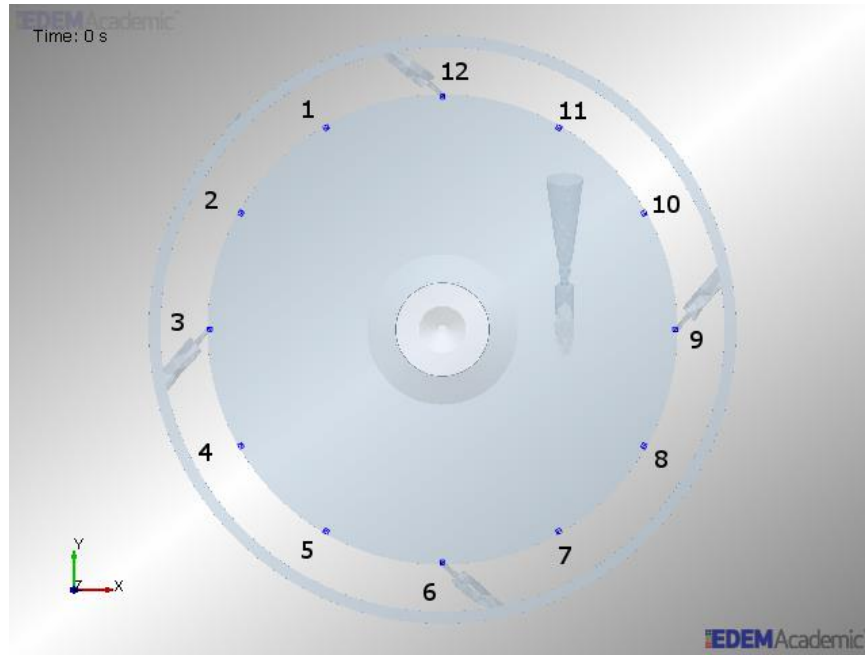
Figure 6.56: The locations of the 12 bins analysed for the number of particles and particle contacts in the simulation with 10^6 particles
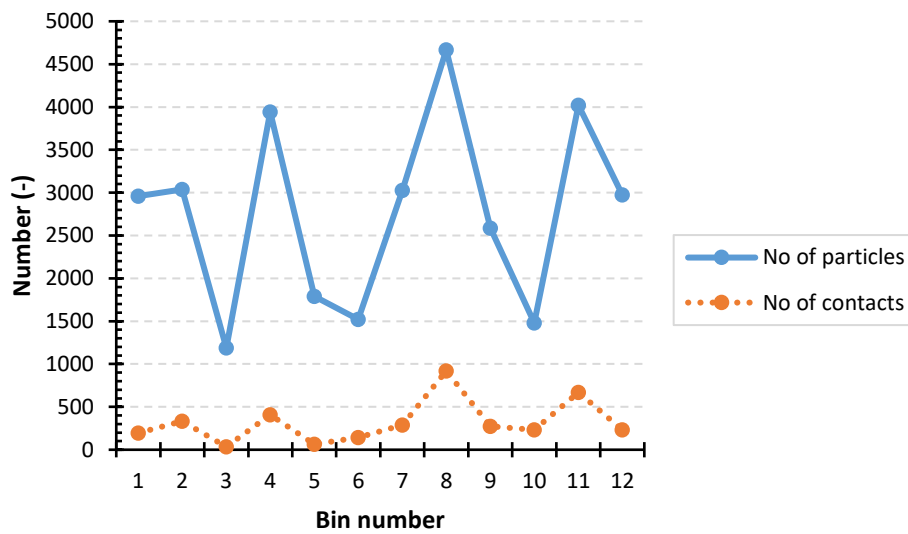
Figure 6.57: Number of particles and contacts with 10^6 particles

6.6   Conclusions

CFD alone, as well as CFD two-way coupled with DEM have shed light on the behaviour of the spiral jet mill. The CFD turbulence model was validated based on the volumetric flow rate and found to correlate well with experimental results. The centrifugal and drag forces alone were found to only classify particles up to 2 µm

in the Hosokawa Alpine Aeroplex Spiral Jet Mill 50AS. The loading of particles is necessary to move particles closer to the central outlet for them to escape. This effect could not be simulated using coupled CFD-DEM to limitations owing to the small particle size and large number of particles required. The simulation of this would be both lengthy and computationally expensive.

Inter-particle collisions were found to have a greater amount of dissipated energy than particle-wall collisions. This suggests that inter-particle collisions contribute more to particle breakage in the spiral jet mill. There may also be the existence of an optimum size ratio in regards to particle breakage; collisions between 10 and 20 µm particles have the highest frequency and level of dissipated energy per collision. The number of each type of these collisions changes with the number of particles in the system, with the share of inter-particle collisions in terms of both number and energy transfer growing as the number of particles increases.

Increasing the nozzle gas pressure led to an increase in the particle velocity and the velocity distribution, as did decreasing the number of particles. However, it was noted that at higher pressures, decreasing the number of particles from 5,000 to 2,500 led to a small increase in particle velocity, suggesting that using a lower number of particles was not economically viable. Decreasing the number of particles also led to a decrease in the collision frequency. It implies the existence of an optimum number of particles.

The stress exerted on particles was found to decrease as the distance from the outer wall increased. The stress before the nozzle was found to be greater than at and after the nozzle, due to particles being blown away from the wall by the nozzle jet.

Despite particles being in very close proximity and appearing to move as a bulk, there were found to be a very low number of contacts between particles in relation to the number of particles present. This combined with the fact that the major stress component experienced by the particles was normal compared to shear implies that particle breakage in the spiral jet mill is due mainly to instantaneous collisions between particles, rather than shearing of particle layers over each other through enduring contacts.

Chapter 7 Scale-up Studies

7.1   Introduction

The spiral jet mill comes in various different scales, ranging from lab-scale mills with diameters as small as 33 mm, to much larger industry scale mills. Using small scale mills helps to give an idea of how a material may reduce in size in a larger industrial setting, without the need of large quantities of material. However, the milling result from a small scale mill is not directly transferable to the behaviour of a larger mill. The change in geometry dimensions and the volume of the grinding chamber means there will be a differing degree of interparticle and particle-wall energy transfer. As the scale chamber size is changed, so usually is the cross sectional area of the nozzles. The fluid power input would therefore be different.

There are several potential avenues for scaling up the spiral jet mill. One criterion is the fluid power input to the system through the grinding nozzles. The milled product median size of particles in the spiral jet mill is inversely related to the grinding pressure (Ramanujam and Venkateswarlu, 1969), and hence to the fluid power input. The energy from the fluid is transferred to the particles, leading to high energy particle-particle and particle-wall collisions. This results in the breakage of the particles. The benefit of this criterion is that it is possible to measure the air mass flow rate by the use of coriolis flow meters and calculate the fluid power input. However, it is not possible to determine how much of the supplied energy is actually utilised in particle breakage.

Scale-up can potentially be investigated by using the interparticle collisional energy. The extent of particle breakage is dependent on the impact velocity, and thus the energy of collision. In theory, if particles with the same mechanical properties collided with the same amount of energy in different sized mills, they will break to the same extent. The energy of collision is a function of the fluid power input, the particle concentration in the grinding chamber, and the particle size and density. Therefore if the relationship between these parameters for a given mill is established, the conditions required to achieve the same energy of collision in different mills can be identified. The energy of collisions in the mill cannot be measured; the degree of energy transfer in the mill can only be investigated by the use of simulations.

Another possible scale up criterion is the tangential velocity of the particles in the mill. A high tangential velocity suggests a high impact velocity of colliding particles, meaning they will collide with a larger amount of energy. As with the energy of collision, if the particle tangential velocity is the same for a given material in different mills, it should break to the same extent.

In this chapter, the potential for scale-up of the spiral jet mill based on fluid power input is investigated using four different jet mills: Hosokawa Alpine Aeroplex Spiral Jet Mill 50AS, Piconizer®, 2 inch Micronizer®, and 4 inch Micronizer®. The mills are operated under grinding conditions which result in the same fluid power input to the grinding chamber, and the specific surface area of the milled product calculated from the particle size distribution, measured by laser diffraction using the Malvern Mastersizer 2000S.

7.2 Review of Spiral Jet Mill Scale-up

There has been very little research work on the scale-up of the spiral jet mill. Müller et al. (1996) equated the centrifugal force to the drag force and showed that the cut size of the product of the spiral jet mill is dependent on the mill geometry and the tangential velocity of the solid-gas mixture at the outlet:

$$d_{cut} = 3.37 \left(\frac{v_t}{v_r d}\right)^{3/8} \left(\frac{\rho_F}{\rho_p}\right)^{5/8} \left(\frac{v_r}{v_t}\right)^{5/4} d_o \tag{7.1}$$

$$v_r = \frac{Q}{\pi d_o h_1} \tag{7.2}$$

where d_{cut} is the particle cut size diameter, d_o is the diameter of the outlet, Q is volumetric air flow rate, and h_1 is the height of the central outlet (the elevation of the central outlet opening above the base of the grinding chamber). They used dimensional analysis and derived a parameter to describe the grinding conditions of a mill, K:

$$K = \beta^{0.5} \frac{P d_c^4 \rho_s}{\dot{m}_F} \tag{7.3}$$

where $\dot{m}_F$ is the gas mass throughput, d_c is the diameter of the milling chamber, β is the load mass throughput of solids in relation to gas mass throughput. Figure 7.1 shows the relationship between the gas tangential velocity and K when material is present in the grinding chamber, and can be used to determine the required K value to achieve a specific tangential velocity, which is used in Eq. 7.1 to find the particle cut size. Eight different materials including limestone were fed into four different sized mills: 80, 170, 450 and 800 mm diameter. The 170 mm mill has grinding nozzles with a diameter of 1.5 mm, however the number of grinding nozzles used in this investigation is not stated, although it is said the mill can be

configured with 8 – 10 nozzles. No other structural information was provided for any of the mills. From Eq. 7.1 the particle cut size is a function of the tangential velocity. This method, however, is not very straightforward, requiring the knowledge of various mill parameters to determine the value of K. This method also does not relate the milling conditions to the degree of size reduction of a material in the mill, but rather to the air velocity in the chamber which alone does not demonstrate the milling performance. This rather tells what size of material will escape from the mill under specified conditions.
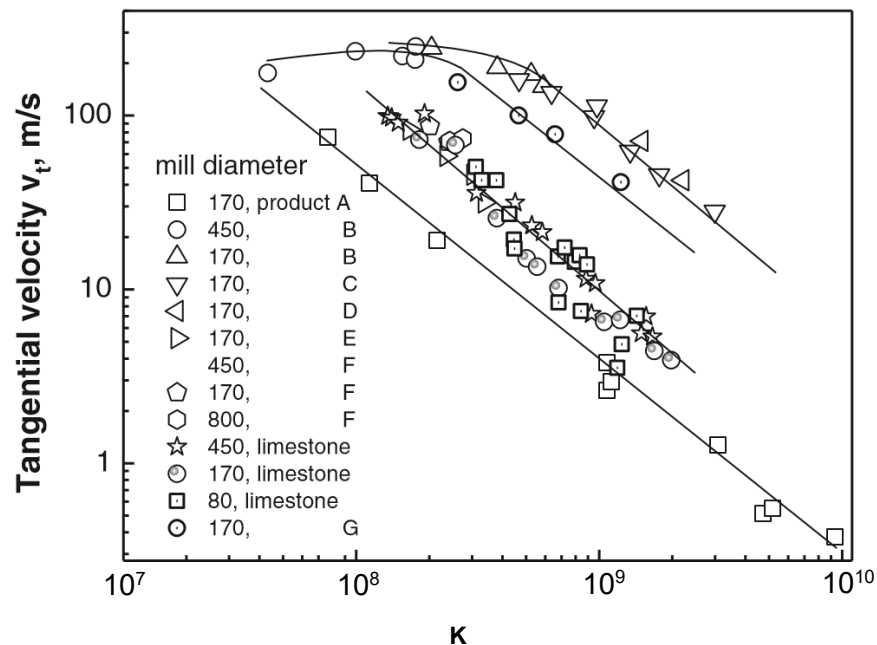
Figure 7.1: Relationship between tangential velocity at the jet mill outlet and the dimensionless number K
(Müller et al., 1996)

Midoux et al. (1999) investigated the jet milling of pharmaceutical powders using three different sized jet mills: 2 inch (6 grinding nozzles, 0.85 mm nozzle diameter), 4 inch (6 grinding nozzles, 1.25 mm nozzle diameter), and 8 inch (12 grinding nozzles, 1.00 mm nozzle diameter). They milled an unidentified powder and showed that the general relationship between the Specific Energy Consumption, E_{sp}, and the change in specific surface area of the milled material in

different sized mills fall in line with each other apart from at the lowest values of E_{sp} in the 4 inch mill, as can be seen in Figure 7.2. E_{sp} is the ratio of supplied kinetic energy to the solid feed rate. The kinetic energy was calculated as the product of the grinding gas mass flow rate and the sonic velocity. The change in specific surface area of the milled product, ΔSSA, was found to increase with E_{sp}.
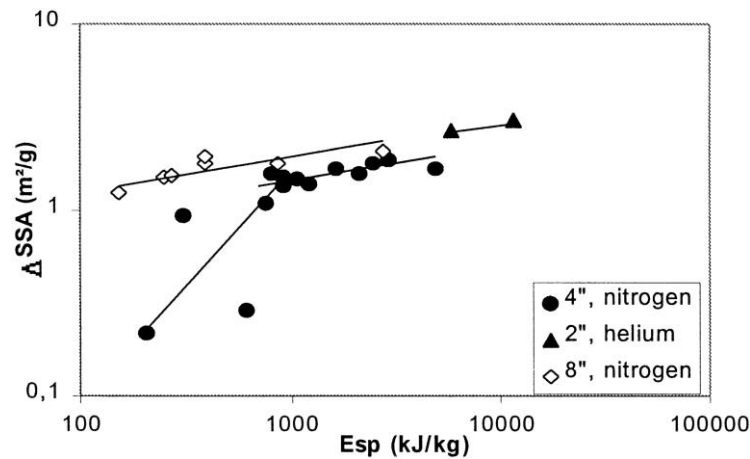
Figure 7.2: ΔSSA of product as a function of E_{sp} (Midoux et al., 1999)

Midoux et al. (1999) also investigated the relationship between grinding pressure and SSA using two different sized mills and the same unidentified material fed at high feed rates. By using different solid feed rates for the two different mills, they found it possible to achieve similar behaviour in the change in SSA with grinding pressure. However, grinding pressure alone is not a reliable parameter for scale-up. The grinding pressure will drop before the gas reaches the grinding nozzles of the mill, and the amount of pressure drop is likely to be different for each mill setup. The size of the grinding nozzles also affect how much fluid power is input to the grinding chamber, which is not taken into account when looking at grinding pressure.
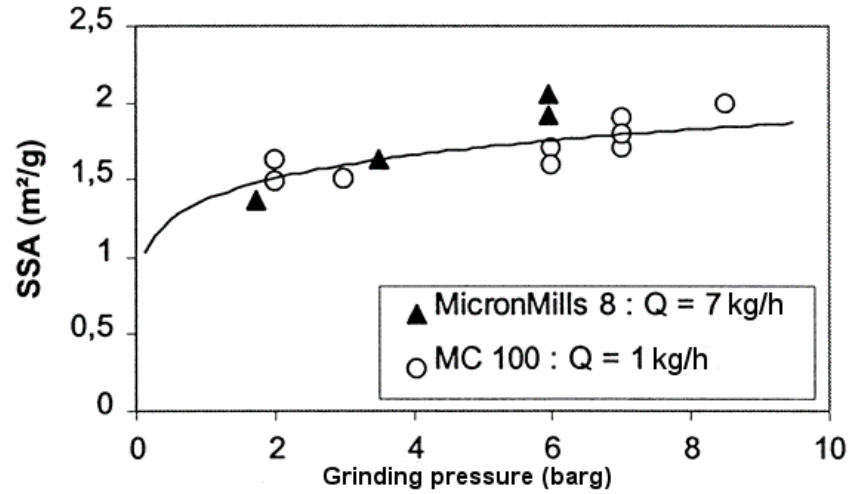
Figure 7.3: SSA of product as a function of grinding pressure (Midoux et al., 1999)

MacDonald et al. (2016) derived an equation (Eq. 7.4) for the cut size of particles in a spiral jet mill based on grinding as well as gas thermodynamic properties, and suggested that it may be used for scale-up.

$$d_{cut} = \left(\frac{h_2}{h_1}\right)^2 \left(\frac{C_2}{k_3^2} + \frac{x_1 k_4}{k_3^2 d_{Reynolds} \dot{m}_F} + \frac{C_2 \dot{m}_p}{k_3^2 x_2} + \frac{x_1}{k_3^2 d_{Reynolds} x_2} \frac{1}{E_{sp}}\right) \tag{7.4}$$

$$C_2 = \frac{3 C_1 \rho_F r}{4 \rho_p} \tag{7.5}$$

$$k_3 = \frac{v_t}{v_r} \tag{7.6}$$

$$k_4 = \frac{2}{v_{sonic}^2} \tag{7.7}$$

$$x_1 = \frac{18 \mu h_1 r}{\rho_p k_2} \tag{7.8}$$

$$x_2 = \frac{C_M \zeta P M_w}{RT} \tag{7.9}$$

where h_2 is the height of the grinding chamber, $d_{Reynolds}$ is the length scale of particles at the grinding chamber exit, $\dot{m}_p$ is the solids feed rate, E_{sp} specific energy consumption, C_1 is the drag coefficient as the Reynolds number tends towards infinity, r is the radial position from the centre of the grinding chamber, v_t is the

particle tangential velocity, v_{sonic} is the gas sonic velocity, C_M is mass transfer coefficient, ζ is the time averaged mass fraction of collision fragments below the cut size, M_w is the gas molecular weight, R is the universal gas constant, T is the gas temperature.

MacDonald et al. (2016) verified the equation with experiments by investigating the relationship between the d_{90} of milled material and $1/E_{sp}$, where the solid feed rate was varied and the gas mass flow rate kept constant, and vice versa. They showed linear relationships between d_{90} and $1/E_{sp}$, which is expected based on Eq. 7.4. However, in some cases there were not enough data points for this relationship to be considered true. They also removed data points which they considered to be outliers. They suggest a linear relationship between $(h_2/h_1)^2$ and the particle cut size, although not enough data points were collected for this statement to be considered valid. The equation was able to produce the same trends of the experimental results of previous researchers (Midoux et al., 1999; Zhao and Schurr, 2002). MacDonald et al. have only carried out work using a single mill geometry and the equation has not been tested for scale-up.

7.2.1 Summary

The scaling of the spiral jet mill is a topic which has not been investigated much; very little literature was found on the subject. The work which has been carried out has considered the importance of the drag and centrifugal forces present within the grinding chamber, which are functions of the grinding pressure or fluid power. However, the work carried out so far has either not investigated scale-up in terms of a characteristic parameter of a milled material, or has not used a scale-up criterion which is easily transferrable between different milling geometries.

There were some analyses of the effect of fluid power on the milling performance for different sized mills, which is a more adequate way of investigating scale-up. By developing a relationship between a characteristic milling parameter of the spiral jet mill such as the fluid power input, and the resultant product size, a more straightforward scale-up behaviour can be analysed. This relationship would be universal for all types of spiral jet mill regardless of the mill physical parameters and is addressed below.

7.3   Method of Spiral Jet Mill Scale-up Investigation Based on Gas Input Power

7.3.1   Details of Spiral Jet Mills

Scale-up was investigated using four different mills: the Hosokawa Alpine Aeroplex Spiral Jet Mill 50AS described in Chapter 5 (Hosokawa Micron Ltd, UK), Hosokawa Alpine Piconizer® module (part of the Picoline range), a 2 inch Micronizer®, and a 4 inch Micronizer® (both constructed by Sturtevant Inc, USA). Experiments with all mills except the Hosokawa Alpine Aeroplex Spiral Jet Mill 50AS were carried out at the AstraZeneca research and development site, located in Macclesfield, UK. α-lactose monohydrate was used as the test material.

7.3.1.1   Piconizer®

The Piconizer® is the spiral jet milling module of the Hosokawa Alpine Picoline range, shown in Figure 7.4. Figure 7.5 gives a closer look at the grinding chamber. It is a 33 mm diameter spiral jet mill with four grinding nozzles, each 0.5 mm in diameter. They are angled at 50° with respect to the normal to the wall. The injector nozzle has a diameter of 1.5 mm. The height of the grinding chamber is 45 mm. The diameter of the central outlet is 7 mm. The outlet of the grinding

chamber is connected to a combined cyclone filter, which separates the milled product from the grinding air, and collects the product in a glass jar. The compressed nitrogen gas system at Astrazeneca only allowed a maximum pressure of 7 bar to be used with the Picoline.

Figure 7.4: Hosokawa Alpine Picoline with Piconizer attached
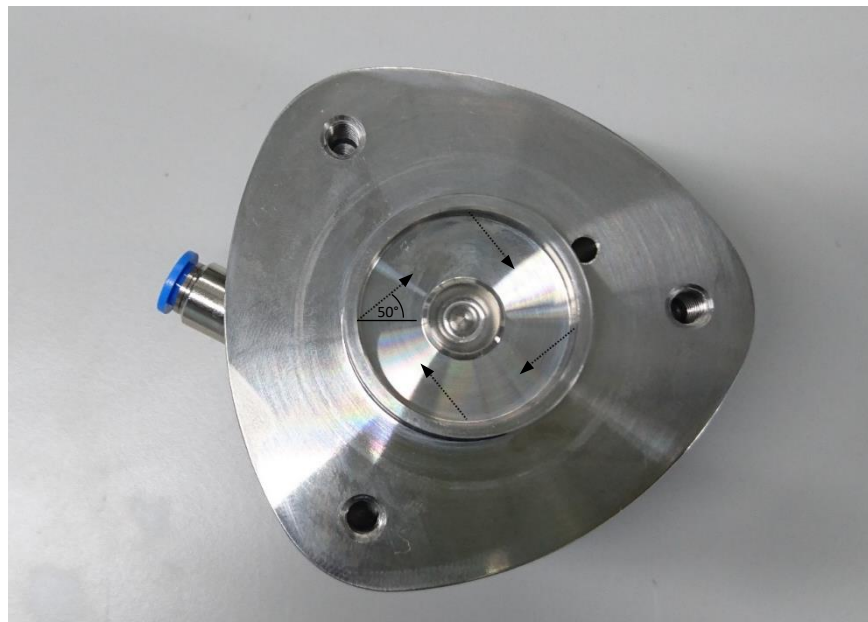
Figure 7.5: Grinding chamber of Piconizer

7.3.1.2   2 inch Micronizer®

The 2 inch Micronizer® is composed of three grinding nozzles, each with a 2 mm diameter, and angled at 70° with respect to the normal to the wall. The injector nozzle has a diameter of 2 mm. The chamber height is 8 mm. The central outlet has a diameter of 15 mm. A filter bag was attached to the outlet to collect the milled material while allowing air to pass through. Figure 7.6 shows the grinding chamber of the mill.

Figure 7.6: Grinding chamber of 2 inch Micronizer®

7.3.1.3   4 inch Micronizer®

The 4 inch Micronizer® consists of six grinding nozzles with 1.3 mm diameter, angled at 70° with respect to the normal to the wall. The injector nozzle has a diameter of 2 mm. The chamber height is 4 mm. The central outlet has a diameter of 20 mm. A filter bag was attached to the outlet to collect the milled material. The grinding chamber can be seen in Figure 7.7. A maximum pressure of 6 bar was reachable on site at Astrazeneca for use with the 2 and 4 inch Micronizers.

Figure 7.7: Grinding chamber of 4 inch Micronizer®

7.3.2 Fluid Power of Jet Mills

In order to investigate the scalability of the mills, the fluid power produced by each mill is calculated. This is based on the work of expansion of the gas from the grinding and injector nozzles into the grinding chamber. Working on the assumption of adiabatic flow through a frictionless nozzle, the mass flow rate of air through a nozzle can be calculated depending on the condition of the flowing gas. The critical pressure of the gas, p^*, in the nozzle is first determined:

$$\frac{P^*}{P_0} = \left(\frac{2}{\gamma+1}\right)^{\gamma/(\gamma-1)} \tag{7.10}$$

where P^* is the critical pressure, P_0 is the pressure of gas entering the nozzle, and γ is the ratio of specific heat at constant pressure to specific heat at constant volume (C_p/C_v), which is 1.4 for air and nitrogen. By rearranging Eq. 7.10 the critical pressure can be found:

$$P^* = 0.5285 P_0 \tag{7.11}$$

If the critical pressure is greater than the surrounding pressure in the grinding chamber, then the flow is choked and the Mach number is 1. The pressure in the grinding chamber is assumed to be atmospheric. The pressure at the nozzle exit will also equal the critical pressure due to flow being choked. The mass flux of gas, G (kg/m^2·s) through the nozzle exit can be calculated (Tilton, 2007):

$$G = P_0 \sqrt{\frac{\gamma M_w}{RT_0}} \frac{M_1}{\left(1+\frac{\gamma-1}{2}M_1^2\right)^{(\gamma+1)/2(\gamma-1)}} \tag{7.12}$$

where M_w is the molecular weight of the gas, T_0 is the temperature of gas entering the nozzle, and M_1 is the Mach number at the nozzle exit. When $M_1 = 1$, Eq. 7.12 can be rearranged to:

$$G^* = P_0 \sqrt{\left(\frac{2}{\gamma+1}\right)^{\frac{\gamma+1}{\gamma-1}}\left(\frac{\gamma M_w}{RT_0}\right)} \tag{7.13}$$

Multiplying G^* by the cross-sectional area of the nozzle exit will therefore give the mass flow rate of gas. The exit velocity of gas from the nozzle is:

$$V = M_1 c \tag{7.14}$$

$$c = \sqrt{\frac{\gamma RT}{M_w}} \tag{7.15}$$

Under choked conditions, the equation becomes:

$$V = c^* = \sqrt{\frac{\gamma RT^*}{M_w}} \tag{7.16}$$

where T^* is the critical temperature, defined as:

$$\frac{T^*}{T_0} = \frac{2}{\gamma + 1} \qquad\qquad (7.17)$$

The calculated mass flow rates through the grinding and injector nozzles at the pressures used in the spiral jet mill are presented in Table 7.1. Combining this with the molar work of gas expansion allows for the calculation of the fluid power input to the spiral jet mill.

Table 7.1: Mass flow rates of gas through the grinding and injector nozzles of the Hosokawa Aeroplex Spiral Jet Mill 50AS

Grinding nozzle (0.8 mm diameter)			Injector nozzle (0.9 mm diameter)		
Pressure [bar]	Velocity [m/s]	Mass flow rate (× 10⁻⁴) [kg/s]	Pressure [bar]	Velocity [m/s]	Mass flow rate (× 10⁻⁴) [kg/s]
0.5	302.8	1.8	0.5	302.8	2.3
1	313.2	2.4	1	313.2	3.0
2	313.2	3.6	2	313.2	4.5
3	313.2	4.8	3	313.2	6.0
4	313.2	6.0	4	313.2	7.5

Table 7.2: Mass flow rates of gas through the grinding and injector nozzles of the Piconizer

Grinding nozzle (0.5 mm diameter)			Injector nozzle (1.5 mm diameter)		
Pressure [bar]	Velocity [m/s]	Mass flow rate (× 10⁻⁴) [kg/s]	Pressure [bar]	Velocity [m/s]	Mass flow rate (× 10⁻⁴) [kg/s]
0.5	302.8	0.7	0.5	302.8	6.3
1	313.2	0.9	1	313.2	8.4
2	313.2	1.4	2	313.2	12.6
3	313.2	1.9	3	313.2	16.8
4	313.2	2.3	4	313.2	20.9

Table 7.3: Mass flow rates of gas through the grinding and injector nozzles of the 2 inch Micronizer

Grinding nozzle (2.0 mm diameter)			Injector nozzle (2.0 mm diameter)		
Pressure [bar]	Velocity [m/s]	Mass flow rate (× 10⁻⁴) [kg/s]	Pressure [bar]	Velocity [m/s]	Mass flow rate (× 10⁻⁴) [kg/s]
0.5	302.8	11.2	0.5	302.8	11.2
1	313.2	14.9	1	313.2	14.9
2	313.2	22.4	2	313.2	22.4
3	313.2	29.8	3	313.2	29.8
4	313.2	37.2	4	313.2	37.2

Table 7.4: Mass flow rates of gas through the grinding and injector nozzles of the 4 inch Micronizer

Grinding nozzle (1.3 mm diameter)			Injector nozzle (2.0 mm diameter)		
Pressure [bar]	Velocity [m/s]	Mass flow rate ($\times 10^{-4}$) [kg/s]	Pressure [bar]	Velocity [m/s]	Mass flow rate ($\times 10^{-4}$) [kg/s]
0.5	302.8	4.7	0.5	302.8	11.2
1	313.2	6.3	1	313.2	14.9
2	313.2	9.4	2	313.2	22.4
3	313.2	12.6	3	313.2	29.8
4	313.2	15.7	4	313.2	37.2

The molar work of gas expansion, W (J/mol), associated with a change in pressure is:

$$W = \int_{P_1}^{P_2} V_F \, dP \tag{7.18}$$

where V_F is the gas volume. By treating the gas compressible the gas law is given by $PV_F = ZRT$, and Eq. 7.18 becomes:

$$W = \int_{P_1}^{P_2} Z \frac{RT}{P} \, dP \tag{7.19}$$

where Z is the compressibility factor. By multiplying the molar work by the total molar flow through the nozzles, the total fluid power input can be calculated. The fluid power input for the various combinations of grinding and injector pressure tested in the spiral jet mill are presented in Table 7.5.

Table 7.5: Fluid power input to the Hosokawa Alpine Aeroplex Spiral Jet Mill 50AS at different grinding and injector pressures

Grinding pressure [bar]	Injector pressure [bar]	Fluid power input (× 10⁻⁴) [J/s]
1.0	2.0	6.5
1.0	3.0	7.8
1.0	4.0	9.0
2.0	3.0	12.0
2.0	4.0	13.0
3.0	4.0	17.0

Each of the investigated mills had a different number of grinding nozzles or different grinding nozzle diameter, which affects the fluid power supplied into the grinding chamber at a given grinding pressure, as detailed in Table 7.6.

Table 7.6: Mills and their nozzle details

Mill type	Mill diameter (mm)	No. of grinding nozzles	Nozzle diameter (mm)	
			Grinding	Injector
50AS	50	4	0.8	0.9
Piconizer	33	4	0.5	1.5
2 inch Micronizer	50.8	3	2.0	2.0
4 inch Micronizer	101.6	6	1.3	2.0

The fluid power input from the grinding nozzles for each mill in relation to the supplied grinding pressure is presented in Figure 7.8. In order to compare the performance of these mills, each mill was operated with a grinding pressure that corresponds to the same fluid power input. As mentioned in Chapter 5, the injector nozzle gas pressure has a negligible effect on size reduction, and so only the fluid power input from the grinding nozzles is considered for determining comparable operating conditions.
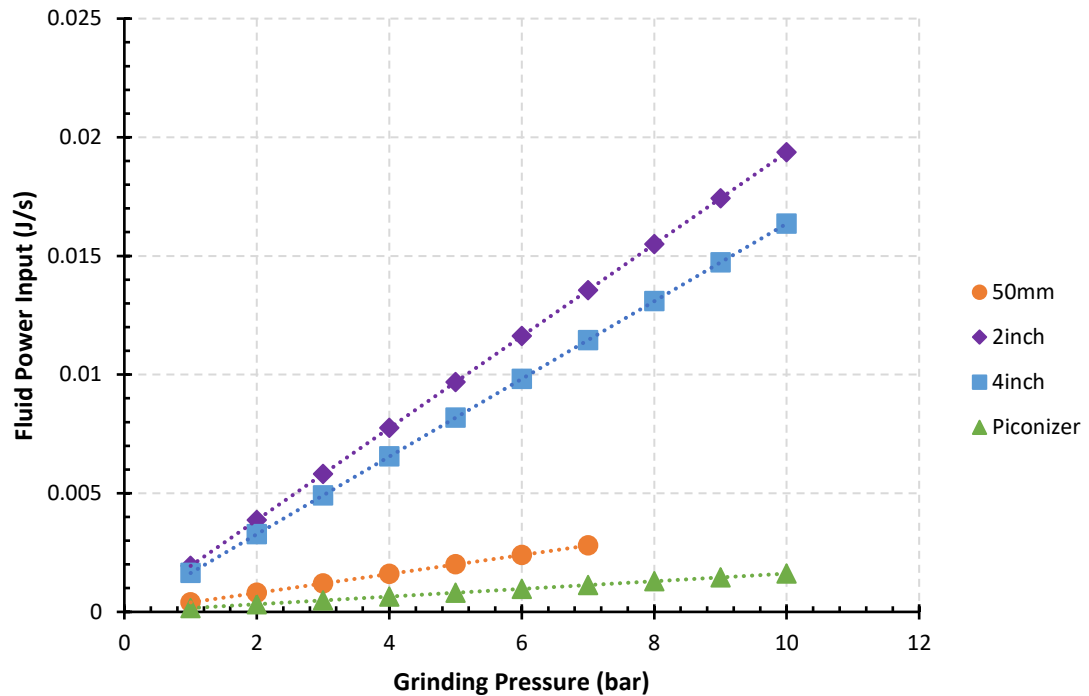
Figure 7.8: Fluid power inputs of each mill as a function of grinding pressure

Looking at the lines for each mill in Figure 7.8, it is clear to see that the 2 inch and 4 inch Micronizers have comparable fluid powers. The 50AS and Piconizer, being comparable to each other in terms of geometry, require much higher grinding pressures (unachievable in practical terms) to reach the same fluid power input as the 2 inch and 4 inch Micronizers.

7.4 Relationship of Fluid Power Input with Change in Specific Surface Area for the Four Mills

α-lactose monohydrate was milled in the various mills at different grinding pressures which corresponded to similar fluid powers. It was fed into the mill at low feed rates ranging from 1 – 3 g/min. The changes in the specific surface area of the material milled in the 2 inch and 4 inch Micronizers, the 50AS mill and the Piconizer, are shown in Figure 7.9. The material milled in the 2 inch and 4 inch Micronizers follow roughly the same trend, where there is an increase in the

ΔSSA/SSA$_f$ as the fluid power input/feed rate increases. This suggests that there is potential for scale-up between the two mills. The 50AS and Piconizer, however, follow a different gradient, with a sharper increase in ΔSSA/SSA$_f$ with fluid power input/feed rate.
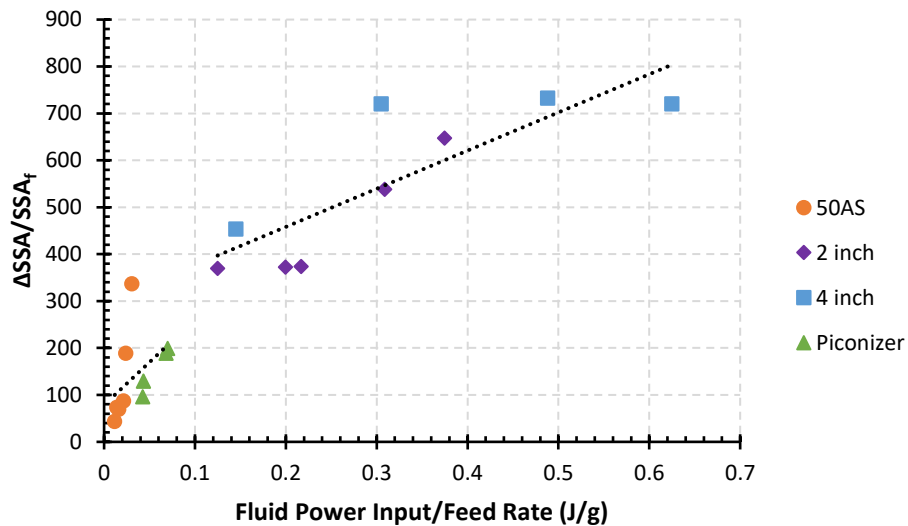
Figure 7.9: The relationship between the change in specific surface area and the fluid power input for different mills

The fluid power used in the 50AS and Piconizer were much lower than that of the 2 and 4 inch Micronizers. The 2 and 4 inch Micronizers produced a greater amount of sub-micron particles compared to the 50AS and Piconizer mills at the maximum achievable grinding pressures, as illustrated by the product size distribution in Figure 7.10.
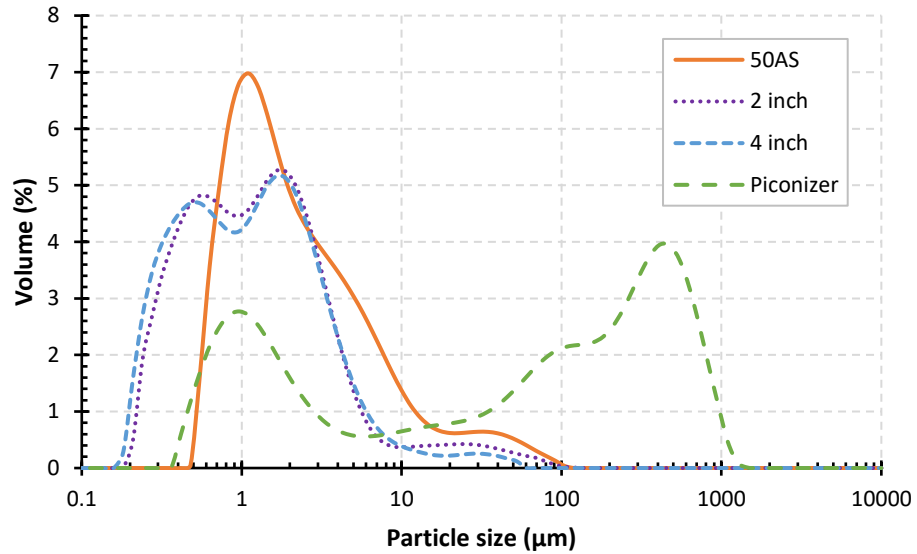
Figure 7.10: Product size distribution of α-lactose monohydrate milled at maximum tested grinding pressure of 3 barg for 50AS, 5 barg for 2 inch, 4.75 barg for 4 inch, and 4 barg for Piconizer

7.5 Conclusions

The potential for scale-up between four different sized spiral jet mills was investigated using α-lactose monohydrate. The mills were found to exhibit similar behaviour in pairs: the Hosokawa Alpine Aeroplex Spiral Jet Mill 50AS and the Hosokawa Alpine Piconizer demonstrated similar trends with regards to the relationship between the fluid power input and ΔSSA of a material, and the 2 inch and 4 inch Micronizer compared well to each other. This is due to the two pairs of mills having similar geometries and nozzle diameters to each other, and therefore were able to reach comparable fluid powers to each other.

While the fluid power input has shown to be a good criterion for scale-up of the spiral jet mill, the solid feed rates for these mills were low. Much higher feed rates are commonly used in industry. It would be beneficial for these mills to be operated at higher feed rates representative of industrial operations to see how

they compare with lower feed rates. A good comparison between the two would

further consolidate the fluid power input as a successful scale-up criterion.

Chapter 8 Conclusions

The spiral jet mill is a widely used size reduction process in the pharmaceutical industry. Using a combination of experimental and simulation work, the jet mill mechanism and the predictability of the milling behaviour of active pharmaceutical ingredients and excipients based on their mechanical properties was investigated to better the understanding of the unit operation.

Three pharmaceutical ingredients were used in this research: aspirin, paracetamol, and α-lactose monohydrate. Using a single particle impact rig, their extent of breakage at different impact velocities was measured and used to infer their mechanical properties in the form of a breakability index. Paracetamol was found to break more extensively than aspirin, which was found to break more extensively than α-lactose monohydrate. The same trend was found as compared to previous work (Bentham et al., 2004; Kwan et al., 2004; Olusanmi et al., 2011).

The Hosokawa Alpine Aeroplex Spiral Jet Mill 50AS was used to mill the three materials under various different gas pressures. The Malvern Mastersizer 2000 was used to measure the size distribution of the milled material and calculate their specific surface area. Paracetamol and aspirin were found to reach their grinding limit at low pressures, while α-lactose monohydrate continued to reduce in size at all tested conditions. This shows that α-lactose monohydrate is harder to break than aspirin and paracetamol, which correlates with the findings of single impact testing. α-lactose monohydrate, however, had a much higher $\Delta SSA/SSA_f$ compared to the other two materials. This may be due to it having a greater hardness than the other two materials, and so the fragments formed during

164

breakage will be smaller than the other materials, leading to a greater SSA at a given grinding condition.

CFD and DEM were used to simulate the 50AS. The model was validated by comparison of the volumetric gas flow rate out of the mill in simulation with that measured from the actual mill. A good correlation was seen between the two. Internal classification was found to only be effective for particle sizes of under 2 μm. Interparticle collisions were found to have a greater amount of dissipated energy compared to particle-wall collisions, indicating that interparticle collisions have the greatest contribution towards particle breakage. An optimum particle size ratio for a high rate of breakage was observed to exist. Decreasing the number of particles, and increasing the grinding nozzle gas pressure, were shown to increase the particle velocities and their relative interparticle collisional velocities. However with large particle numbers their effect was shown to be very small, indicating there would be little effect on the milling performance. Particle stresses were found to be highest just before particles passed the grinding nozzles compared to in front of and after the nozzle. The normal stress was found to have a greater contribution to the stress exerted on the particles than the shear stress. There was also found to be a very low number of particle contacts compared to the number of particles present in the chamber. This suggests that particle breakage is a result of instantaneous particle collisions rather than particle layers shearing over each other.

The scale-up of the spiral jet mill with four different sized mills was investigated. A good correlation was seen between the fluid power input and $\Delta SSA/SSA_f$ of α-lactose monohydrate for the four different mills. It was noted that mills with

similar geometries and nozzle sizes (the 50AS – Piconizer, and 2 inch – 4 inch Micronizers) had comparable fluid input power and their performance compared well with each other.

8.1 Future Work

There are a few ways in which the work presented here can be expanded upon.

Material properties: The relationship between the milling behaviour and the mechanical properties of the material was found not to be straightforward. Different factors which affect the breakage of a material such as the presence of cleavage and slip planes could be investigated and their effect on the spiral jet milling behaviour analysed.

Loading: The spiral jet milling was also carried out at low feed rates. The next step would be to carry out milling at higher feed rates commonly used in industry to investigate whether the milling behaviour is comparable between the two conditions. This would be of great benefit particularly to the pharmaceutical industry, as they would be able to establish the milling performance of a material with a small quantity and predict the result of their large scale operations.

Scale-up: Due to the geometries of the mills used in the scale-up studies and the restrictions on reachable pressures at the testing sites, it was not possible to compare all the mills at the same fluid power conditions. It would be interesting to see whether the milling behaviour is comparable between all four mills. Scale-up studies can also be furthered by investigating the scale-up potential based on the interparticle collisional energies, which would require the use of simulations.

The use of a different pharmaceutical material is also recommended to see what effect mechanical properties play in scale-up.

Decoupling milling and classification: Further work can be done on the CFD-DEM simulations to try to decouple milling from classification. While this would require a very large number and small size of particles which would make for a slow simulation, advances in computing power are making this more achievable. The stress in the spiral jet mill was investigated using a constant number and size of particles. An interesting line of research would be to see how the stress in the system changes when particle sizes and number change, i.e. when particles are breaking and escaping from the mill.

References

Alfano, G., Saba, P. and Surracco, M. 1996. Development of a new jet mill for very fine mineral grinding. *International Journal of Mineral Processing.* **44-45**, pp.327-336.

Ali, M., Bonakdar, T., Ghadiri, M. and Tinke, A. 2015. Particle Breakage in a Scirocco Disperser. *Powder Technology.* **285**, pp.138-145.

Allen, T. 1997. *Particle Size Measurement.* 5th ed. London, UK: Chapman & Hall.

ANSYS Inc. 2011. *ANSYS Fluent User's Guide.*

ANSYS Inc. 2013. *ANSYS Fluent Theory Guide.*

Bagi, K. 1996. Stress and strain in granular assemblies. *Mechanics of Materials.* **22**, pp.165-177.

Bentham, A.C., Kwan, C.C., Boerefijn, R. and Ghadiri, M. 2004. Fluidised-bed jet milling of pharmaceutical powders. *Powder Technology.* **141**, pp.233-238.

Bernotat, S. and Schönert, K. 2006. Size Reduction. *Ullmann's Encyclopedia of Industrial Chemistry.* Weinheim: Wiley-VCH, pp.159-198.

Boudriche, L., Chamayou, A., Calvet, R., Hamdi, B. and Balard, H. 2014. Influence of different dry milling processes on the properties of an attapulgite clay, contribution of inverse gas chromatography. *Powder Technology.* **254**, pp.352-363.

Brosh, T., Batat, Y., Kalman, H., Levy, A. and Brown, A.B. 2008. Particle motion and classification in a jet mill. *Bulk Solids & Powder – Science & Technology.* **3**, pp.1-10.

Brosh, T., Kalman, H. and Levy, A. 2011. Fragments spawning and interaction models for DEM breakage simulation. *Granular Matter.* **13**, pp.765-776.

Brosh, T., Kalman, H., Levy, A., Peyron, I. and Ricard, F. 2014. DEM-CFD simulation of particle comminution in jet-mill. *Powder Technology.* **257**, pp.104-112.

Chaumeil, F. and Crapper, M. 2014. Using the DEM-CFD method to predict Brownian particle deposition in a constricted tube. *Particuology.* **15**, pp.94-106.

Cundall, P.A. 1974. A computer model for rock-mass behaviour using interactive graphics for the input and output of geometrical data. In: *Missouri River Division.*

Cundall, P.A. and Strack, O.D.L. 1979. A discrete numerical model for granular assemblies. *Géotechnique.* **29**, pp.47-65.

de Vegt, O., Vromans, H., den Toonder, J. and van der Voort Maarschalk, K. 2009. Influence of flaws and crystal properties on particle fracture in a jet mill. *Powder Technology.* **191**, pp.72-77.

de Vegt, O., Vromans, H., Faassen, F. and van der Voort Maarschalk, K. 2005a. Milling of Organic Solids in a Jet Mill. Part 1: Determination of the Selection

Function and Related Mechanical Material Properties. *Particle & Particle Systems Characterization.* **22**, pp.133-140.

de Vegt, O., Vromans, H., Faassen, F. and van der Voort Maarschalk, K. 2005b. Milling of Organic Solids in a Jet Mill. Part 2: Checking the Validity of the Predicted Rate of Breakage Function. *Particle & Particle Systems Characterization.* **22**, pp.261-267.

DEM Solutions Ltd. 2012. *Parallel EDEM CFD Coupling for ANSYS FLUENT – Version 1.0 User Guide.*

DEM Solutions Ltd. 2015. *EDEM 2.7 User Guide.*

Djokić, M., Djuriš, J., Solomun, L., Kachrimanis, K., Djurić, Z. and Ibrić, S. 2014a. The influence of spiral jet-milling on the physicochemical properties of carbamazepine form III crystals: Quality by design approach. *Chemical Engineering Research and Design.* **92**, pp.500-508.

Djokić, M., Kachrimanis, K., Solomun, L., Djuriš, J., Vasiljević, D. and Ibrić, S. 2014b. A study of jet-milling and spray-drying process for the physicochemical and aerodynamic dispersion properties of amiloride HCl. *Powder Technology.* **262**, pp.170-176.

Elghobashi, S. 1991. Particle-laden turbulent flows: direct simulation and closure models. *Applied Scientific Research.* **48**, pp.301-314.

Eskin, D. and Kalman, H. 2002. Engineering model of friction of gas-solids flow in a jet mill nozzle. *Chemical Engineering and Technology.* **25**, pp.57-64.

Eskin, D. and Voropayev, S. 2001. Engineering estimations of opposed jet milling efficiency. *Minerals Engineering.* **14**, pp.1161-1175.

Eskin, D., Voropayev, S. and Vasilkov, O. 1999. Simulation of jet milling. *Powder Technology.* **105**, pp.257-265.

Finnie, S., Prasad, K.V.R., Sheen, D.B. and Sherwood, J.N. 2001. Microhardness and dislocation identification studies on paracetamol single crystals. *Pharmaceutical Research.* **18**, pp.674-681.

Ghadiri, M. and Zhang, Z. 2002. Impact attrition of particulate solids. Part 1: A theoretical model of chipping. *Chemical Engineering Science.* **57**, pp.3659-3669.

Gibson, M.M. and Launder, B.E. 1978. Ground effects on pressure fluctuations in the atmospheric boundary layer. *J. Fluid Mech.* **86**, pp.491-511.

Gommeren, H.J.C., Heitzmann, D.A., Moolenaar, J.A.C. and Scarlett, B. 2000. Modelling and control of a jet mill plant. *Powder Technology.* **108**, pp.147-154.

Han, T., Kalman, H. and Levy, A. 2002. DEM Simulation of Particle Comminution in Jet Milling. *Particulate Science and Technology.* **20**, pp.325-340.

Hancock, B., York, P. and Rowe, R.C. 1997. The use of solubility parameters in pharmaceutical dosage form design. *International Journal of Pharmaceutics.* **148**, pp.1-21.

Hare, C. 2010. *Particle Breakage in Agitated Dryers*. thesis, University of Leeds.

Heckel, R.W. 1961. Density-Pressure Relationships in Powder Compaction. *Transactions of the Metallurgical Society of AIME.* **221**, pp.671-675.

References

Hertz, H. 1882. Ueber die Berührung fester elastischer Körper. *Journal für die reine und angewandte Mathematik (Crelle's Journal).* **1882**, pp.156-171.

Hosokawa Alpine AG. 2004. *Operating Manual: Aeroplex Spiral Jet Mill 50AS.*

Hoyer, H., Schlocker, W., Krum, K. and Bernkop-Schnürch, A. 2008. Preparation and evaluation of microparticles from thiolated polymers via air jet milling. *European Journal of Pharmaceutics and Biopharmaceutics.* **69**, pp.476-485.

Hutchings, I.M. 1992. *Tribology: friction and wear of engineering materials.* CRC Press.

Hutchings, I.M. 1993. Mechanisms of wear in powder technology: A review. *Powder Technology.* **76**, pp.3-13.

Johnson, K.L., Kendall, K. and Roberts, A.D. 1971. Surface Energy and the Contact of Elastic Solids. *Proceedings of the Royal Society A: Mathematical, Physical and Engineering Sciences.* **324**, pp.301-313.

Katz, A. and Kalman, H. 2007. Preliminary experimental analysis of a spiral jet mill performance. *Particle and Particle Systems Characterization.* **24**, pp.332-338.

Kolmogorov, A.N. 1941. Equations of turbulent motion in an incompressible fluid. *Doklady Akademii Nauk SSSR.* **30**, pp.299-303.

Kozawa, K., Seto, T. and Otani, Y. 2012. Development of a spiral-flow jet mill with improved classification performance. *Advanced Powder Technology.* **23**, pp.601-606.

Kwan, C.C., Chen, Y.Q., Ding, Y.L., Papadopoulos, D.G., Bentham, a.C. and Ghadiri, M. 2004. Development of a novel approach towards predicting the

milling behaviour of pharmaceutical powders. *European journal of pharmaceutical sciences: official journal of the European Federation for Pharmaceutical Sciences.* **23**, pp.327-336.

Launder, B.E. and Spalding, D.B. 1972. *Lectures in mathematical models of turbulence.* London: Academic Press.

Lawn, B.R. 1993. *Fracture of brittle solids.* 2 ed. Cambridge: Cambridge University Press.

Lawn, B.R. and Evans, A.G. 1977. A model for crack initiation in elastic/plastic indentation fields. *Journal of Materials Science.* **12**, pp.2195-2199.

Lawn, B.R., Evans, A.G. and Marshall, D.B. 1980. Elastic/Plastic Indentation Damage in Ceramics: the Median/Radial Crack System. *Journal of the American Ceramic Society.* **63**, pp.574-581.

Levy, A. and Kalman, H. 2007. Numerical Study of Particle Motion in Jet Milling. *Particulate Science and Technology.* **25**, pp.197-204.

Luding, S. 2008. Cohesive, frictional powders: Contact models for tension. *Granular Matter.* **10**, pp.235-246.

MacDonald, R., Rowe, D., Martin, E. and Gorringe, L. 2016. The spiral jet mill cut size equation. *Powder Technology.* **299**, pp.26-40.

Marsh, D.M. 1964. Plastic Flow in Glass. *Proceedings of the Royal Society A: Mathematical, Physical and Engineering Sciences.* **279**, pp.420-435.

Matinde, E. and Hino, M. 2011. Dephosphorization Treatment of High Phosphorus Iron Ore by Pre-reduction, Mechanical Crushing and Screening Methods. *ISIJ International.* **51**, pp.220-227.

Mebtoul, M., Large, J.F. and Guigon, P. 1996. High velocity impact of particles on a target - An experimental study. *International Journal of Mineral Processing.* **44-45**, pp.77-91.

Meier, M., John, E., Wieckhusen, D., Wirth, W. and Peukert, W. 2008. Characterization of the grinding behaviour in a single particle impact device: Studies on pharmaceutical powders. *European Journal of Pharmaceutical Sciences.* **34**, pp.45-55.

Menter, F.R. 1994. Two-equation eddy-viscosity turbulence models for engineering applications. *AIAA Journal.* **32**, pp.1598-1605.

Midoux, N., Hošek, P., Pailleres, L. and Authelin, J.R. 1999. Micronization of pharmaceutical substances in a spiral jet mill. *Powder Technology.* **104**, pp.113-120.

Mindlin, R. and Deresiewicz, H. 1953. Elastic Spheres in Contact Under Varying Oblique Forces. *Journal of Applied Mechanics.* **20**, pp.327-344.

Mindlin, R.D. 1949. Compliance of Elastic Bodies in Contact. *Journal of Applied Mechanics.* **20**, pp.259-268.

Muehlenfeld, C., Kann, B., Windbergs, M. and Thommes, M. 2013. Solid dispersions prepared by continuous cogrinding in an air jet mill. *Journal of Pharmaceutical Sciences.* **102**, pp.4132-4139.

Müller, F., Polke, R. and Schädel, G. 1996. Spiral jet mills: hold up and scale up. *International Journal of Mineral Processing.* **44-45**, pp.315-326.

Nair, P.B.R. and Ramanujam, M. 1992. Fluid energy grinding. *Advanced Powder Technology.* **3**, pp.273-284.

Ning, Z. 1995. *Elasto-Plastic Impact of Fine Particle and Fragmentation of Small Agglomerates*. thesis, University of Surrey.

Ning, Z. and Ghadiri, M. 2006. Distinct element analysis of attrition of granular solids under shear deformation. *Chemical Engineering Science.* **61**, pp.5991-6001.

Olusanmi, D. 2009. *Milling of Organic Solids*. thesis, University of Leeds.

Olusanmi, D., Roberts, K.J., Ghadiri, M. and Ding, Y. 2011. The breakage behaviour of Aspirin under quasi-static indentation and single particle impact loading: Effect of crystallographic anisotropy. *International Journal of Pharmaceutics.* **411**, pp.49-63.

Olusanmi, D., Wang, C., Ghadiri, M., Ding, Y. and Roberts, K.J. 2010. Effect of temperature and humidity on the breakage behaviour of Aspirin and sucrose particles. *Powder Technology.* **201**, pp.248-252.

Ortega-Rivas, E. 2012. *Unit operations of particulate solids : theory and practice.* CRC Press.

Palaniandy, S. and Azizli, K.A.M. 2009. Mechanochemical effects on talc during fine grinding process in a jet mill. *International Journal of Mineral Processing.* **92**, pp.22-33.

Papadopoulos, D.G. 1998. *Impact breakage of particulate solids*. thesis, University of Surrey.

Papadopoulos, D.G. and Ghadiri, M. 1996. Impact breakage of poly-methylmethacrylate (PMMA) extrudates: I. Chipping mechanism. *Advanced Powder Technology.* **7**, pp.183-197.

Pasha, M., Dogbe, S., Hare, C., Hassanpour, A. and Ghadiri, M. 2014. A linear model of elasto-plastic and adhesive contact deformation. *Granular Matter.* **16**, pp.151-162.

Prasad, K.V.R., Sheen, D.B. and Sherwood, J.N. 2001. Fracture property studies of paracetamol single crystals using microindentation techniques. *Pharmaceutical Research.* **18**, pp.867-872.

Ramanujam, M. and Venkateswarlu, D. 1969. Studies in fluid energy grinding. *Powder Technology.* **3**, pp.92-101.

Rodnianski, V., Krakauer, N., Darwesh, K., Levy, A., Kalman, H., Peyron, I. and Ricard, F. 2013. Aerodynamic classification in a spiral jet mill. *Powder Technology.* **243**, pp.110-119.

Rumpf, H. 1973. Physical aspects of comminution and new formulation of a law of comminution. *Powder Technology.* **7**, pp.145-159.

Saleem, I.Y. and Smyth, H.D.C. 2010. Micronization of a soft material: air-jet and micro-ball milling. *AAPS PharmSciTech.* **11**, pp.1642-1649.

Salman, A.D. and Gorham, D.A. 1997. Observation of blunt indentation at high loads. *Journal of Materials Science Letters.* **16**, pp.1099-1100.

Salman, A.D. and Gorham, D.A. 2000. The fracture of glass spheres. *Powder Technology.* **107**, pp.179-185.

Schuhmann Jr, R. 1940. Principles of comminution, I. Size distribution and surface calculation. *American Institute of Mining, Metallurgical, and Petroleum Engineers.*

Seipenbusch, M., Toneva, P., Peukert, W. and Weber, A.P. 2007. Impact fragmentation of metal nanoparticle agglomerates. *Particle and Particle Systems Characterization.* **24**, pp.193-200.

Sikong, L., Kooptanond, K., Morasut, N. and Pongprasert, T. 2008. Fine grinding of brittle minerals and materials by jet mill. *Songklanakarin Journal of Science and Technology.* **30**, pp.377-384.

Subero-Couroyer, C., Ghadiri, M., Brunard, N. and Kolenda, F. 2005. Analysis of catalyst particle strength by impact testing: The effect of manufacturing process parameters on the particle strength. *Powder Technology.* **160**, pp.67-80.

Sun, H., Hohl, B., Cao, Y., Handwerker, C., Rushing, T.S., Cummins, T.K. and Weiss, J. 2013. Jet mill grinding of portland cement, limestone, and fly ash: Impact on particle size, hydration rate, and strength. *Cement and Concrete Composites.* **44**, pp.41-49.

Teng, S., Wang, P., Zhang, Q. and Gogos, C. 2011. Analysis of Fluid Energy Mill by gas-solid two-phase flow simulation. *Powder Technology.* **208**, pp.684-693.

Teng, S., Wang, P., Zhu, L., Young, M.W. and Gogos, C.G. 2009. Experimental and numerical analysis of a lab-scale fluid energy mill. *Powder Technology.* **195**, pp.31-39.

Thornton, C. and Ning, Z. 1998. A theoretical model for the stick/bounce behaviour of adhesive, elastic-plastic spheres. *Powder Technology.* **99**, pp.154-162.

Tilton, J.N. 2007. Fluid and Particle Dynamics. *Perrys' Chemical Engineers' Handbook.* pp.1-54.

Tomas, J. 2007. Adhesion of ultrafine particles-A micromechanical approach. *Chemical Engineering Science.* **62**, pp.1997-2010.

Tuunila, R. and Nyström, L. 1998. Effects of grinding parameters on product fineness in jet mill grinding. *Minerals Engineering.* **11**, pp.1089-1094.

Vatsaraj, N.B., Gao, D. and Kowalski, D.L. 2003. Optimization of the operating conditions of a lab scale Aljet mill using lactose and sucrose: a technical note. *AAPS PharmSciTech.* **4**, pE27.

Vogel, L. and Peukert, W. 2003. Breakage behaviour of different materials - Construction of a mastercurve for the breakage probability. *Powder Technology.* **129**, pp.101-110.

Vogel, L. and Peukert, W. 2004. Determination of material properties relevant to grinding by practicable labscale milling tests. *International Journal of Mineral Processing.* **74**, pp.S329-S338.

Vogel, L. and Peukert, W. 2005. From single particle impact behaviour to modelling of impact mills. *Chemical Engineering Science.* **60**, pp.5164-5176.

Weibull, W. 1951. A statistical distribution function of wide applicability. *Journal of Applied Mechanics.* **18**, pp.293-297.

Yang, W., Kwan, C.C., Ding, Y.L., Ghadiri, M. and Roberts, K.J. 2007. Milling of sucrose. *Powder Technology.* **174**, pp.14-17.

Zhang, Z. and Ghadiri, M. 2002. Impact attrition of particulate solids. Part 2: Experimental work. *Chemical Engineering Science.* **57**, pp.3671-3686.

Zhao, Q.Q. and Schurr, G. 2002. Effect of motive gases on fine grinding in a fluid energy mill. *Powder Technology.* **122**, pp.129-135.

Zhu, H.P., Zhou, Z.Y., Yang, R.Y. and Yu, A.B. 2007. Discrete particle simulation of particulate systems: Theoretical developments. *Chemical Engineering Science.* **62**, pp.3378-3396.

Zügner, S., Marquardt, K. and Zimmermann, I. 2006. Influence of nanomechanical crystal properties on the comminution process of particulate solids in spiral jet mills. *European Journal of Pharmaceutics and Biopharmaceutics.* **62**, pp.194-201.